Technical University of Denmark

DTU

Wind tunnel tests of the Risø-A1-18, Risø-A1-21 and Risø-A1-24 airfoils

Fuglsang, Peter; Dahl, K.S.; Antoniou, I.

Publication date:
1999

Document Version
Publisher's PDF, also known as Version of record

Link back to DTU Orbit

DTU Library
Technical Information Center of Denmark

Wind Tunnel Tests of the Risø-A1-18, Risø-A1-21 and Risø-A1-24 Airfoils

Peter Fuglsang, Kristian S. Dahl, Ioannis Antoniou

FINAL

DRAFT

Abstract

This report contains 2D measurements of the Risø-A1-18, Risø-A1-21 and Risø-A1-24 airfoils. The aerodynamic properties were derived from pressure measurements on the airfoil surface and in the wake. The VELUX open jet wind tunnel was used having a background turbulence intensity of 1%, a flow velocity of 42 m/s and a Reynolds number of 1.6×10^6. The airfoil sections had a chord of 0.60 m and a span of 1.9 m and end plates were used to minimise 3D flow effects. The measurements comprised both static and dynamic inflow where dynamic inflow was obtained by pitching the airfoil in a harmonic motion. We tested the influence of leading edge roughness, vortex generators and Gurney flaps both individually and in combination.

For smooth surface conditions, all three airfoils had the desirable properties of constant lift curve slope and low drag coefficient until the maximum lift of about 1.4 was reached. The Risø-A1-18 airfoil had a smooth post stall whereas the Risø-A1-21 and Risø-A1-24 airfoils had a significant drop in the lift coefficient after stall. Test on all airfoil sections mounted with zigzag tape showed that the airfoils were insensitive to leading edge roughness. However with a drop in the maximum lift coefficient to about 1.2. Mounting of delta wing shaped vortex generators and Gurney flaps showed that there was room for a significant increase in the maximum lift coefficient, which was increased to 1.90 for Risø-A1-24 with vortex generators located at 15% chord. The combination of vortex generators and Gurney flaps increased the maximum lift coefficient to about 2.0.

The work was carried out within the EFP 98 project, 'Experimental verification of the Risø-A airfoil family' with the following partners:

- LM Glasfiber A/S.   Peter Grabau,
                                           Peter Hansen,
                                           Steen Z. Dyremose,
                                           Niels Brønnum

- Vestas Wind Systems A/S   Kaj Morbech,
                                           Mark Slot

- The Techical University of Denmark   Stig Øye

- Risø National Laboratory   Peter Fuglsang
                                           Ioannis Antoniou
                                           Kristian S. Dahl

Contents

Nomenclature

c	[m]	Airfoil chord
h	[m]	Jet height
k		Reduced frequency
Δp	[Pa/m]	Pressure loss
p	[Pa]	Static pressure
p_o	[Pa]	Total pressure head
q	[Pa]	Dynamic pressure
s		Airfoil surface co-ordinate
t	[s]	Pitch motion time
x		Co-ordinate in chord direction
y		Wake rake vertical co-ordinate, airfoil vertical co-ordinate
A	[°]	Pitch motion amplitude
C_D		Drag coefficient
C_L		Lift coefficient
C_M		Moment coefficient
C_N		Normal force coefficient
C_P		Airfoil pressure coefficient
C_T		Tangential force coefficient
Re		Reynolds number
T	[°C]	Air temperature
V	[m/s]	Velocity
α	[rad] [°]	Angle of attack
ε		Speed-up factor
ρ	[kg/m^3]	Air density
ω	[rad/s]	Pitch motion angular velocity

Subscripts

1-3	Pitot tube measurement
a	Airfoil section measurement
atm	Atmospheric value
j	Jet outlet measurement
m	Mean value
min	Minimum value
max	Maximum value
p	Pressure measurement
t	Measured value (uncorrected)
w	Wake rake measurement
∞	Free stream reference for normalisation of airfoil forces

1 Introduction

This report concerns 2D wind tunnel measurements of the Risø-A1-18, Risø-A1-21 and Risø-A1-24 airfoils. These airfoils are members of an airfoil family that was recently developed by Risø National Laboratory for use on wind turbines [1]. The airfoils were specially designed for wind turbines with either stall, active stall or pitch regulation. The operational design Reynolds numbers were around Re = 3.0 million depending on the relative thickness. This corresponds to a rotor size of around 600 kW. The measurements were carried out in the VELUX wind tunnel, which has an open test section with a background turbulence level of 1% and a maximum flow velocity of 42 m/s. All tests were carried out at the highest possible Reynolds number of 1.6 million. The angle of attack range was between -5° and 30°. Pressure distribution measurements were taken on the airfoil section together with wake rake pressure measurements. The testing facility is described in detail in Fuglsang et al., 1998 [2].

The test matrix included:
- Steady and quasi-steady inflow measurements where mean values were obtained for the airfoil aerodynamic coefficients. The angle of attack was changed continuously at an average rate around 0.3°/s. Alternatively the angle of attack was changed in steps of 2° and a 20 s duration time series was obtained for each angle of attack.
- Dynamic inflow measurements with the airfoil in pitching motion at amplitudes around ±2° and reduced frequencies around 0.1. The hysteresis effects on the aerodynamic coefficients were derived.

The airfoils were tested under the following configurations:
- Smooth surface, referred to as, 'smooth flow'.
- Vortex generators on the suction side to delay separation and increase the maximum lift coefficient referred to as, 'VG'.
- Gurney flaps on the pressure side trailing edge to increase the maximum lift coefficient referred to as, 'GF'.
- Leading edge roughness to simulate the change of the aerodynamic coefficients from dirt and dust accumulation referred to as, 'LER'.
- Different combinations of vortex generators, Gurney flaps and leading edge roughness.

2 Experimental set-up

The experimental set-up is briefly described in this chapter. A more complete description can be found in Fuglsang *et al.*, 1998 [2].

2.1 Testing facility

The VELUX wind tunnel is of the closed return type with an open test section with a cross section of 7.5×7.5 m and a length of 10.5 m, Figure 2-1. The cross section of the jet blowing into the test section is 3.4×3.4 m. The maximum flow velocity is 42 m/s.
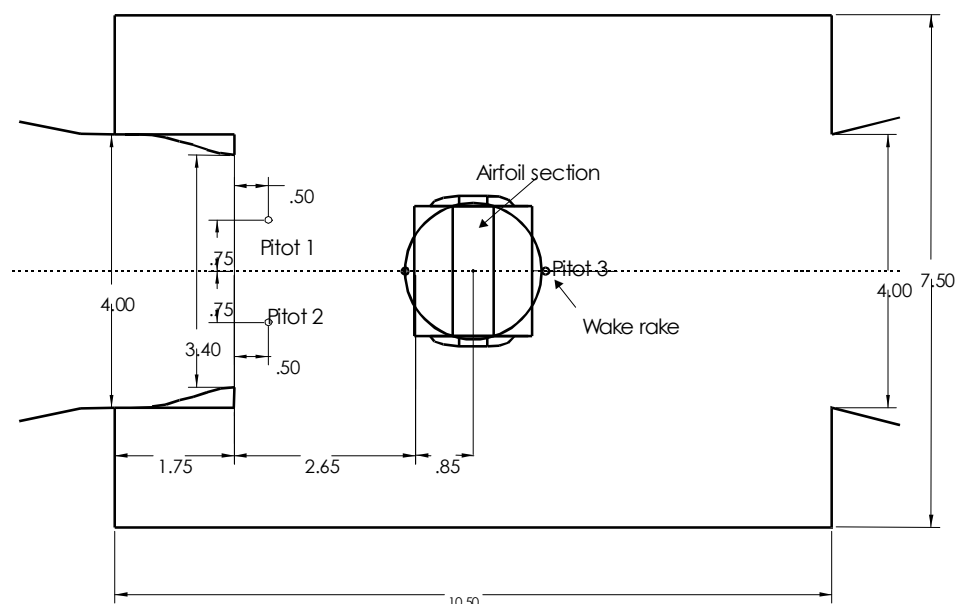

Figure 2-1 The wind tunnel test section with the test stand seen in a top view. with the flow coming from the left.

A test stand was built for 2D airfoil testing, Figure 2-2. The test stand was inserted in the tunnel test section. The airfoil section with a span of 1.9 m and a chord of 0.6 m was mounted 1.7 m from the tunnel floor and 3.2 m from the nozzle outlet. End plates were fixed to the stand at the ends of the airfoil section to limit 3d effects.

Three Pitot tubes measured static and total pressure at different locations in the test section, Figure 2-1. These Pitot tubes were used to measure the wind tunnel reference pressures and to estimate the turbulence level and the stability of the wind tunnel flow.

Quasi-steady measurements at continuously varying angles of attack as well as dynamic inflow measurements were possible. Dynamic inflow was obtained by pitching the airfoil section at different reduced frequencies up to $k = 0.15$ and amplitudes between $\pm 1° < A < \pm 5°$ with the pitch axis located at $x/c = 0.40$, see section 2.4.
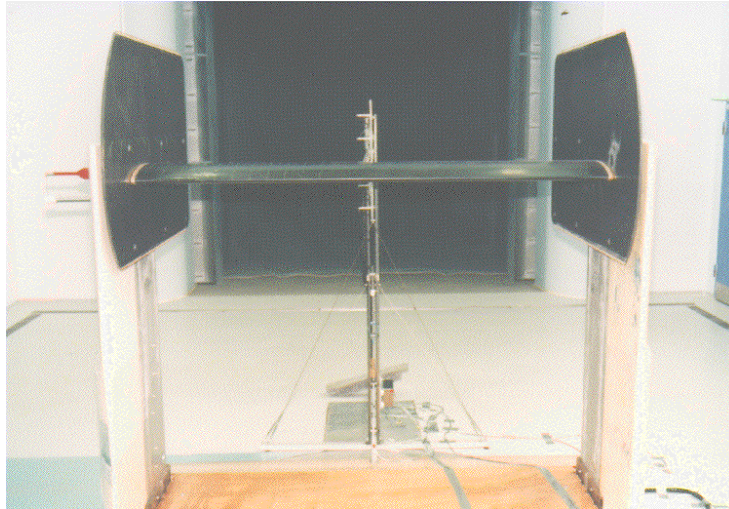
Figure 2-2 The test section with the test stand and the wake rake downstream of the airfoil section.

The wake rake consisted of 53 total pressure probes and five static tubes. The vertical span was 0.456 m, Figure 2-3. The distance between the airfoil trailing edge and the wake rake was 0.7 airfoil chords and the centre of the wake rake was placed at the height of the trailing edge at 0° incidence and behind the centre line of the airfoil section. The rake was not traversed in the horizontal or the vertical directions.
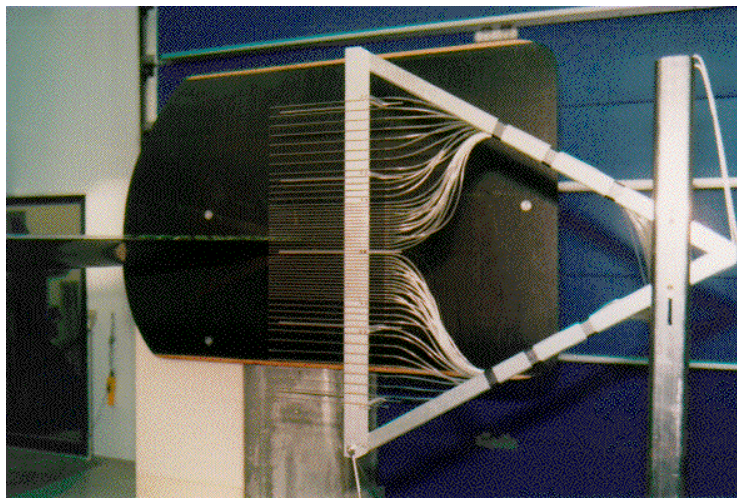

Figure 2-3 The wake rake seen from the side in front of an endplate.

The HyScan 2000 data acquisition system from Scanivalve Corp. was used. Two ZOC33 pressure-scanning modules recorded the pressure signals. For the airfoil surface pressures, 40 psi and 24 2.5psi range sensors were used. For the wake rake and the Pitot tubes, 10′′ H_2O sensors were used. The ZOC module for the airfoil pressures was mounted on the test stand side just outside the airfoil section. Equal length tubes were lead from the airfoil section through a hollow axis to the pressure module. The pressure module used for the wake and the Pitot tube measurements was placed on the floor next to the wake rake. A ZOCEIM16 module was used for the acquisition of the electrical signals.

A total of 134 signals were measured by the data acquisition system during the measurement campaigns:

- 64 airfoil surface static pressures, $p_a(s)$
- 5 wake rake static pressures, $p_w(y)$
- 53 wake rake total pressures, $p_{ow}(y)$
- 3 Pitot tube static pressures, p_{1-3}
- 3 Pitot tube total pressures, p_{o1-3}
- Angle of attack, α
- Air temperature, T
- Atmospheric pressure, p_{atm}
- 2 strain gauges for recording shaft bending corresponding to the lift and drag forces experienced by the airfoil section.
- Electric motor frequency

2.2   Wind tunnel boundary corrections

Wind tunnel corrections should be applied for streamline curvature and down-wash. Horizontal buoyancy, solid and wake blockage could on the other hand be neglected because the test section configuration corresponds to an open jet, which is free to expand, Ray and Pope, 1984 [3]. The application of wind tunnel boundary corrections for the VELUX wind tunnel was verified in Fuglsang *et al.,* 1998 [2].

Streamline curvature is introduced to the flow, especially in the case of open test sections. Solid walls do not bound the flow, which is then free to diverge downstream of the airfoil section. The curvature of the flow induces drag and influences the effective angle of attack over the airfoil. In the case of the VELUX tunnel, the presence of the floor close to the jet bottom boundary will influence the streamline curvature and will introduce uncertainty on the wind tunnel corrections. This influence was assumed to be negligible and the applied corrections for streamline curvature do not account for it.

Down-wash is introduced to the flow when the jet dimensions exceed the airfoil section span. The airfoil section corresponds to a finite wing and trailing vortices appear at the ends of the span although reduced by the end plates. The trailing vorticity induces a down-wash velocity in the case of positive lift coefficient. Due to the down wash the angle of attack is reduced and additional drag is induced.

Both down-wash and streamline curvature result in a change in the angle of attack due to the induction of a velocity normal to the flow direction and the airfoil section. It is assumed in this case that down-wash is insignificant compared with streamline curvature because of the presence of end plates.

For the correction of streamline curvature, the method of Brooks and Marcolini, 1984 [4] was used.

The corrected angle of attack, α, is found from:

$$\alpha = \alpha_t - \frac{\sqrt{3\sigma}}{\pi} C_L - \frac{2\sigma}{\pi} C_L - \frac{\sigma}{\pi}(4C_{Mt}) \; [rad]$$

(2-1)

Where

$$\sigma = \frac{\pi^2}{48} \cdot \left(\frac{c}{h}\right)^2$$

(2-2)

The drag coefficient, C_D, is calculated from:

(2-3)

$$C_D = C_{Dt} + \left[-\frac{\sqrt{3\sigma}}{\pi} C_L\right] C_L$$

The moment coefficient, C_M, is obtained:

$$C_M = C_{Mt} - \frac{\sigma}{2} C_L$$

(2-4)

For details see Fuglsang *et al.*, 1998 [2].

2.3   Wind tunnel flow conditions

In Fuglsang *et al.,* 1998 [2] the wind tunnel flow conditions are investigated and it is found that:

- The turbulence intensity at the test section inlet is 1%.
- Between the inlet and the airfoil section, there is a speed-up of, $\varepsilon_{j\text{-}a} = 6.9\%$, and a static pressure drop of $\Delta p_{j\text{-}a} = 15$ Pa/m.

The wind tunnel references for static, p_∞ and total pressures, $p_{o\infty}$ were derived from Pitot 1 measurements, Figure 2-1. The flow acceleration between Pitot 1 and the airfoil section, $\varepsilon_{1\text{-}\infty} = 5.9\%$ and the static pressure drop between Pitot 1 and the airfoil section, $\Delta p_{1\text{-}\infty} = 15$ Pa/m were determined in Fuglsang *et al.,* 1998 [2] and they are taken into account at the calculation of p_∞ and $p_{o\infty}$.

2.4   Calculation methods

The airfoil pressure coefficient, $C_p(s)$, around the airfoil surface, s, is calculated from:

$$C_p(s) = \frac{p_a(s) - p_\infty}{q_\infty}$$

(2-5)

Where

$$q_\infty = p_{o\infty} - p_\infty$$

(2-6)

The normal force coefficient, C_N, and the tangential force coefficient, C_T, are found from integration of the $C_P(s)$ distribution along the *x*- and *y*-axis as seen

in Figure 2-4. The airfoil lift coefficient, C_L, and drag coefficient, C_D, are found by resolving C_N and C_T perpendicular to and parallel with the oncoming flow:

$$C_L = \cos(\alpha)C_N + \sin(\alpha)C_T$$

(2-7)

$$C_D = -\cos(\alpha)C_T + \sin(\alpha)C_N$$

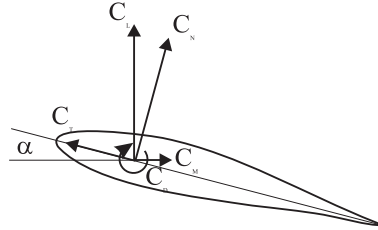The moment coefficient, C_M, is found from integration of $C_P(s)$ at $x/c = 0.25$.

Figure 2-4 Sign convention for aerodynamic coefficients.

The total airfoil drag is the sum of skin friction and pressure drag. By assuming a control surface, which surrounds the airfoil section, the total drag can be calculated from the balance of the momentum flux entering and exiting the control surface. The momentum profile entering is assumed uniform and is calculated from the wind tunnel free stream reference pressures. The momentum profile exiting is calculated from the pressures measured by the wake rake.

Assuming that the flow is 2D, the total wake drag coefficient, C_{Dw}, is calculated from Rae and Pope, 1984 [3]:

$$C_{Dw} = \frac{2}{c}\int_{y_{min}}^{y_{max}} \sqrt{\frac{p_o(y) - p(y)}{q_\infty}} \cdot \left(1 - \sqrt{\frac{p_o(y) - p(y)}{q_\infty}}\right) dy$$

(2-8)

In the analysis of dynamic loads, while the airfoil is in pitching motion, the pitching motion is described by the equation:

$$\alpha = A\sin(\omega t) + \alpha_m$$

(2-9)

The pitching motion is related to the reduced frequency:

$$k = \frac{\omega c}{2V_\infty}$$

(2-10)

3 Airfoil sections and aerodynamic devices

The tested airfoils were the Risø-A1-18, Risø-A1-21 and Risø-A1-24 airfoils from Fuglsang and Dahl, 1999 [1].

3.1 Airfoil sections

For all airfoil sections, the span was 1.9 m and the chord was 0.60 m. Vestas Wind Systems A/S manufactured the Risø-A1-18 model and LM Glasfiber A/S manufactured the Risø-A1-21 and Risø-A1-24 models. Risø carried out the instrumentation of pressure tabs, end pieces and strain gauges. Each model was manufactured in two pieces as an upper and a lower shell to facilitate instrumentation. The models were made of GRP in moulds. The pressure taps were holes drilled directly in the model surface with the exception of the leading and trailing edges where tubes were installed through the model surface, flush with the surface. Inside the model metal tubes were mounted parallel to the drilled holes and flexible plastic tubes were connected to the metal tubes. When the instrumentation was completed the two shells were assembled. The pressure tubes were taken outside of the model through a hollow axis at one side of the airfoil.

The airfoil sections were equipped with 62 pressure taps of 0.5 mm inner diameter in the centre line region. The taps were placed along the chord at the centre line of the model in a staggered alignment to minimise disturbances from upstream taps. Additional taps were drilled close to the centre line as a back up to taps at important positions, e.g., the leading and trailing edges, and in order to allow measurements away from the centre line.

The position of the pressure taps on the model was decided by looking on the theoretical pressure distributions derived by numerical calculations. The distribution of the pressure taps reflected the expected pressure gradients and the tap spacing was dense at leading edge. There was higher concentration on the upper surface compared to the lower surface. After the model was permanently assembled the model dimensions and the tap positions were checked for compliance with the theoretical ones, with the help of a CNS flat-bed machine.

Only minor differences were found between the theoretical and the measured co-ordinates. For all airfoil models, it was concluded that this would not result in significant errors in the pressure distribution and in the derivation of aerodynamic loads.

3.2   Vortex generators

Vortex generators (VGs) are often used at the inner part of wind turbine blades located on the blade suction side between 10% to 30% of the chord counted from the leading edge. They increase the maximum lift coefficient by delaying separation on the airfoil suction side to higher incidences. At the same time, they increase the drag coefficient.

A parametric study was conducted where VGs of height 6 mm were used at different chordwise locations. However not all combinations were tried for all the airfoils. The design of the VGs followed the guide lines from Hoerner and Borst, 1975 [5] and was similar to those used for numerous airfoil tests by Timmer, 1992 [6], at Delft University.

Figure 3-1 shows the shapes and dimensions of the used VGs. They have a height of 6 mm a length of 18 mm. The angles relative to the chordwise direction are ±19.5°. The leading edge spacing between two VGs is 10 mm and the distance between two consecutive pairs is 25 mm. They are of the Delta wing type with a shape of orthogonal triangles and they are placed with their right-angle perpendicular to the airfoil surface and their height increases towards the trailing edge. The presence of the VGs results in the formation of counter-rotating vortices, which transfer high momentum fluid down to the airfoil surface and thus delay separation. To achieve this VGs are arranged in pairs at equal and opposite angles relative to the chord of the blade.

The VGs were constructed from 0.2 mm thick stainless steel. Each VG was cut out and bent perpendicular to the surface. The VGs were glued on the airfoil model surface separately. The thickness of the gluing surface will slightly disturb the measurements since the flow has to enforce the edge of the gluing surface. In particular the drag coefficient at low angles of attack will be increased.
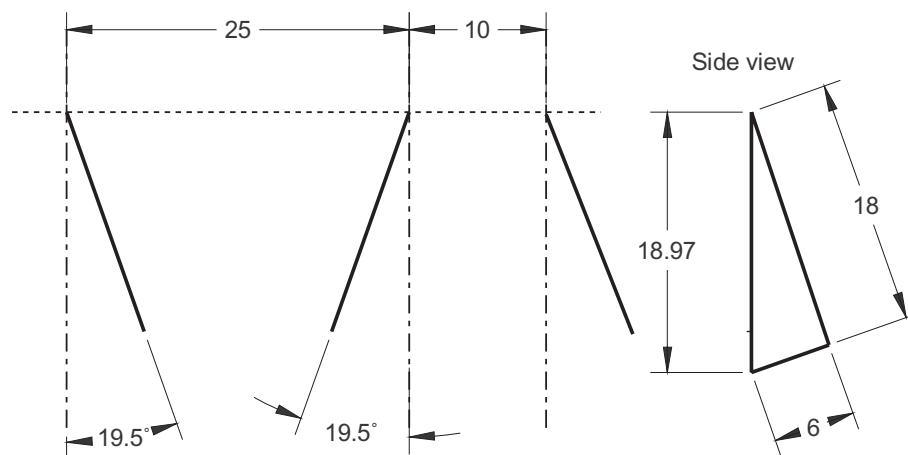

Figure 3-1 Vortex generators of height 6 mm, length 18 mm.

3.3   Gurney flaps

A Gurney flap (GF) is a small flap rigidly attached to the trailing edge of the pressure side of the airfoil. The intended purpose of a GF is to improve the airfoil performance by increasing the lift coefficient without introducing a commensurate increase in drag coefficient.

A parametric study was conducted for the Risø-A1-24 airfoil where GFs of height 1% and 2% of the chord respectively were used.

The GFs were constructed from 0.2 mm thick strip, bent in a 90° angle so that they were mounted perpendicular to the pressure side trailing edge surface.

3.4   Leading edge roughness

Trip tape was mounted to the airfoil model surface to simulate the effects from leading edge roughness (LER). LER appears when dirt, bugs or soil are accumulated on the wind turbine blades in dirty environments.

The used trip tape was originally intended for use on gliders and were manufactured as fibre enforced plastic tape that was glued to the airfoil model surface. The trip tape was mounted at $x/c = 0.05$ on the suction side and at $x/c = 0.10$ on the pressure side.

Figure 3-2 shows the used 90° zigzag trip tape with a 90° angle, a width of 3 mm and a thickness of 0.35 mm.
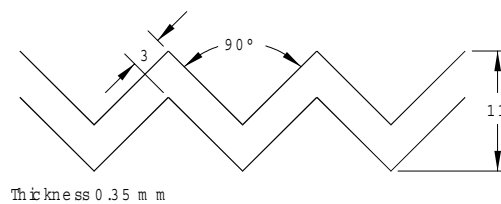
Figure 3-2 Trip tape with 90° zigzag of 3 mm width and 0.35 mm thickness.

4 Results

All shown results were corrected for wind tunnel effects and the aerodynamic forces were referenced to the wind tunnel free stream flow by use of Pitot 1 taking into account corrections for speed-up and pressure loss.

The measurements for each airfoil are reported in Chapter 5 – 7 and the measurements are discussed in Chapter 8.

The different types of conducted measurements are described in Appendix A.

4.1 Testing conditions

The testing conditions are shown in Table 4-1.

Table 4-1 Testing conditions

Airfoil chord	$c = 0.60$ m
Flow velocity	$v = 42$ m/s
Reynolds number	$Re = 1.6 \times 10^6$
Dynamic inflow	
Angular velocity	$\omega = 12.9$ *rad/s*
Reduced frequency	$k = 0.092$
Amplitude	$1.4^o < A < 2.0^o$

4.2 Numerical calculations

The measurements were compared with numerical calculations when it was possible. The Ellipsys2D Navier-Stokes code, Sørensen, 1995 [7], with the k-ω SST turbulence model, Menter, 1993 [8], was used for turbulent flow calculations. Free transition was modelled using the Michel transition criteria, Michel, 1952 [9].

The leading edge roughness measurements were compared with numerical calculations. The Ellipsys2D Navier-Stokes code was used with turbulent flow on the entire airfoil to simulate leading edge roughness.

Measurements with vortex generators and Gurney flap were not compared with numerical calculations.

5 Results for Risø-A1-18

5.1 Risø-A1-18 Smooth flow (run017)
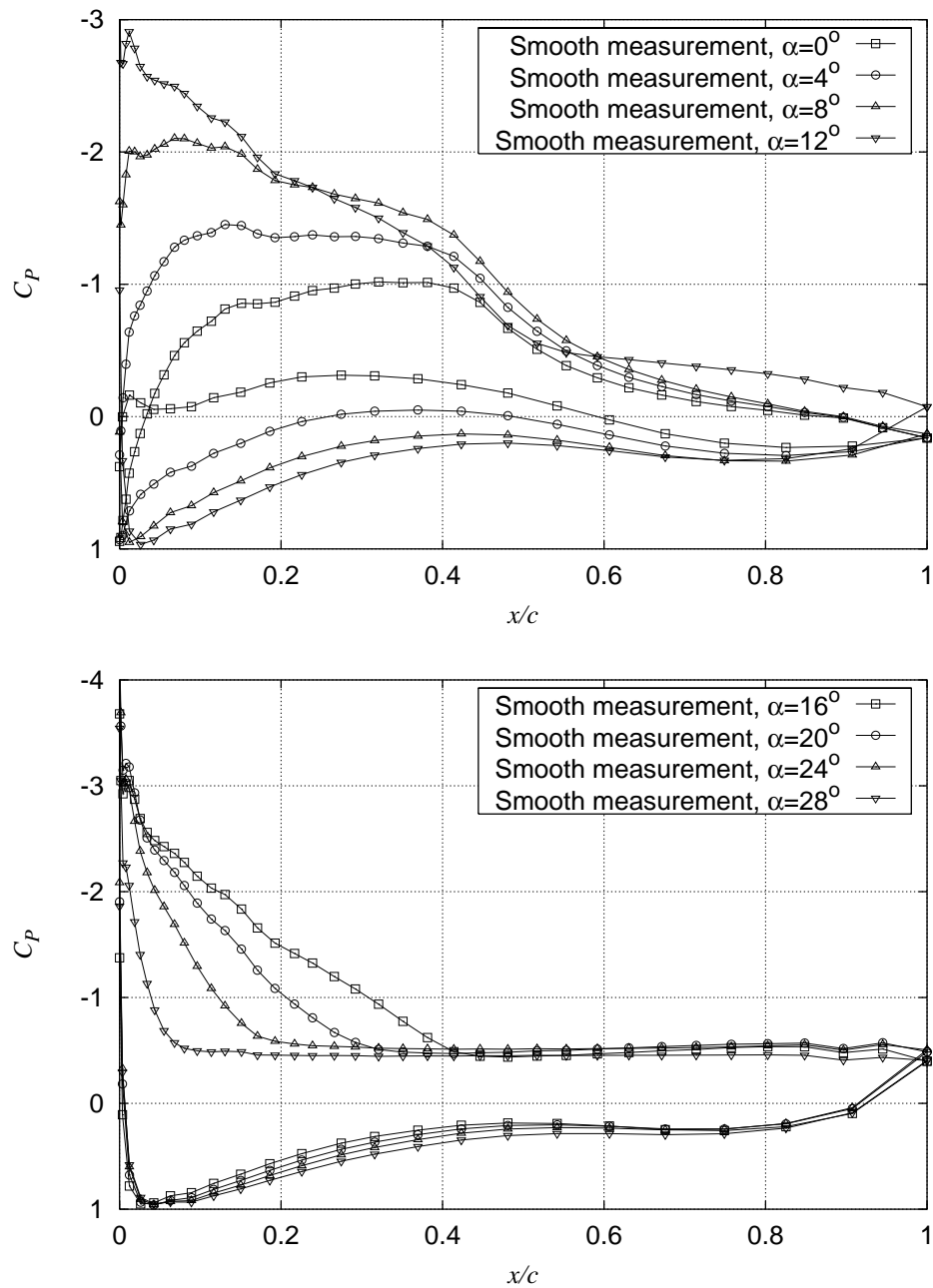
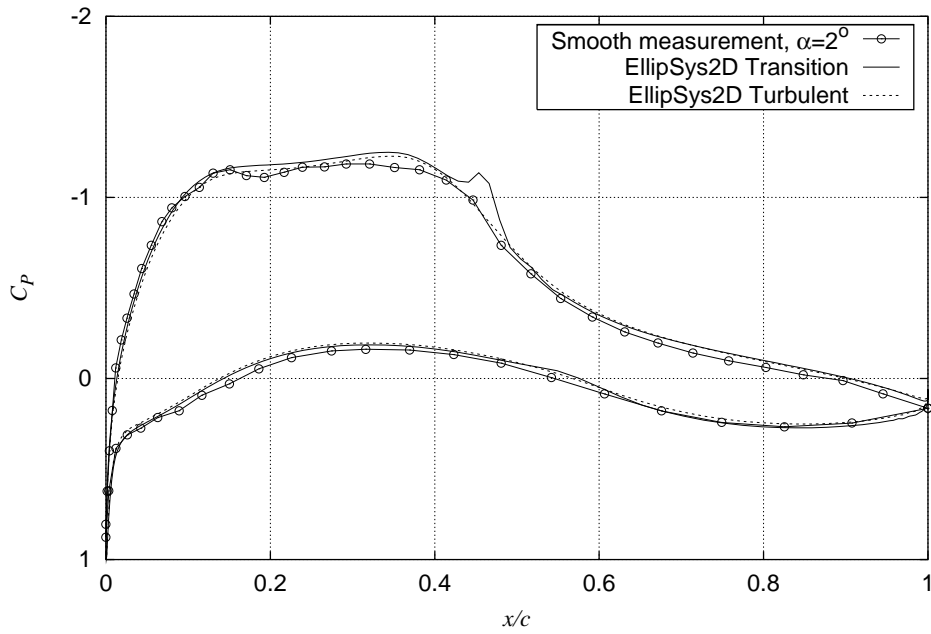Figure 5-1 C_P at different angles of attack for Risø-A1-18 smooth measurement (run017).

Figure 5-2 C_P at $\alpha = 2°$ for Risø-A1-18 smooth measurement compared with EllipSys2D calculations with transition modeling and turbulent flow respectively (run017).
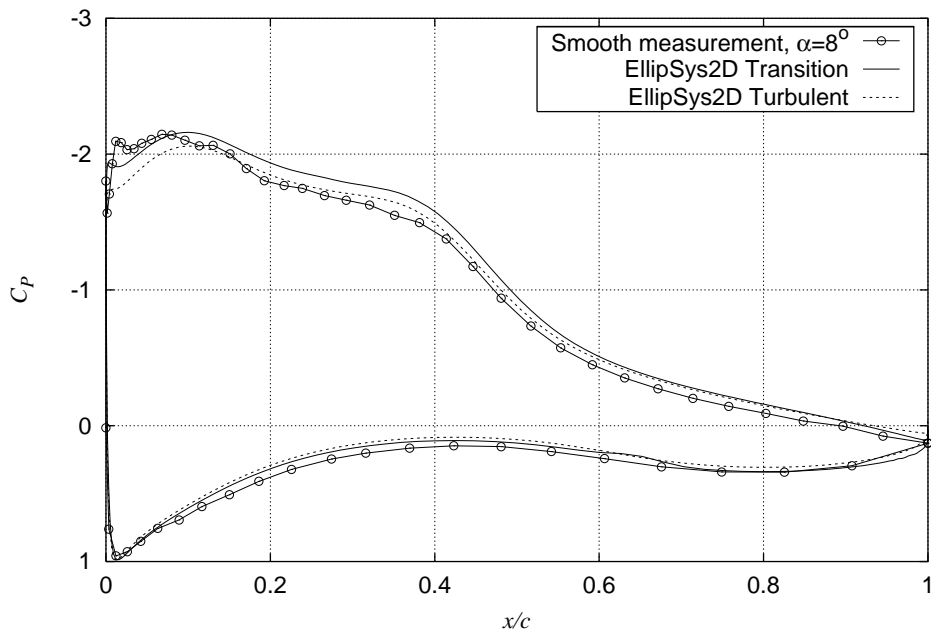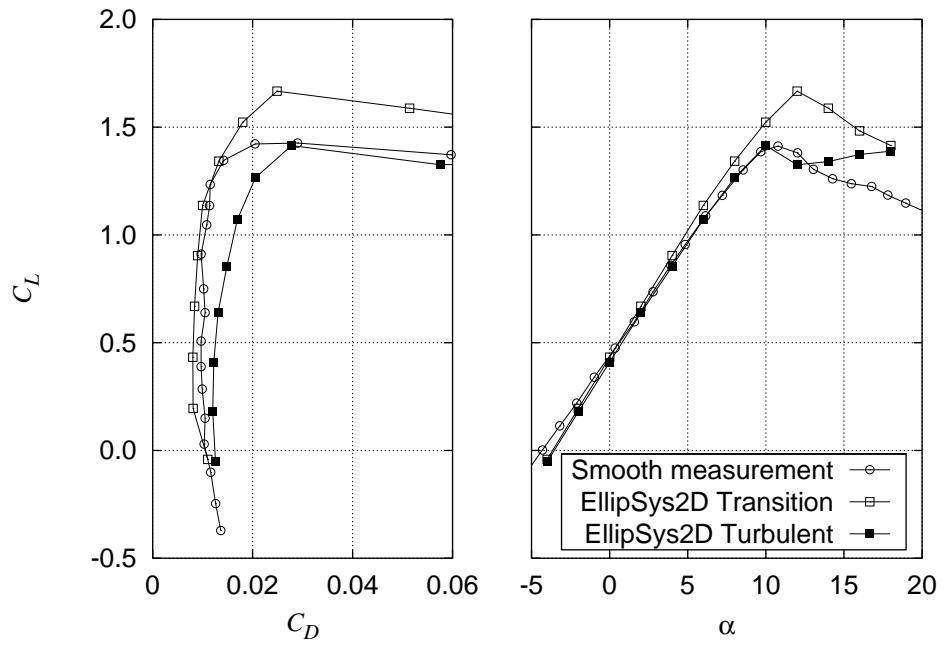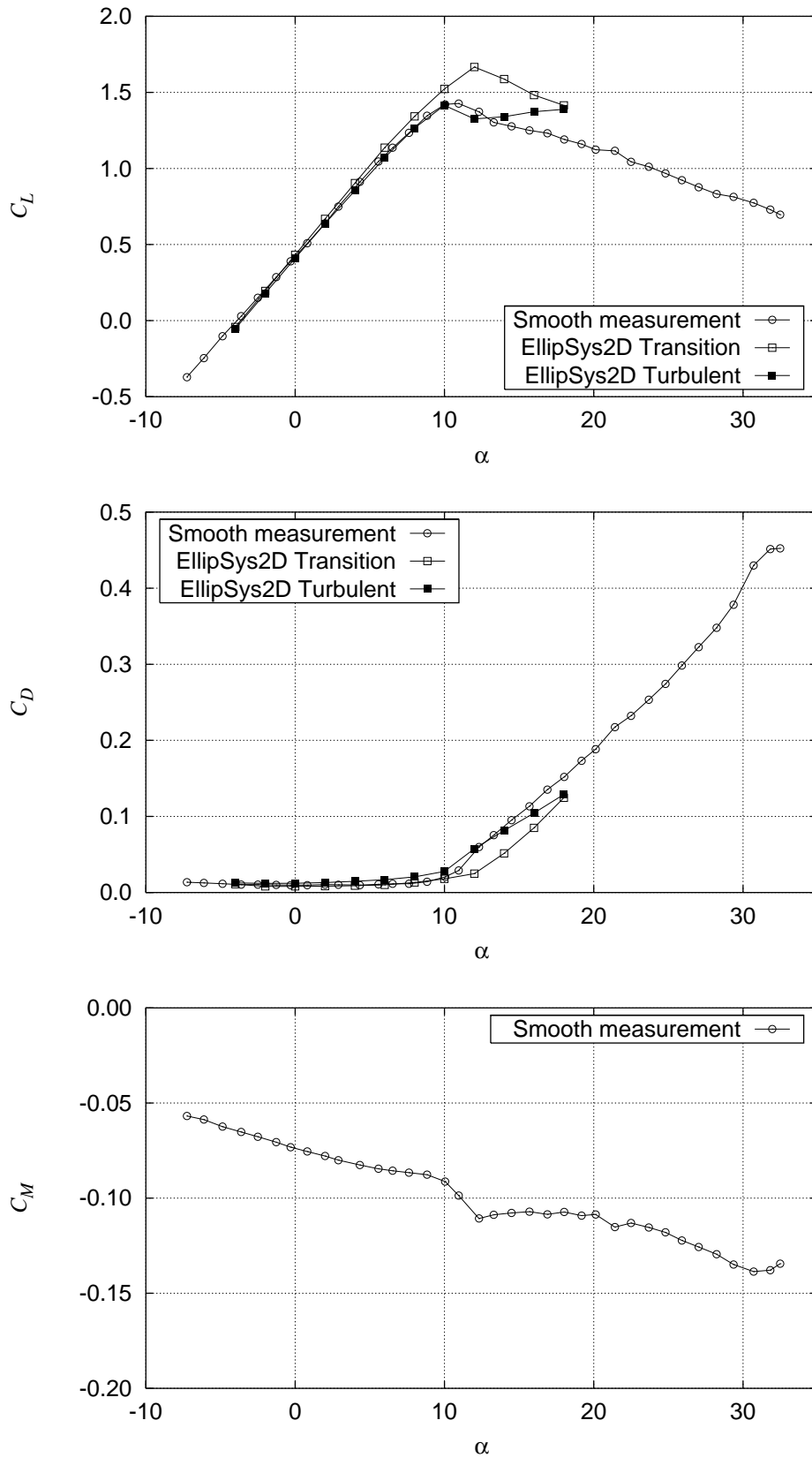

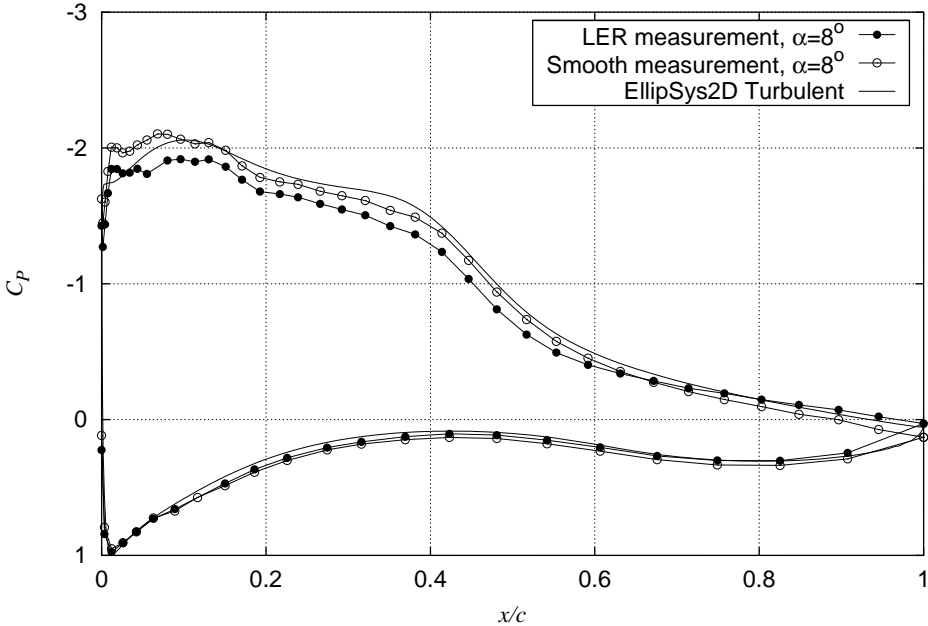*Figure 5-3 C_P at $\alpha = 8°$ for Risø-A1-18 smooth measurement compared with EllipSys2D calculations with transition modeling and turbulent flow respectively (run017).*

Figure 5-4 C_L-C_D for Risø-A1-18 smooth measurement compared with EllipSys2D calculations with transition modeling and turbulent flow respectively (run017).

Figure 5-5 C_L, C_D and C_M for Risø-A1-18 smooth measurement compared with EllipSys2D calculations with transition modeling and turbulent flow respectively (run017).

5.2   Risø-A1-18 LER (run016)

Figure 5-6 C_P at $\alpha = 8°$ for Risø-A1-18 LER measurement compared with smooth measurement and EllipSys2D calculations with turbulent flow (run016).
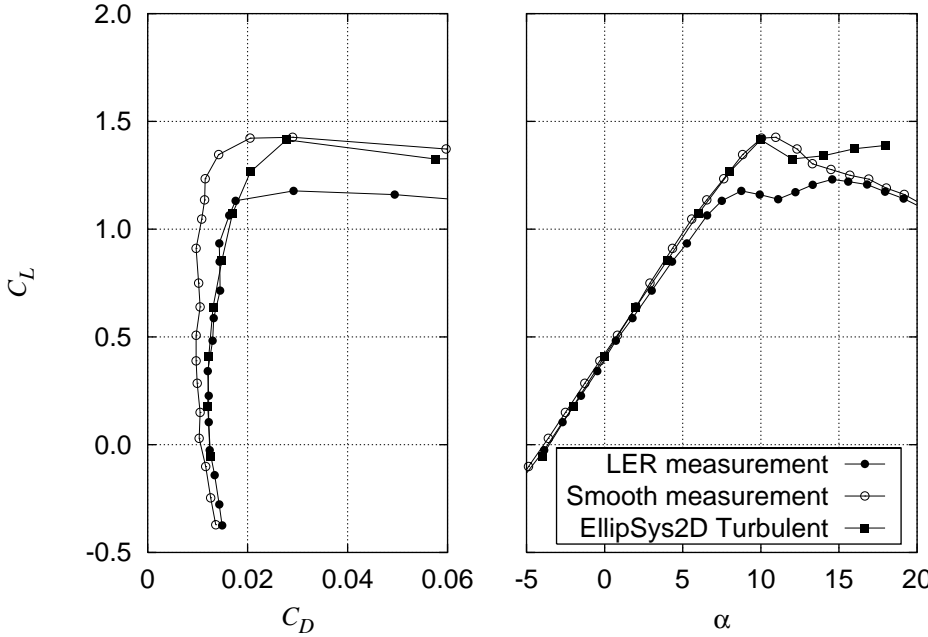
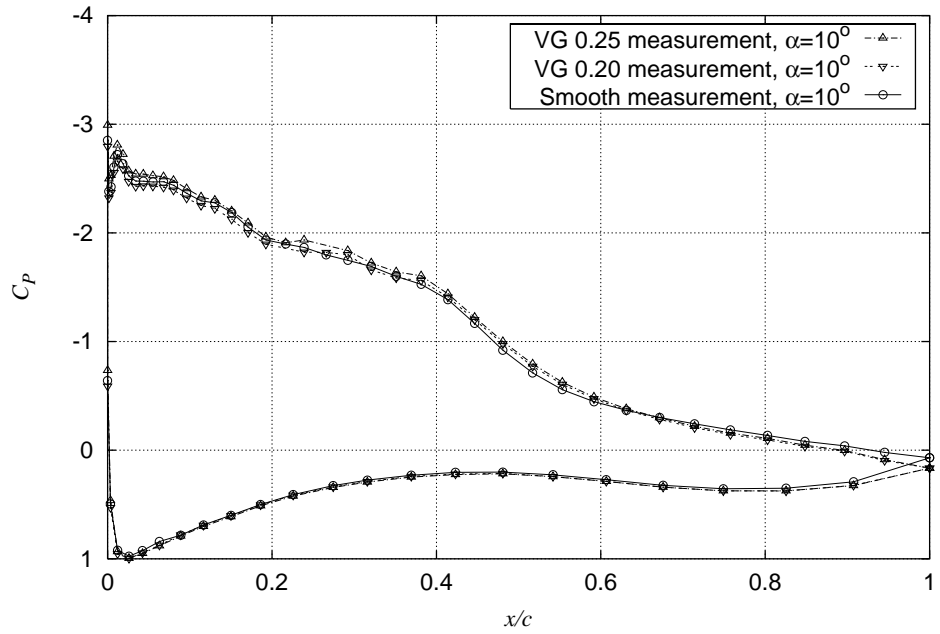*Figure 5-7 C_L-C_D for Risø-A1-18 LER measurement compared with smooth measurement and EllipSys2D calculations with turbulent flow (run016).*
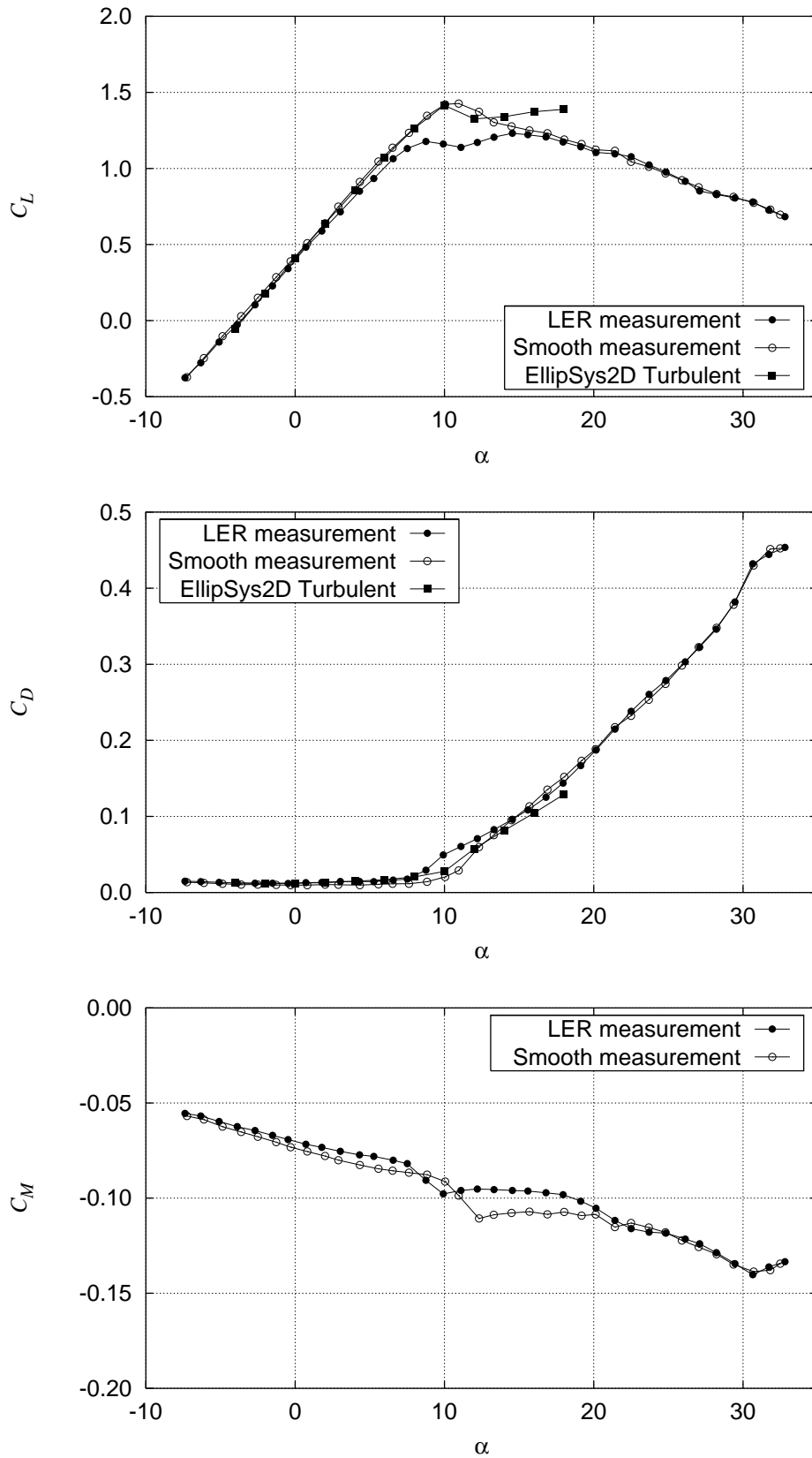
Figure 5-8 C_L, C_D and C_M for Risø-A1-18 LER measurement compared with smooth measurement and EllipSys2D calculations with turbulent flow (run016).

5.3   Risø-A1-18 VGs (run014, 020)

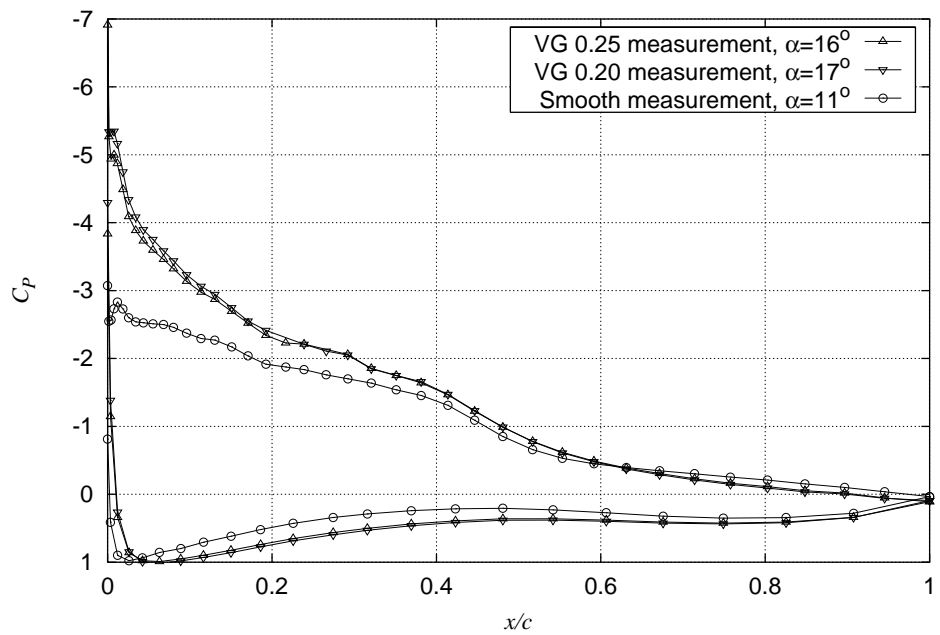Figure 5-9 C_P at $\alpha = 10^o$ for Risø-A1-18 VG measurements compared with smooth measurement (run014,020)

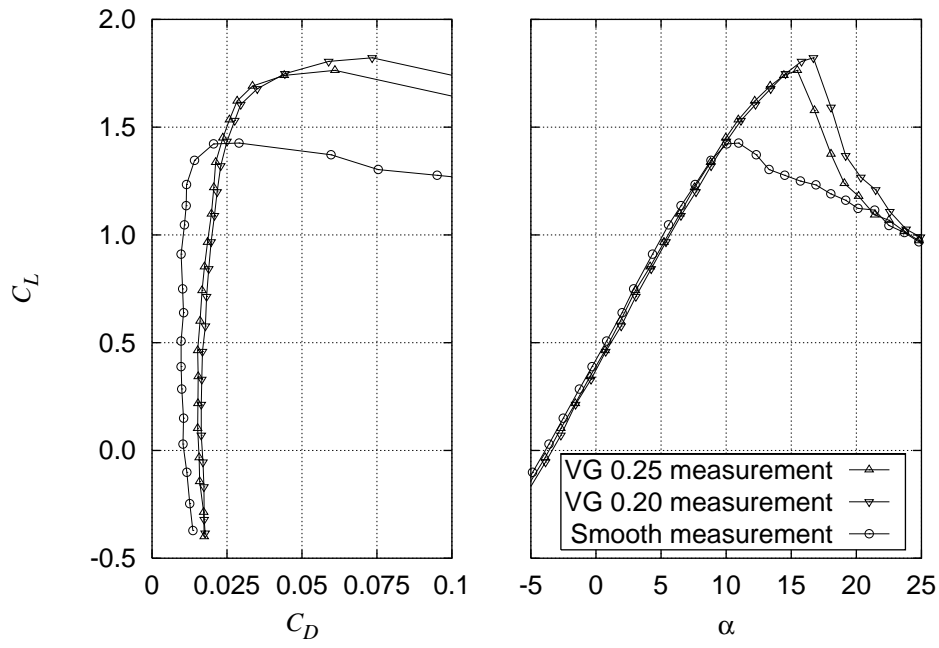Figure 5-10 C_p at maximum C_L for Risø-A1-18 VG measurements compared with smooth measurement (run014,020).

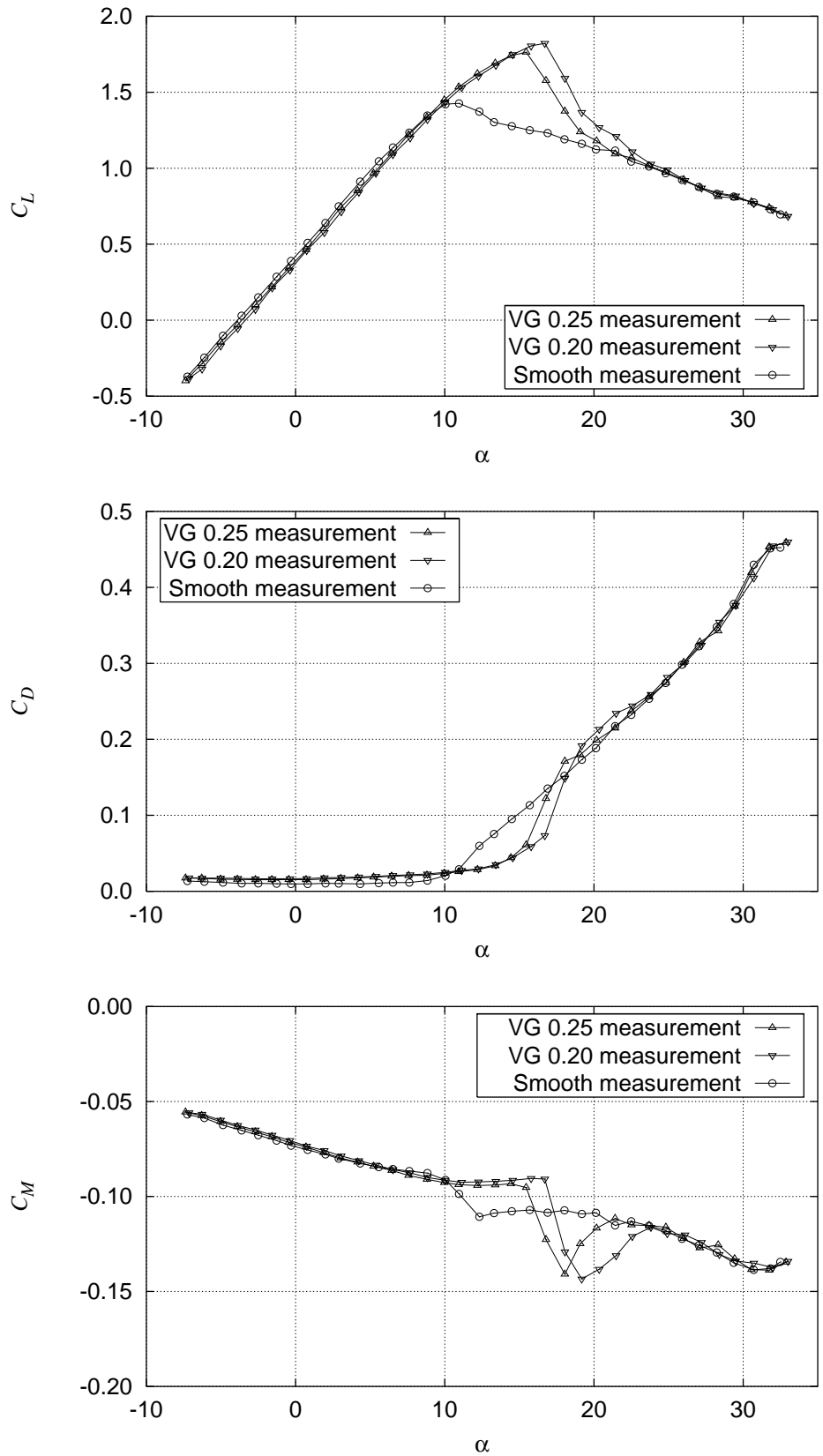*Figure 5-11 C_L-C_D for Risø-A1-18 VG measurements compared with smooth measurement (run014,020).*

Figure 5-12 C_L, C_D and C_M for Risø-A1-18 VG measurements compared with smooth measurement (run014, 020).

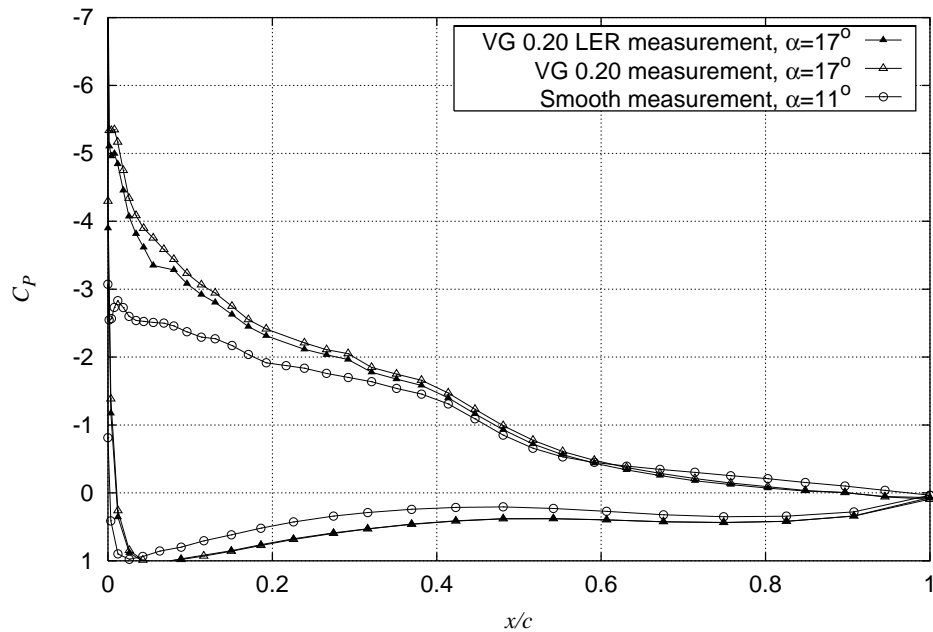## 5.4   Risø-A1-18 VGs at 0.2 (run014, 015)

Figure 5-13 C_p at maximum C_L for Risø-A1-18 VG 20% Smooth and LER measurement compared with smooth measurements (run014,015).
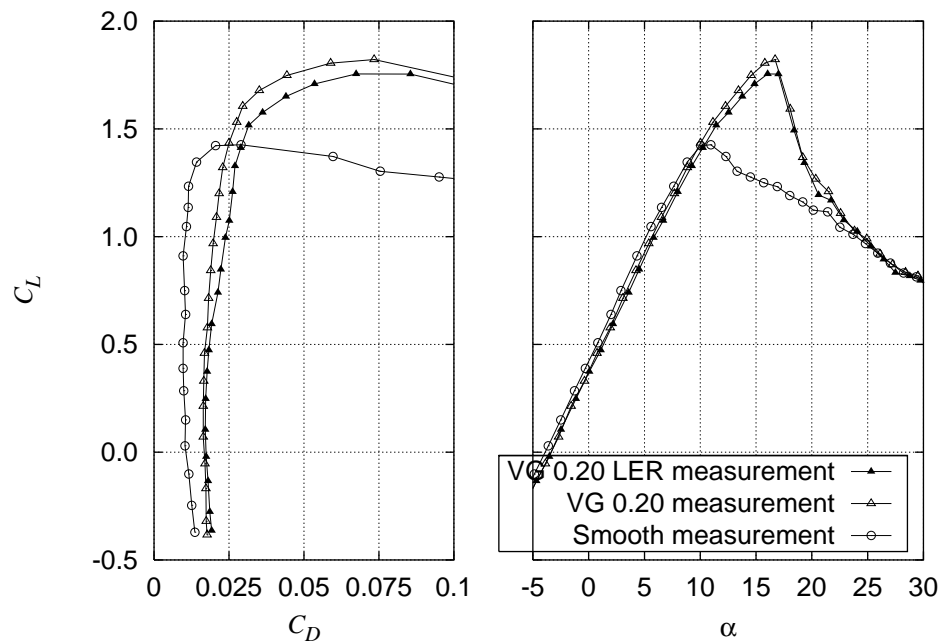

Figure 5-14 C_L-C_D for Risø-A1-18 VG 20% Smooth and LER measurement compared with smooth measurements (run014,015).
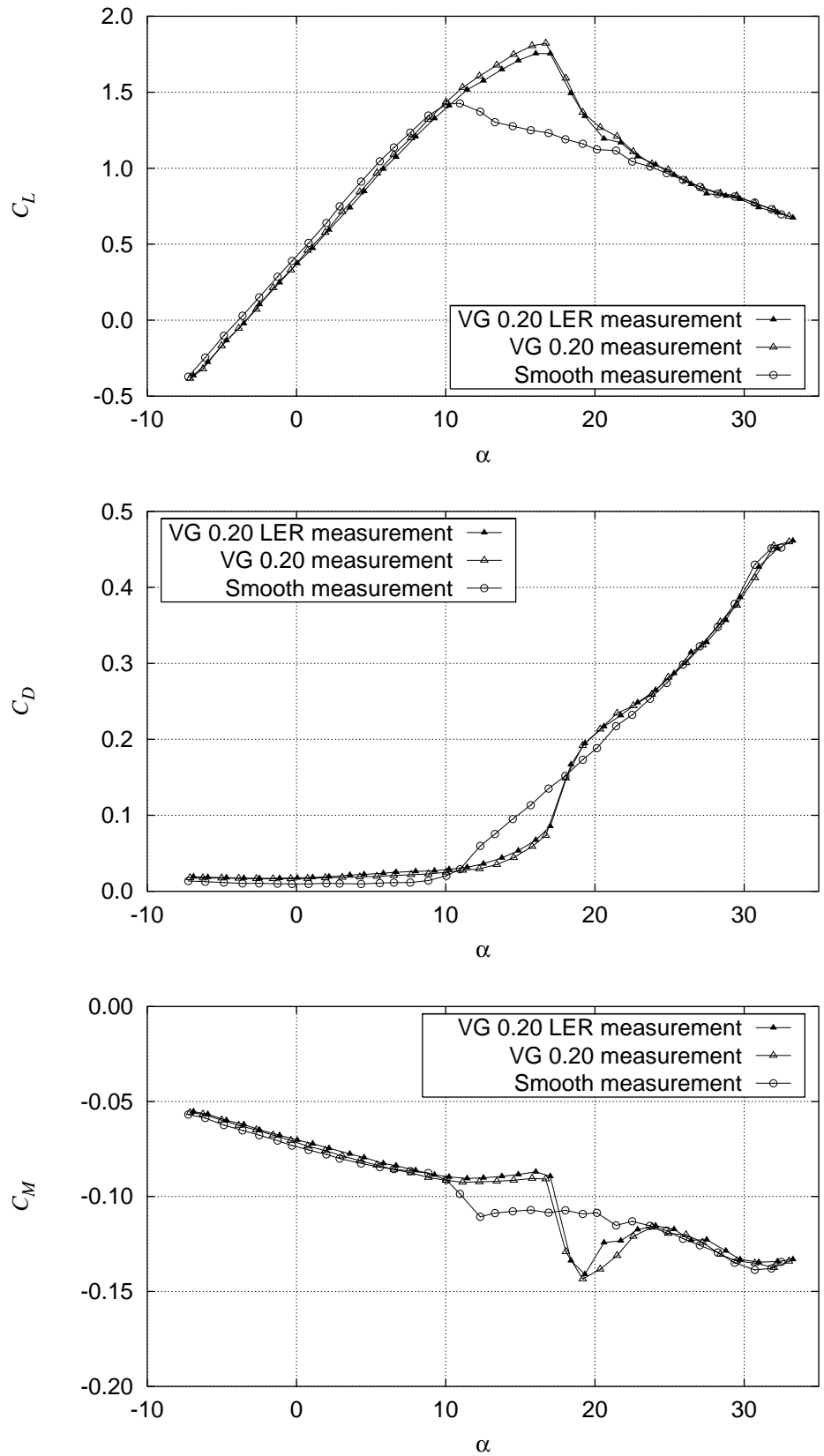
Figure 5-15 C_L, C_D and C_M for Risø-A1-18 VG 20% Smooth and LER measurement compared with smooth measurements (run014,015).
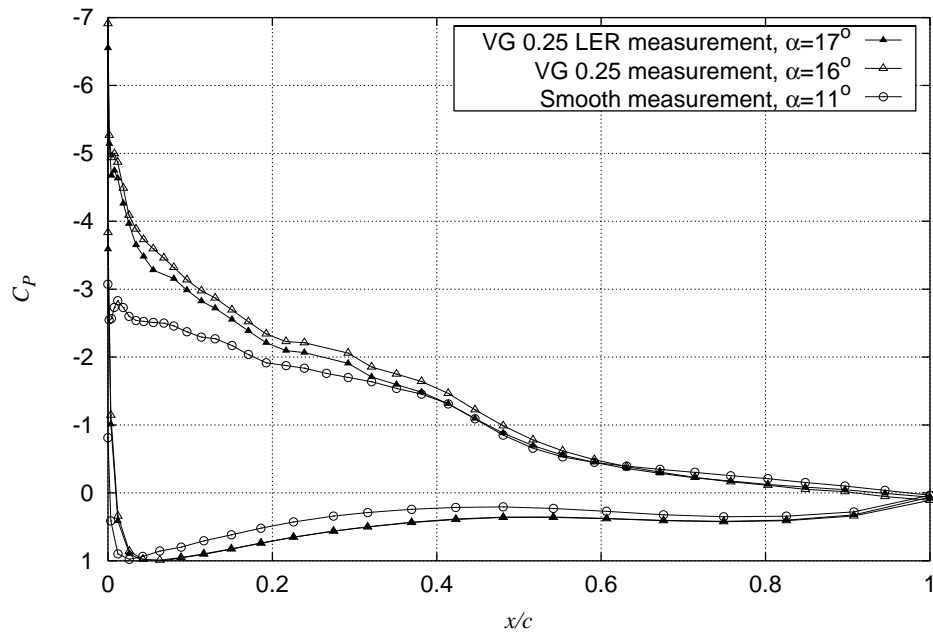
5.5 Risø-A1-18 VGs at 0.25 (run020, 021)

Figure 5-16 C_p at maximum C_L for Risø-A1-18 VG 25% Smooth and LER measurement compared with smooth measurements (run020,021).
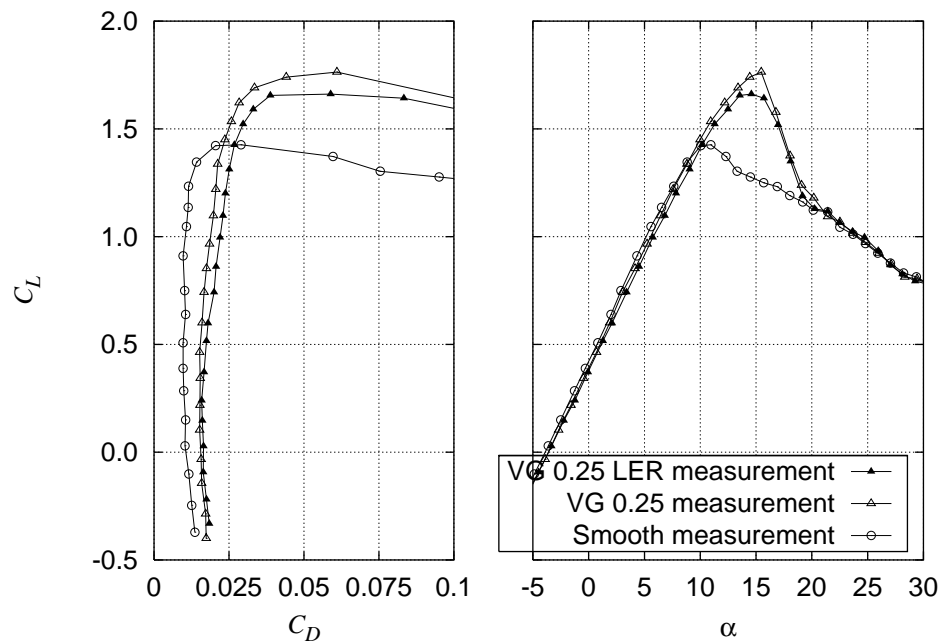

Figure 5-17 C_L-C_D for Risø-A1-18 VG 25% Smooth and LER measurement compared with smooth measurements (run020,021).
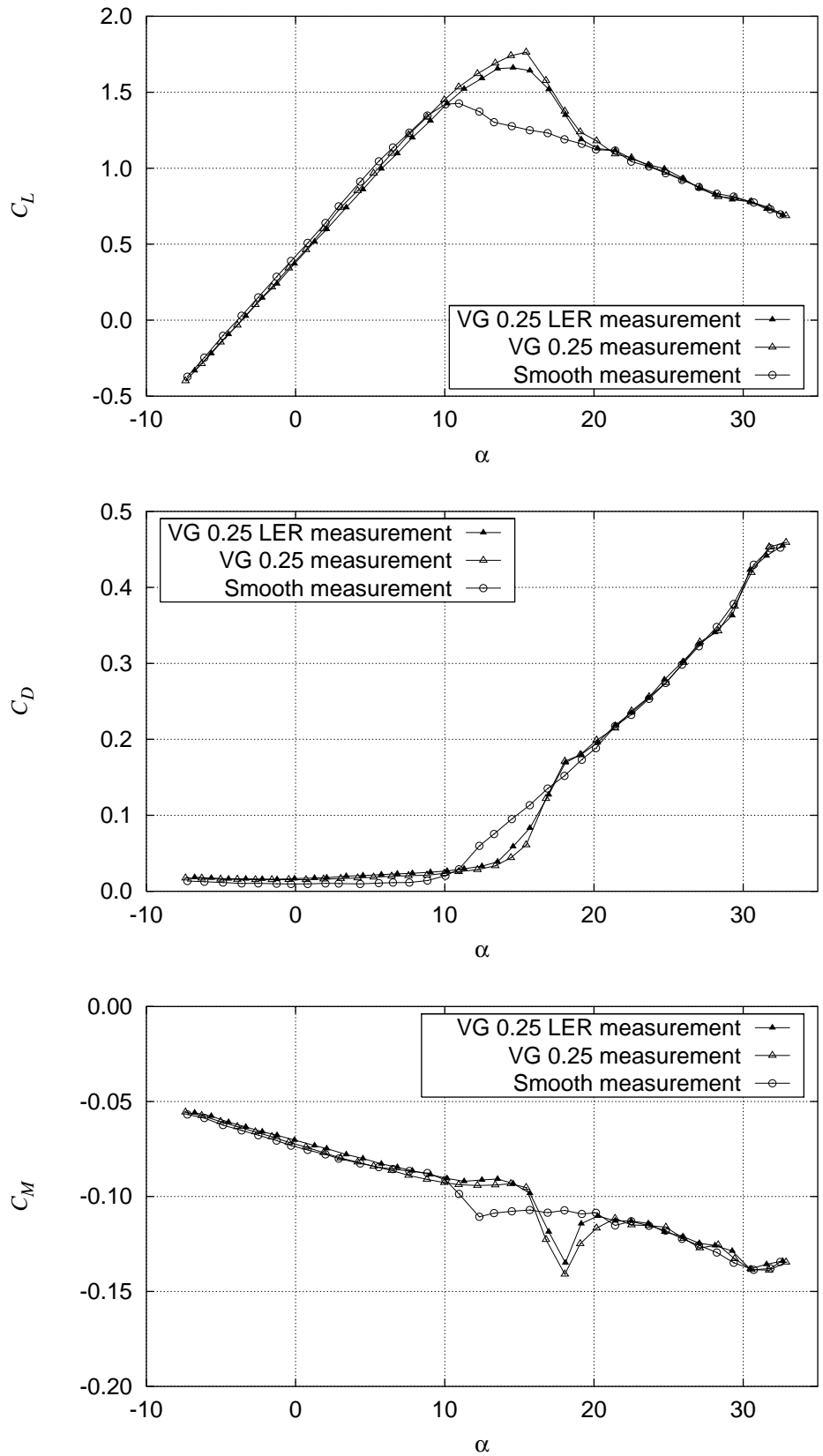
Figure 5-18 C_L, C_D and C_M for Risø-A1-18 VG 25% Smooth and LER measurement compared with smooth measurements (run020,021).
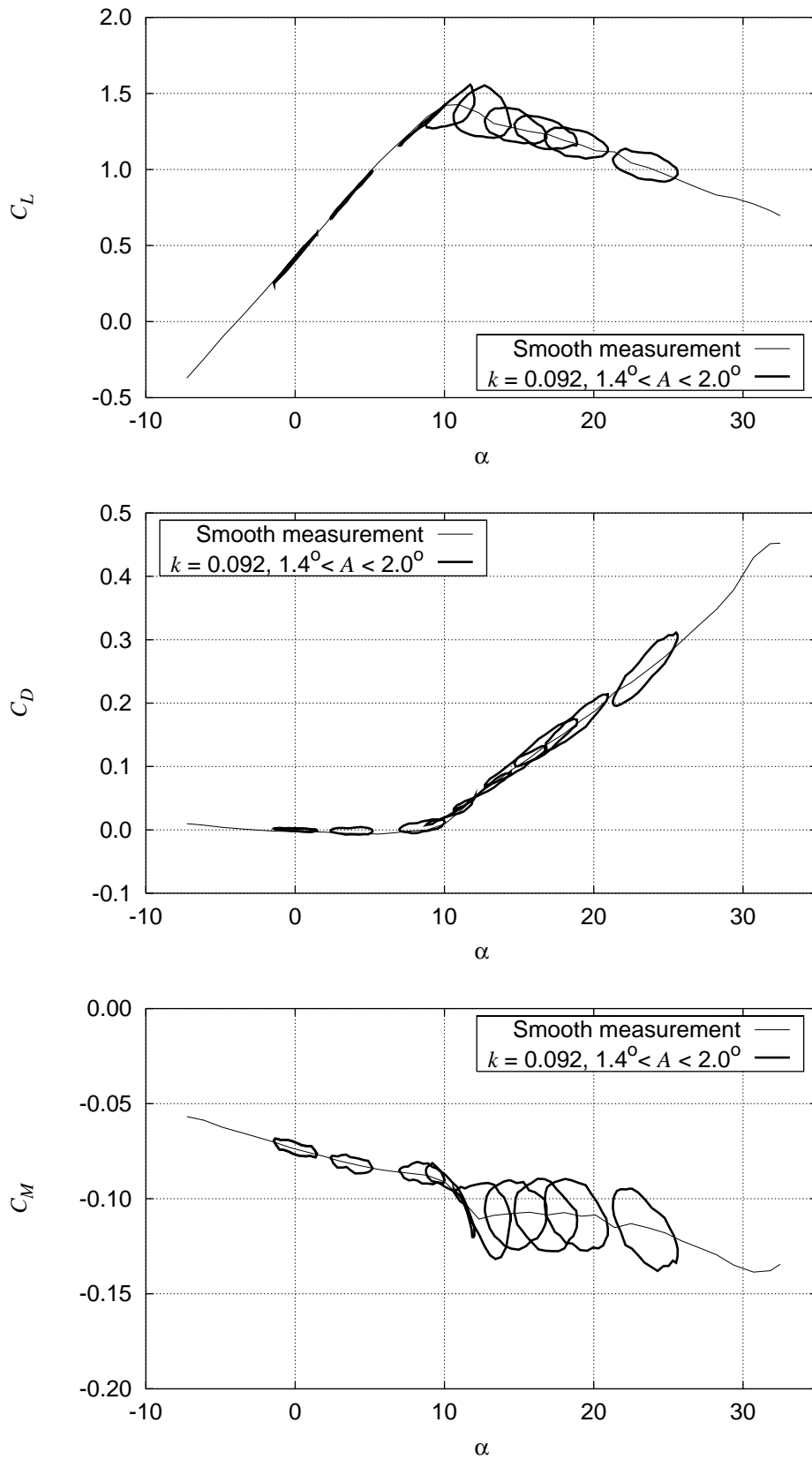
5.6 Risø-A1-18 Dynamic stall (run022)

Figure 5-19 C_L, C_D and C_M hysteresis loops for Risø-A1-18 smooth measurement at k = 0.092, A between 1.4° and 2.0° (run022).
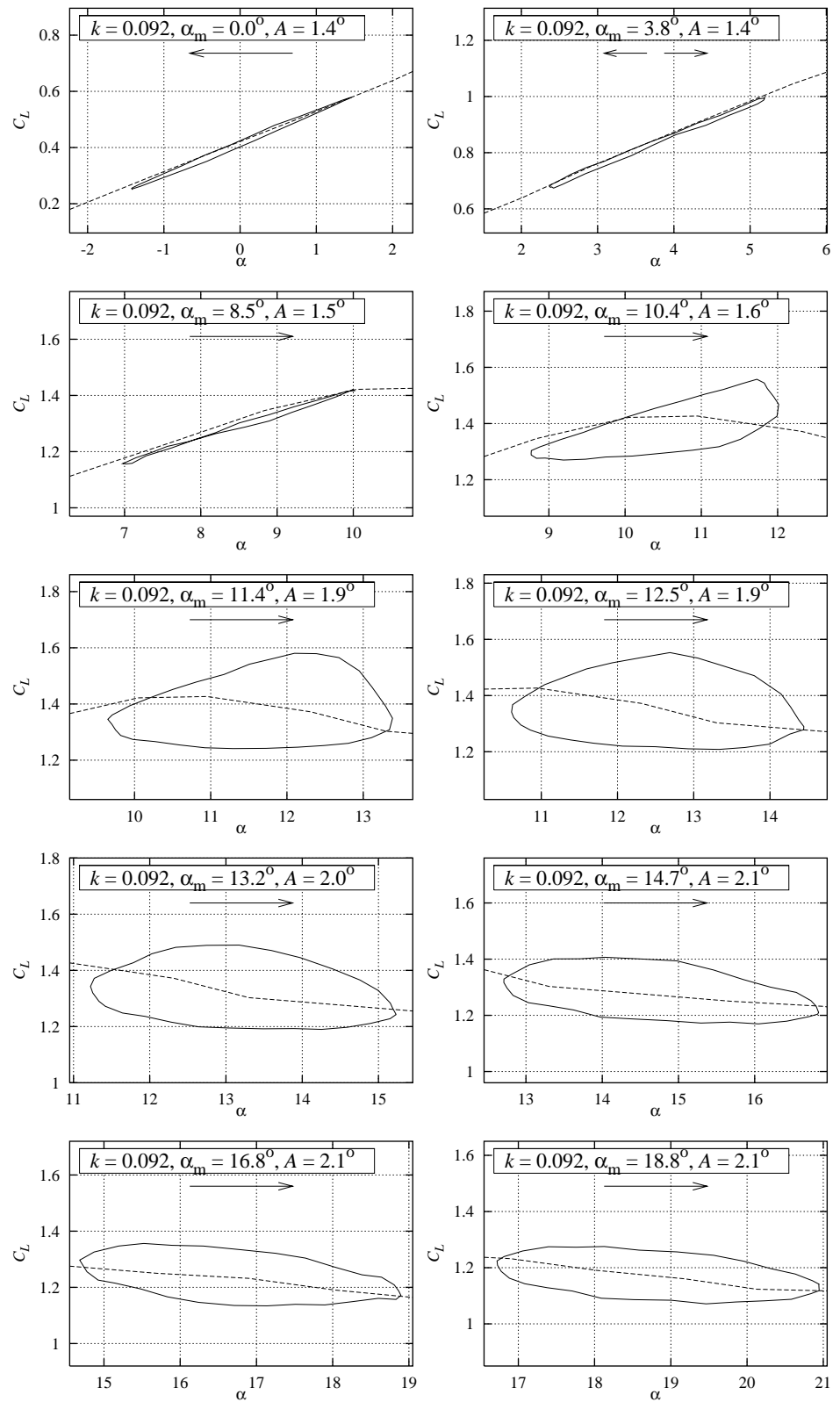
Figure 5-20 C_L hysteresis loops for Risø-A1-18 smooth measurement at k = 0.092, A between 1.4° and 2.0° (run022).

Figure 5-21 C_D hysteresis loops for Risø-A1-18 smooth measurement at k = 0.092, A between 1.4° and 2.0° (run022).
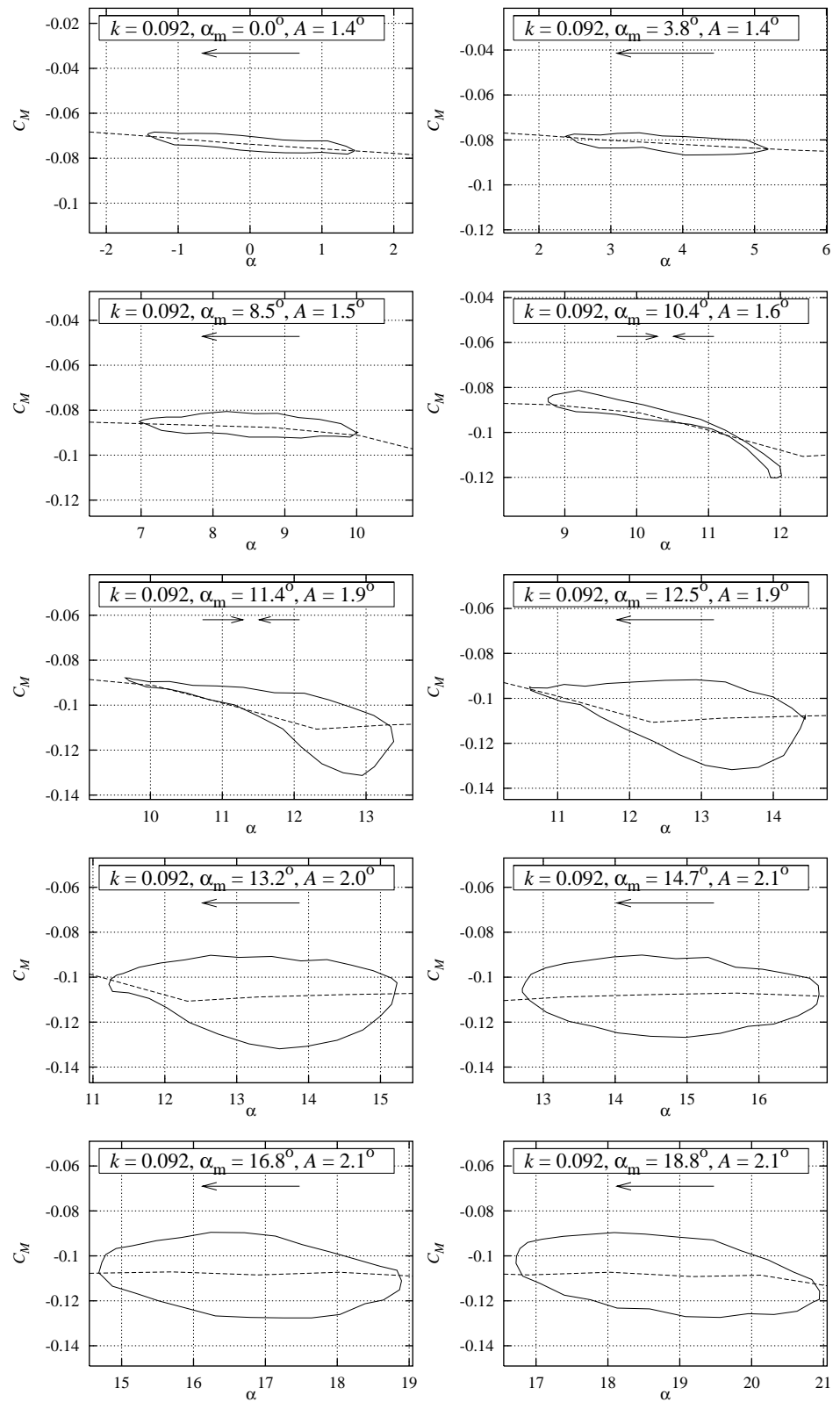
Figure 5-22 C_M hysteresis loops for Risø-A1-18 smooth measurement at k = 0.092, A between 1.4° and 2.0° (run022).
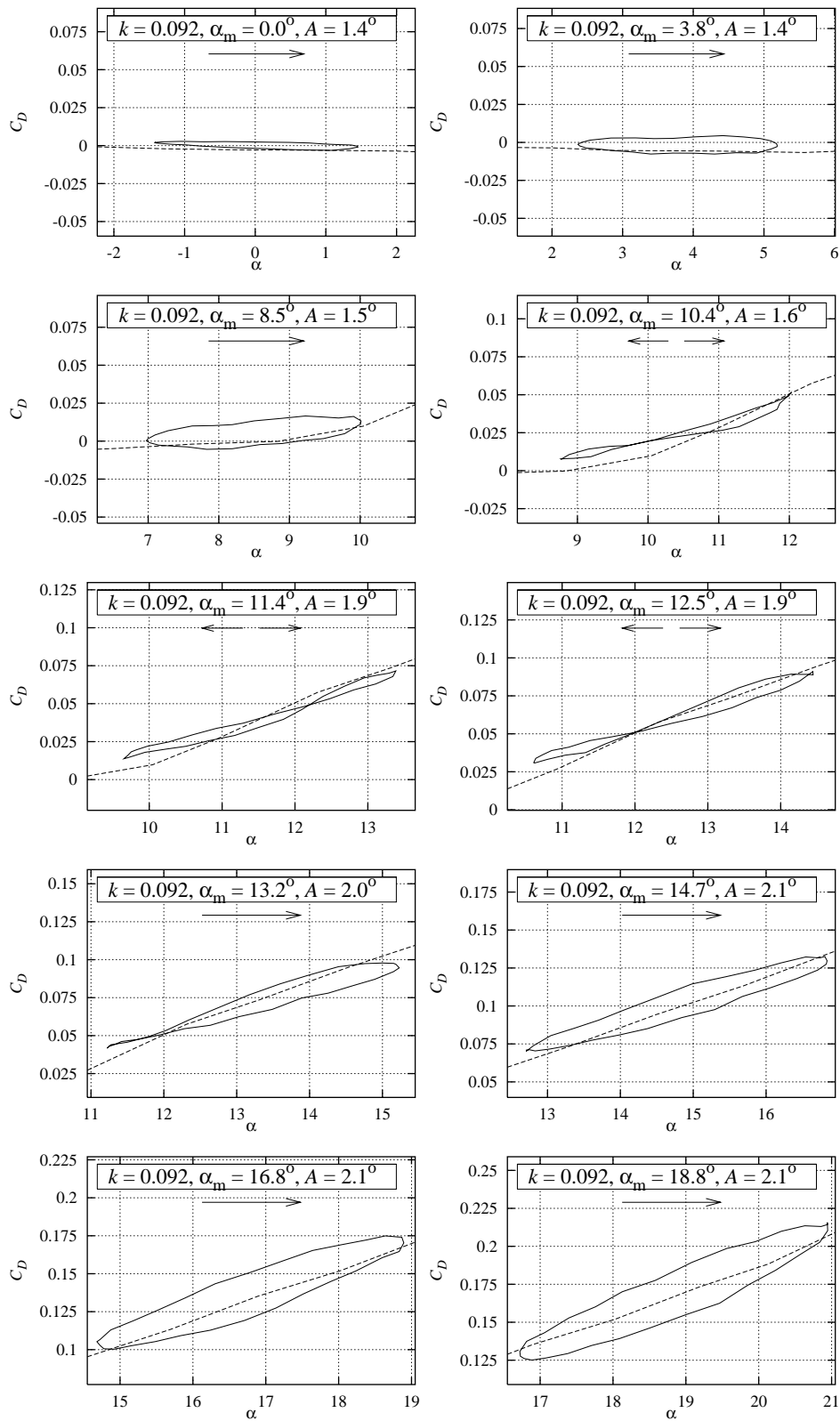
6 Results for Risø-A1-21

6.1 Risø-A1-21 Smooth flow (run025)
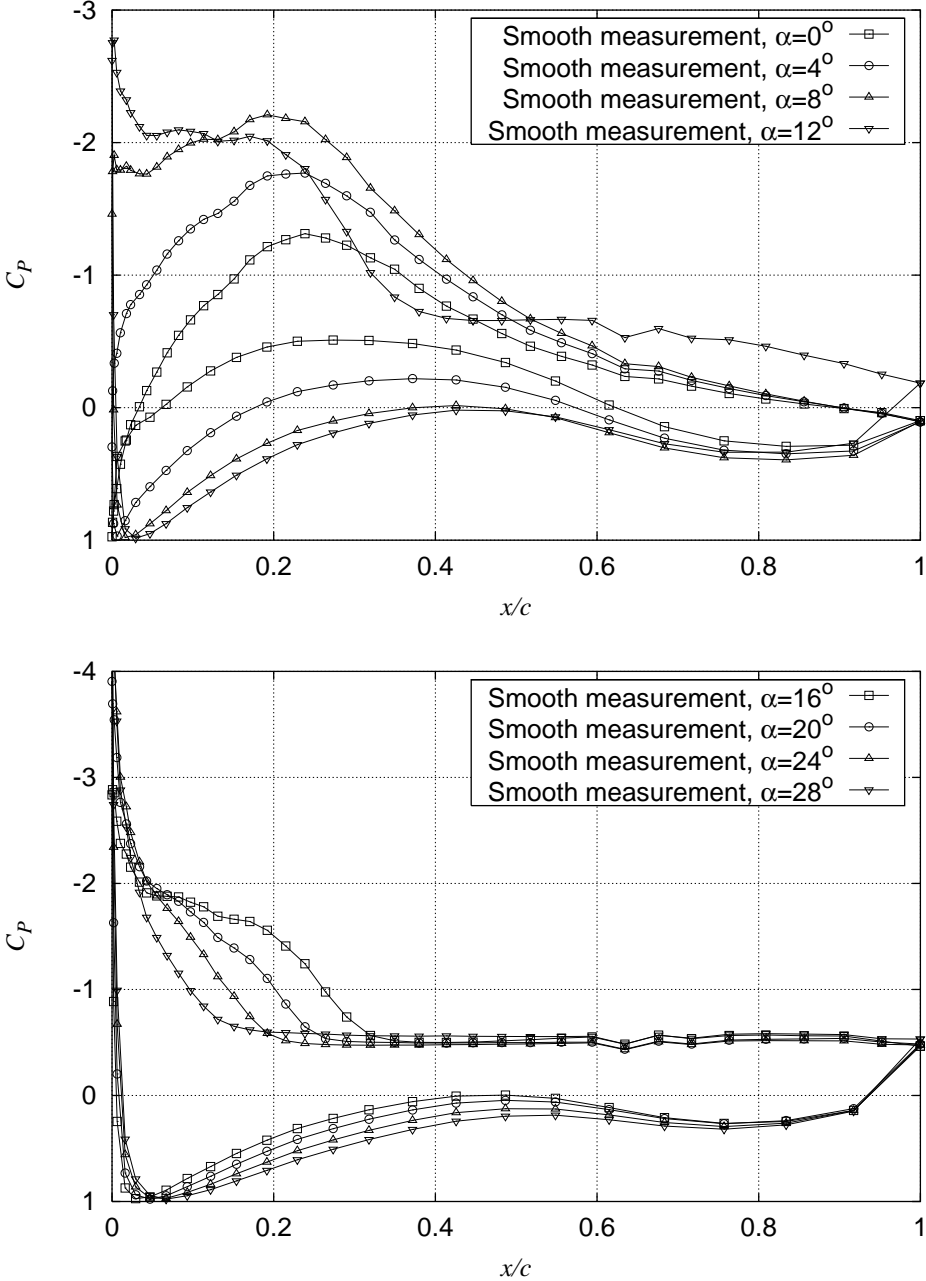
Figure 6-1 C_P at different angles of attack for Risø-A1-21 smooth measurement (run025).
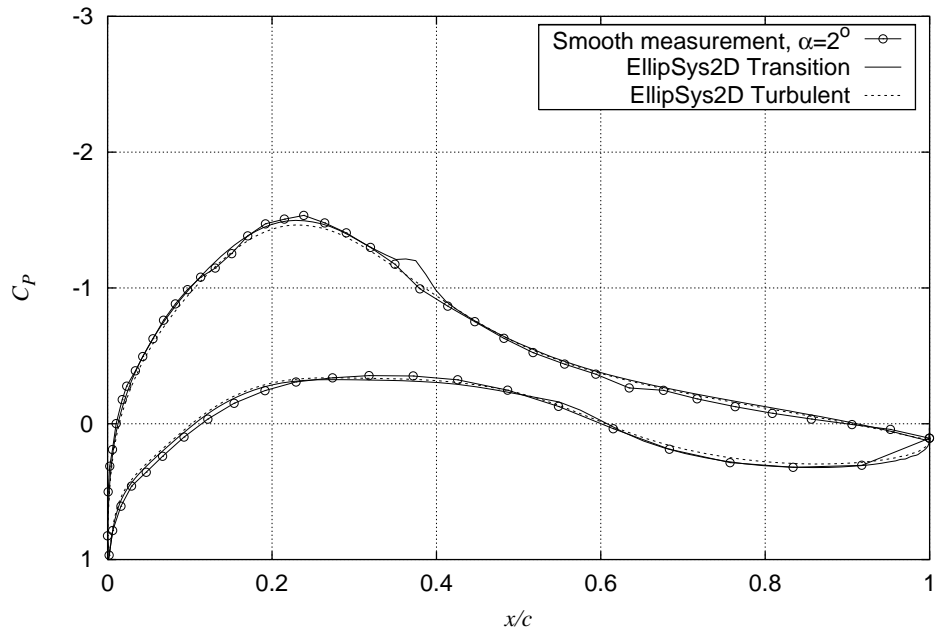
Figure 6-2 C_P at α = 2° for Risø-A1-21 smooth measurement compared with EllipSys2D calculations with transition modeling and turbulent flow respectively (run025).
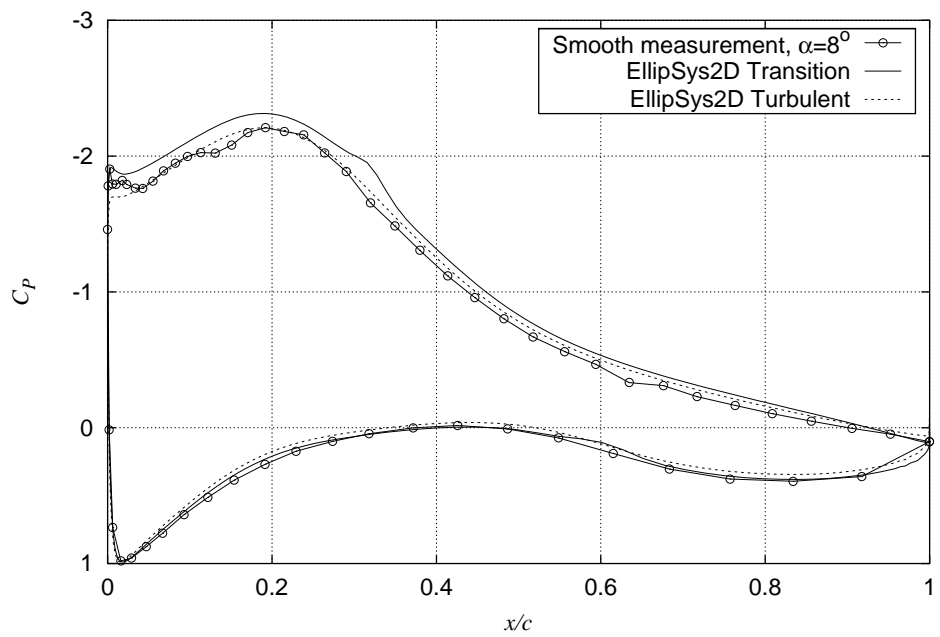
Figure 6-3 C_P at α = 8° for Risø-A1-21 smooth measurement compared with EllipSys2D calculations with transition modeling and turbulent flow respectively (run025).
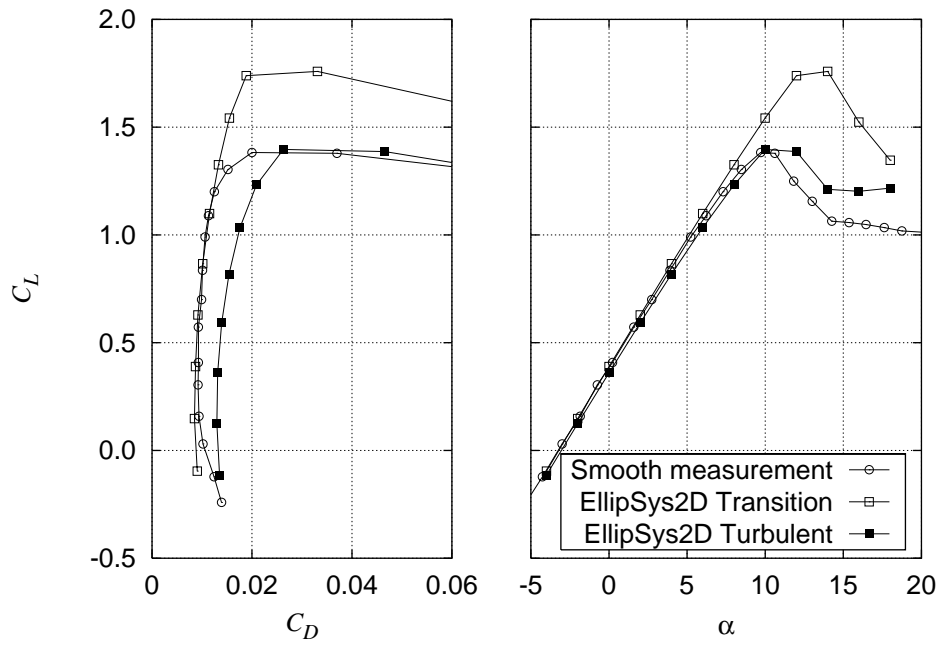
Figure 6-4 C_L-C_D for Risø-A1-21 smooth measurement compared with EllipSys2D calculations with transition modeling and turbulent flow respectively (run025).
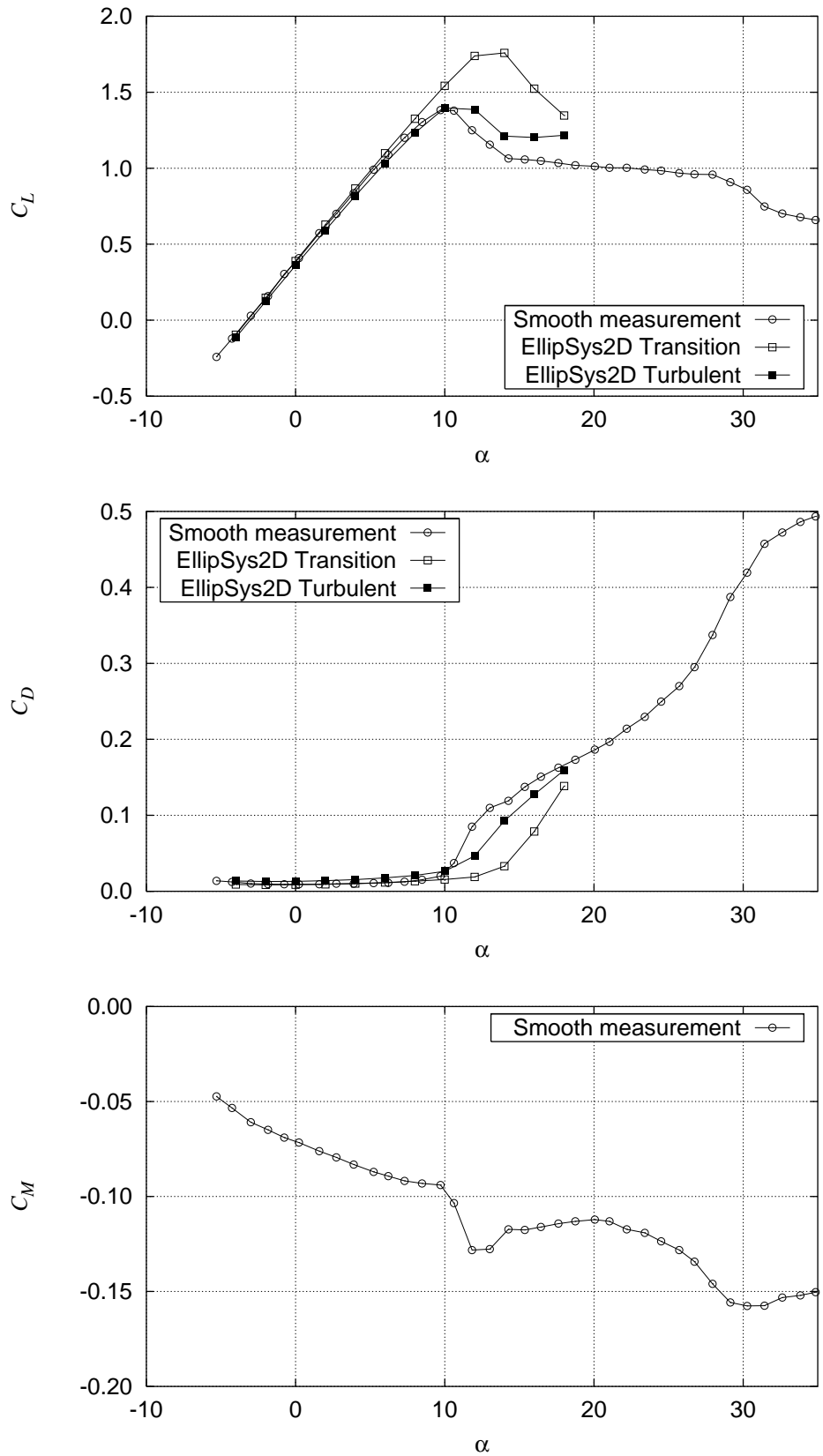
Figure 6-5 C_L, C_D and C_M for Risø-A1-21 smooth measurement compared with EllipSys2D calculations with transition modeling and turbulent flow respectively (run025).

6.2   Risø-A1-21 LER (run005)
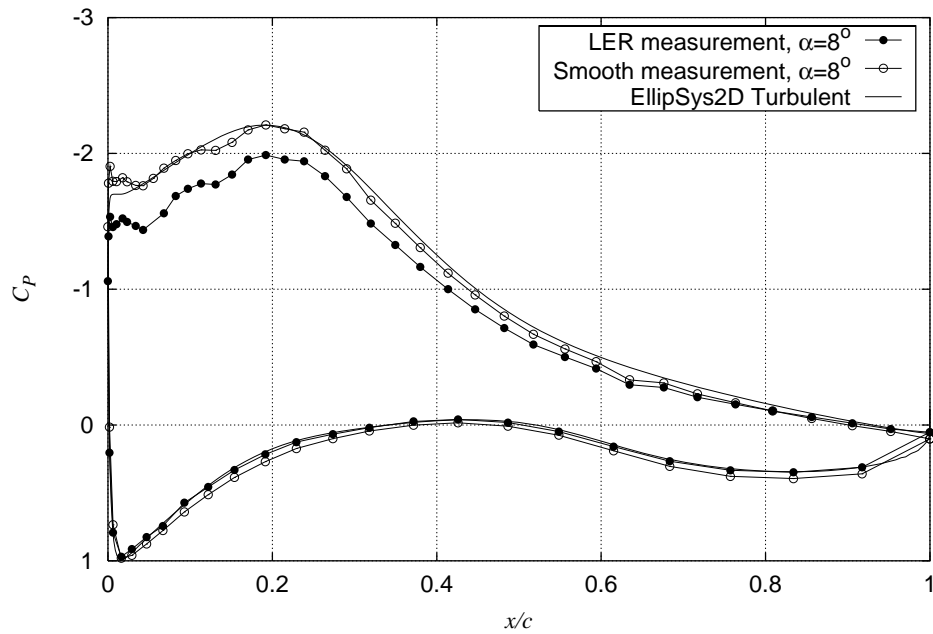
Figure 6-6 C_P at $\alpha = 8°$ for Risø-A1-21 LER measurement compared with smooth measurement and EllipSys2D calculations with turbulent flow (run005).
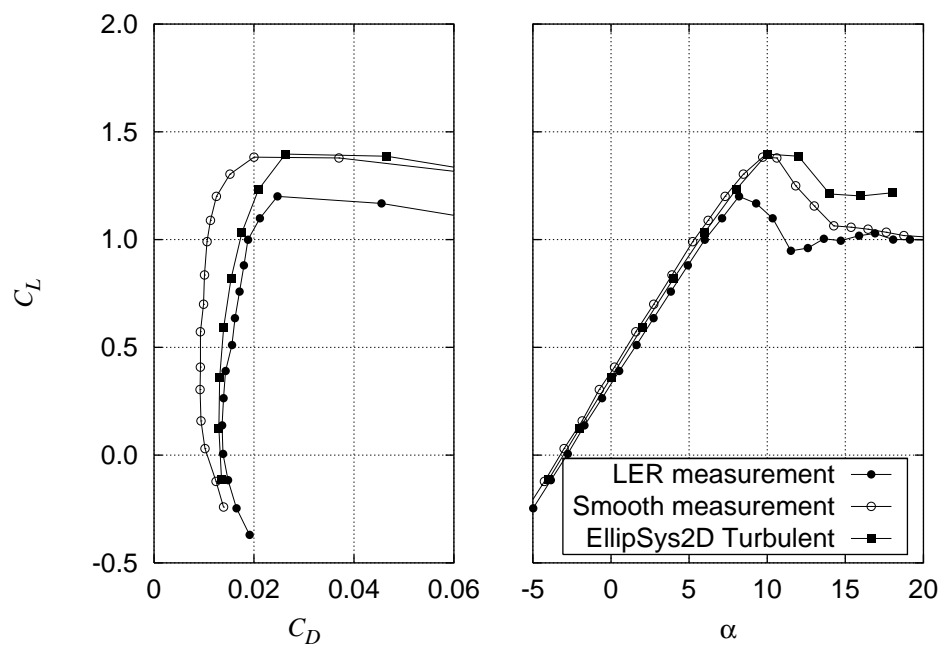
Figure 6-7 C_L-C_D for Risø-A1-21 LER measurement compared with smooth measurement and EllipSys2D calculations with turbulent flow (run005).
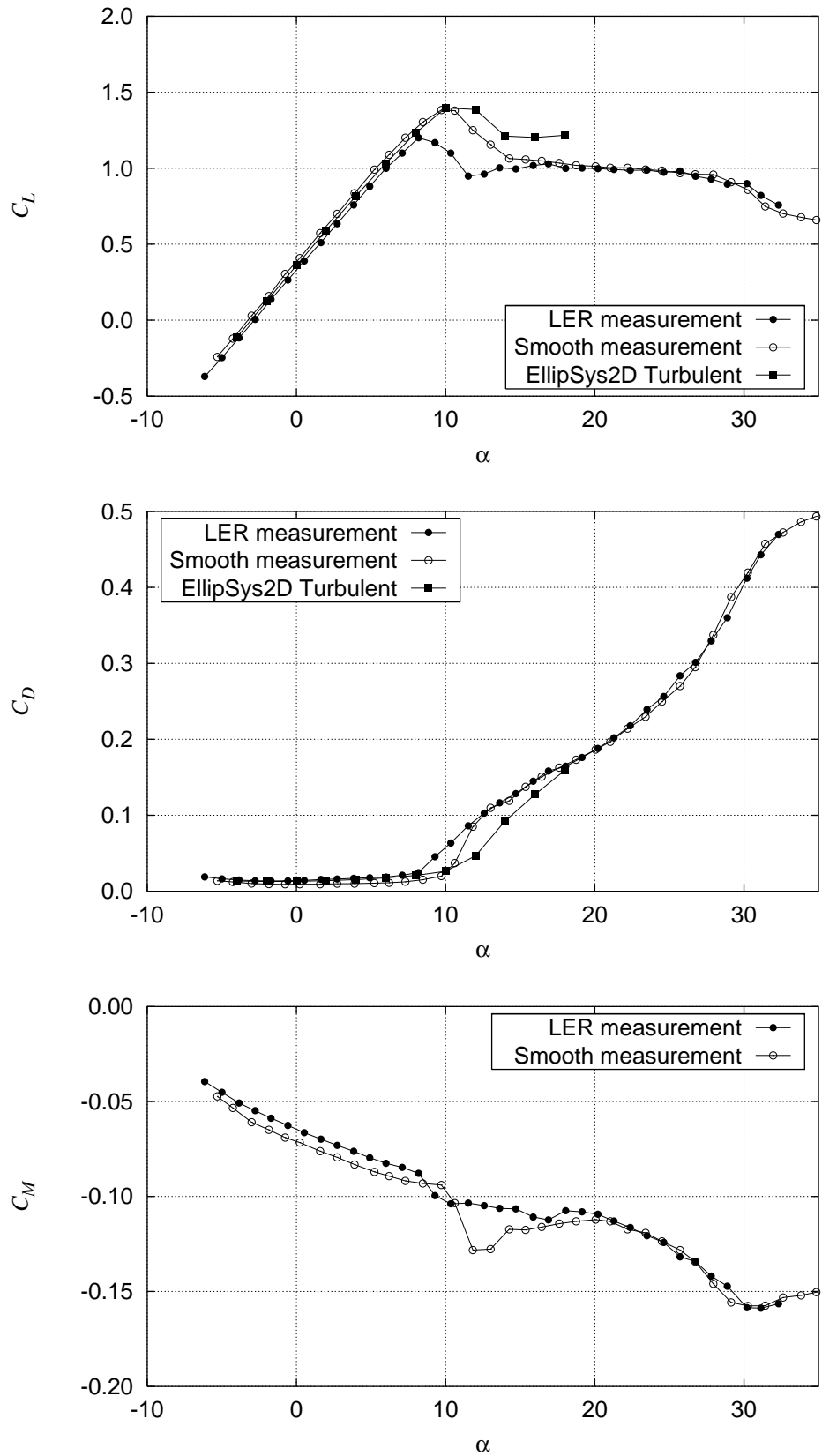
Figure 6-8 C_L, C_D and C_M for Risø-A1-21 LER measurement compared with smooth measurement and EllipSys2D calculations with turbulent flow respectively (run005).

6.3 Risø-A1-21 VGs (run003, 024)
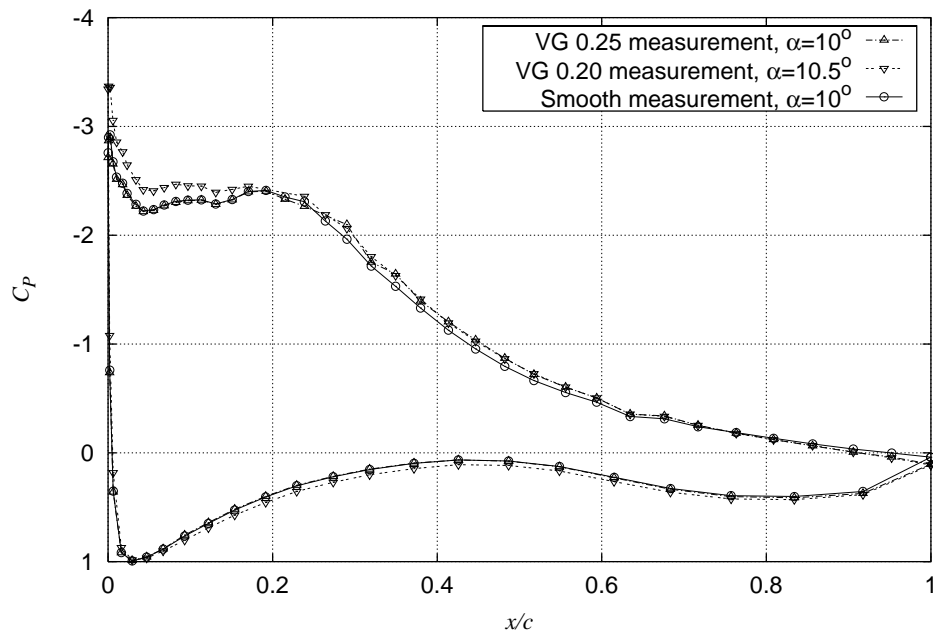
Figure 6-9 C_P at $\alpha = 10^o$ for Risø-A1-21 VG measurements compared with smooth measurement (run003, 024).
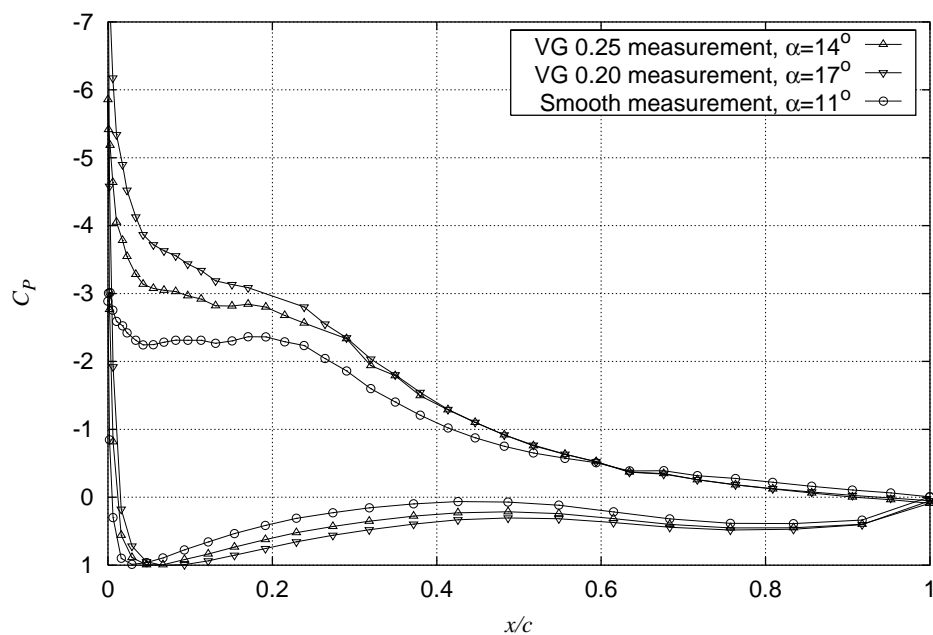
Figure 6-10 C_p at maximum C_L for Risø-A1-21 VG measurements compared with smooth measurement (run003, 024).
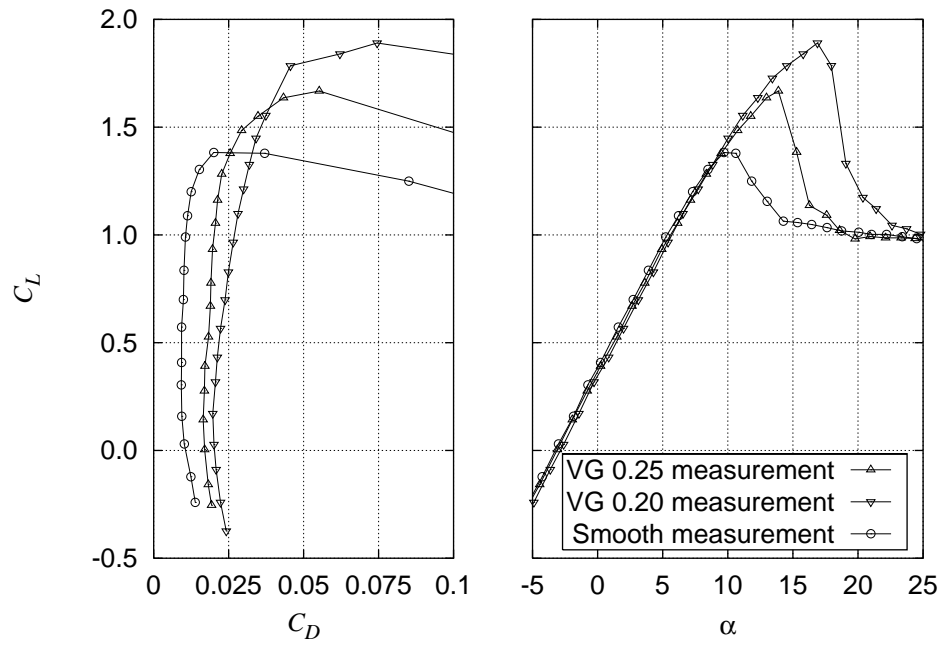
Figure 6-11 C_L-C_D for Risø-A1-21 VG measurements compared with smooth measurement (run003, 024).
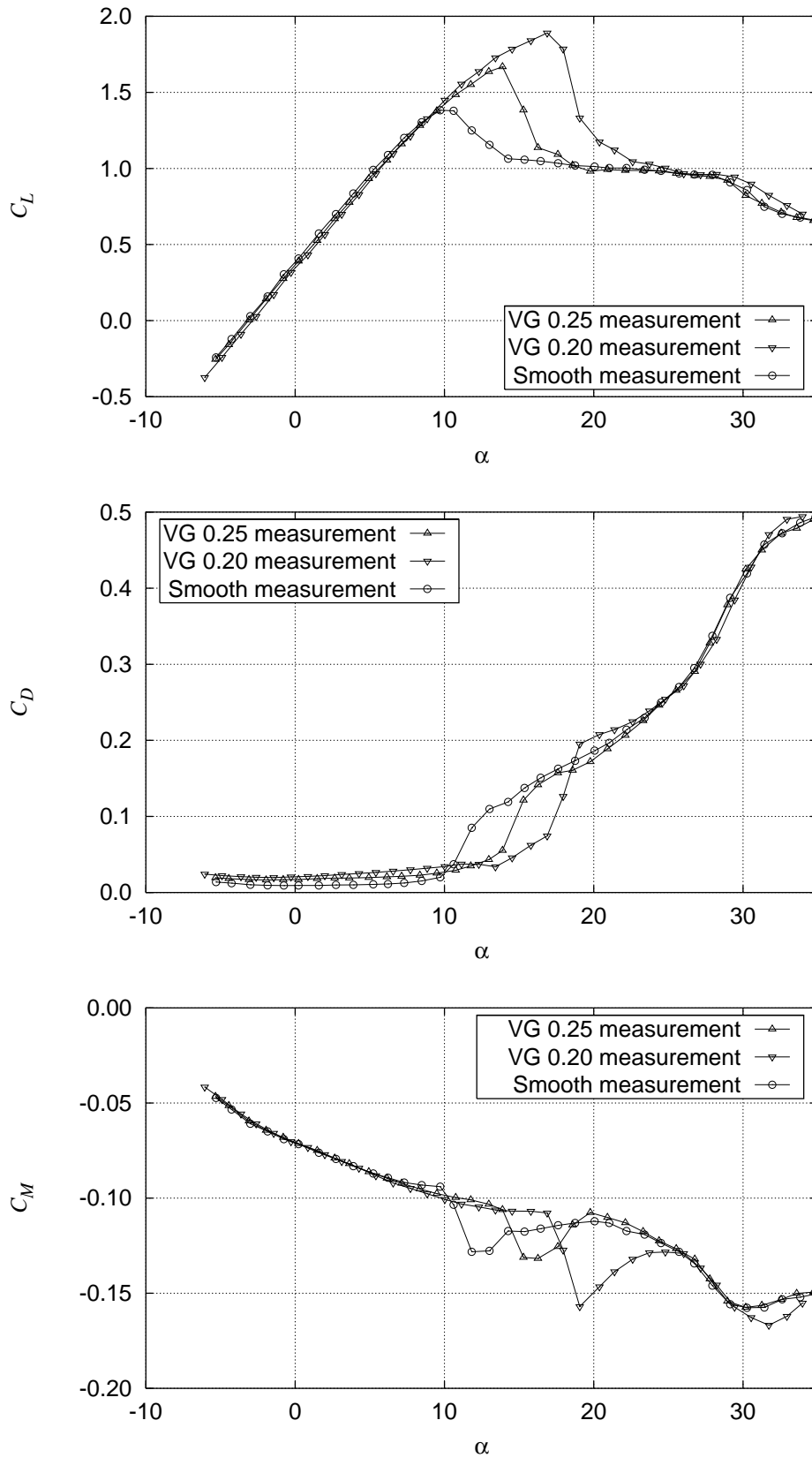
Figure 6-12 C_L, C_D and C_M for Risø-A1-21 VG measurements compared with smooth measurement (run003, 024).

6.4 Risø-A1-21 VGs at 0.2 (run003, 004)
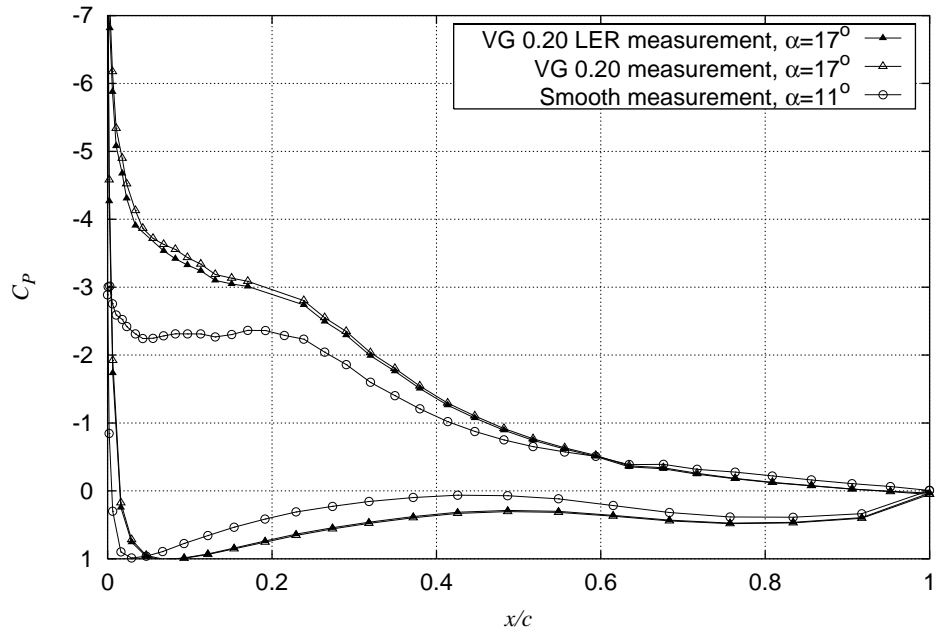
Figure 6-13 C_p at maximum C_L for Risø-A1-21 VG 20% Smooth and LER measurement compared with smooth measurements (run003,004).
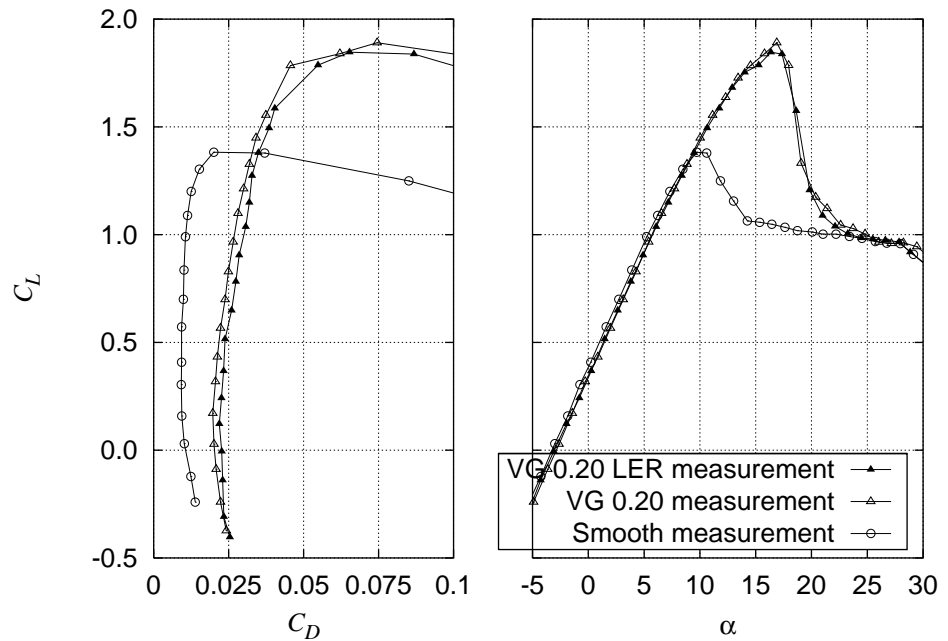
Figure 6-14 C_L-C_D for Risø-A1-21 VG 20% Smooth and LER measurement compared with smooth measurements (run003,004).
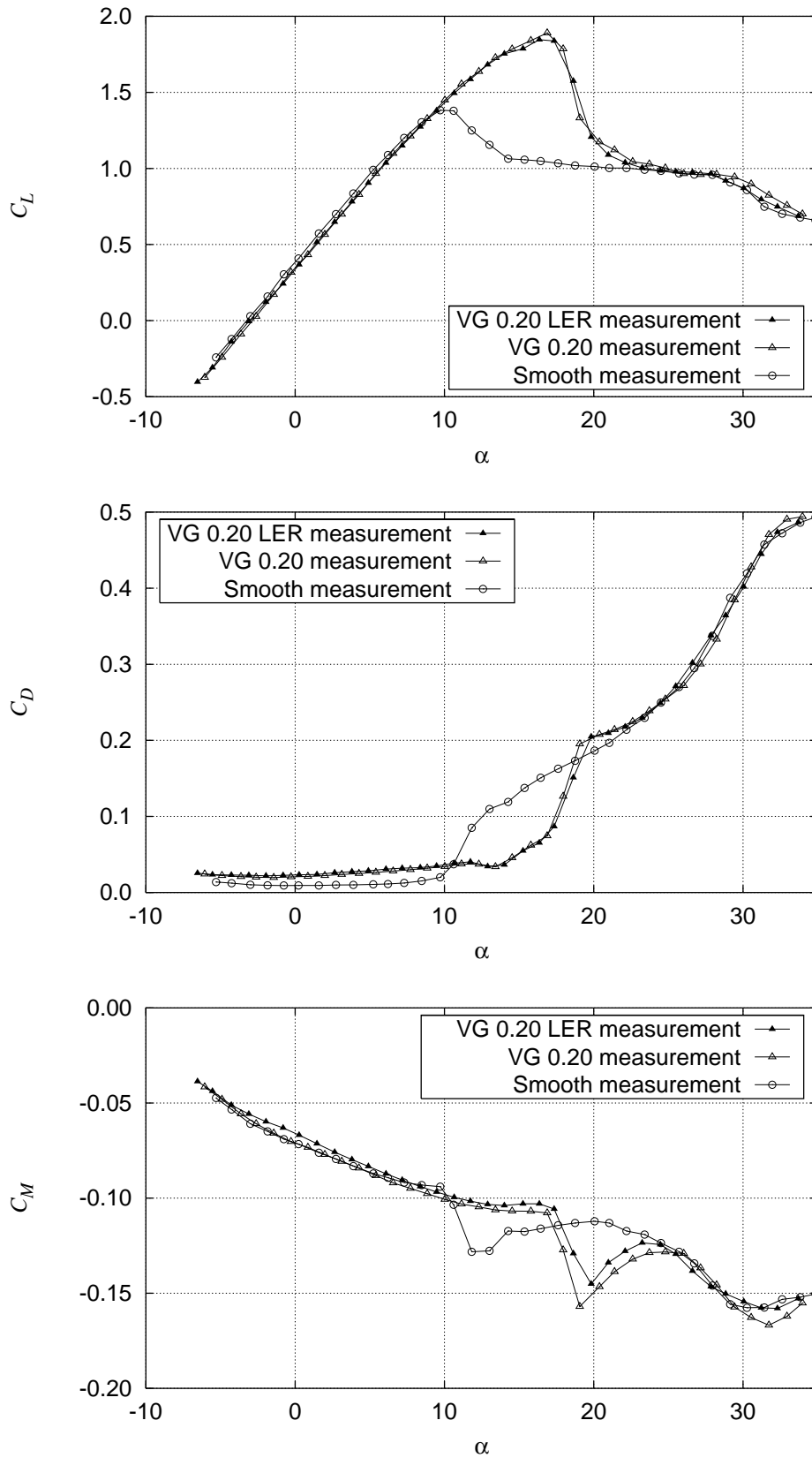
Figure 6-15 C_L, C_D and C_M for Risø-A1-21 VG 20% Smooth and LER measurement compared with smooth measurements (run003 004).

6.5   Risø-A1-21 VGs at 0.25 (run023, 024)
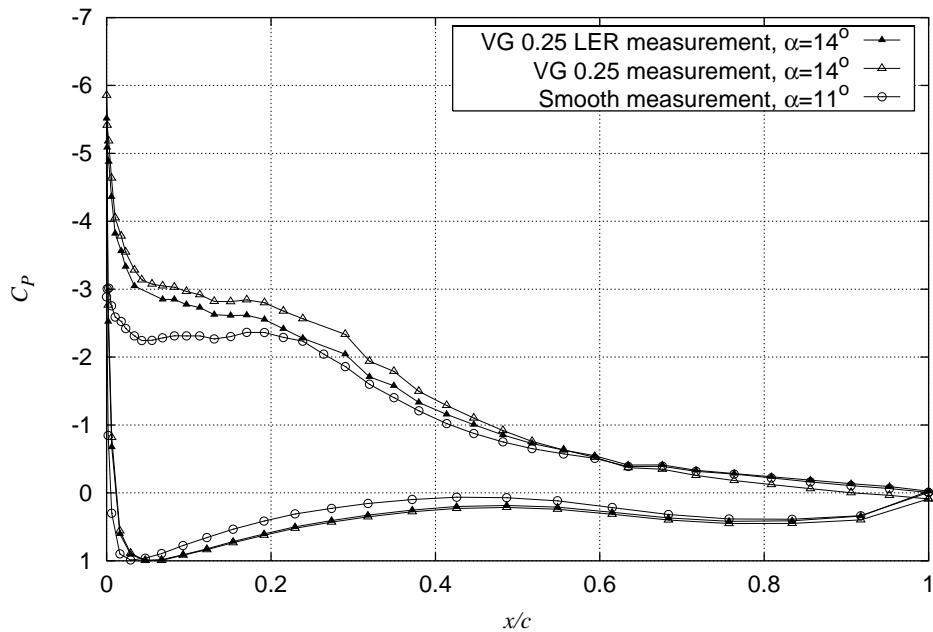
Figure 6-16 C_p at maximum C_L for Risø-A1-21 VG 25% Smooth and LER measurement compared with smooth measurements (run023,024).
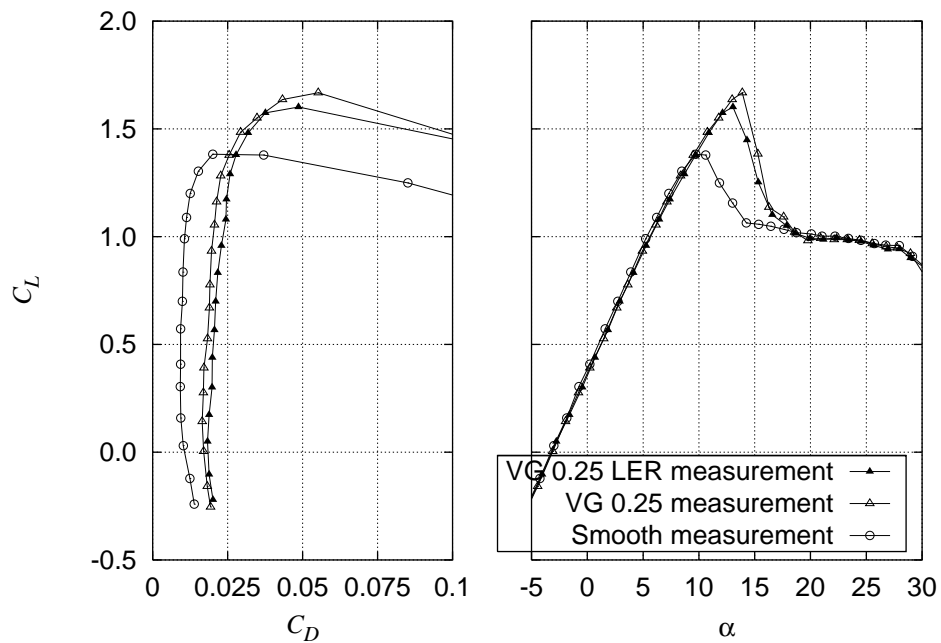
Figure 6-17 C_L-C_D for Risø-A1-21 VG 25% Smooth and LER measurement compared with smooth measurements (run023,024).

Figure 6-18 C_L, C_D and C_M for Risø-A1-21 VG 25% Smooth and LER measurement compared with smooth measurements (run023,024).

6.6 Risø-A1-21 Dynamic stall (run026)
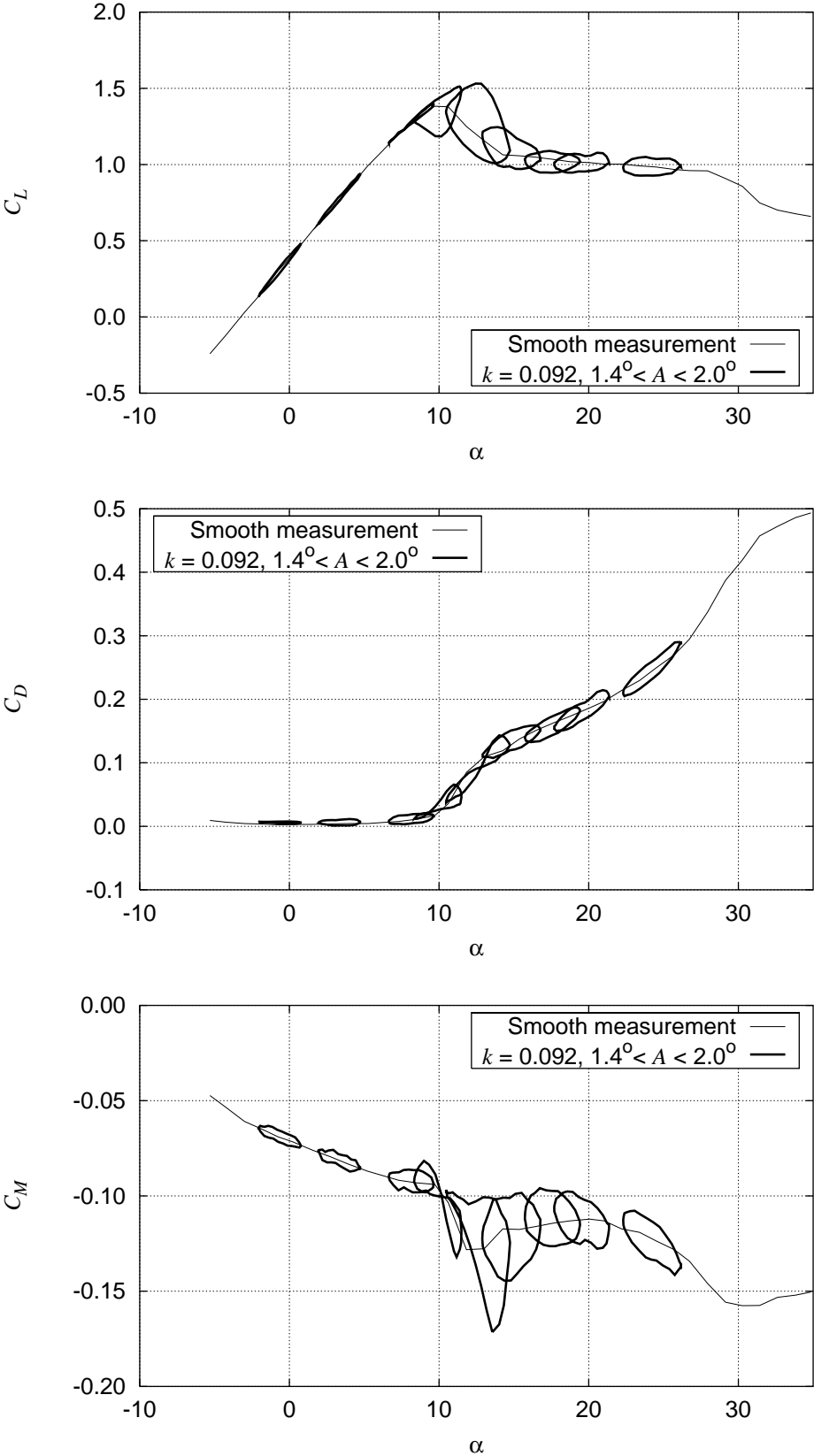
Figure 6-19 C_L, C_D and C_M hysteresis loops for Risø-A1-21 smooth measurement at k = 0.092, A between 1.4° and 2.0° (run022).
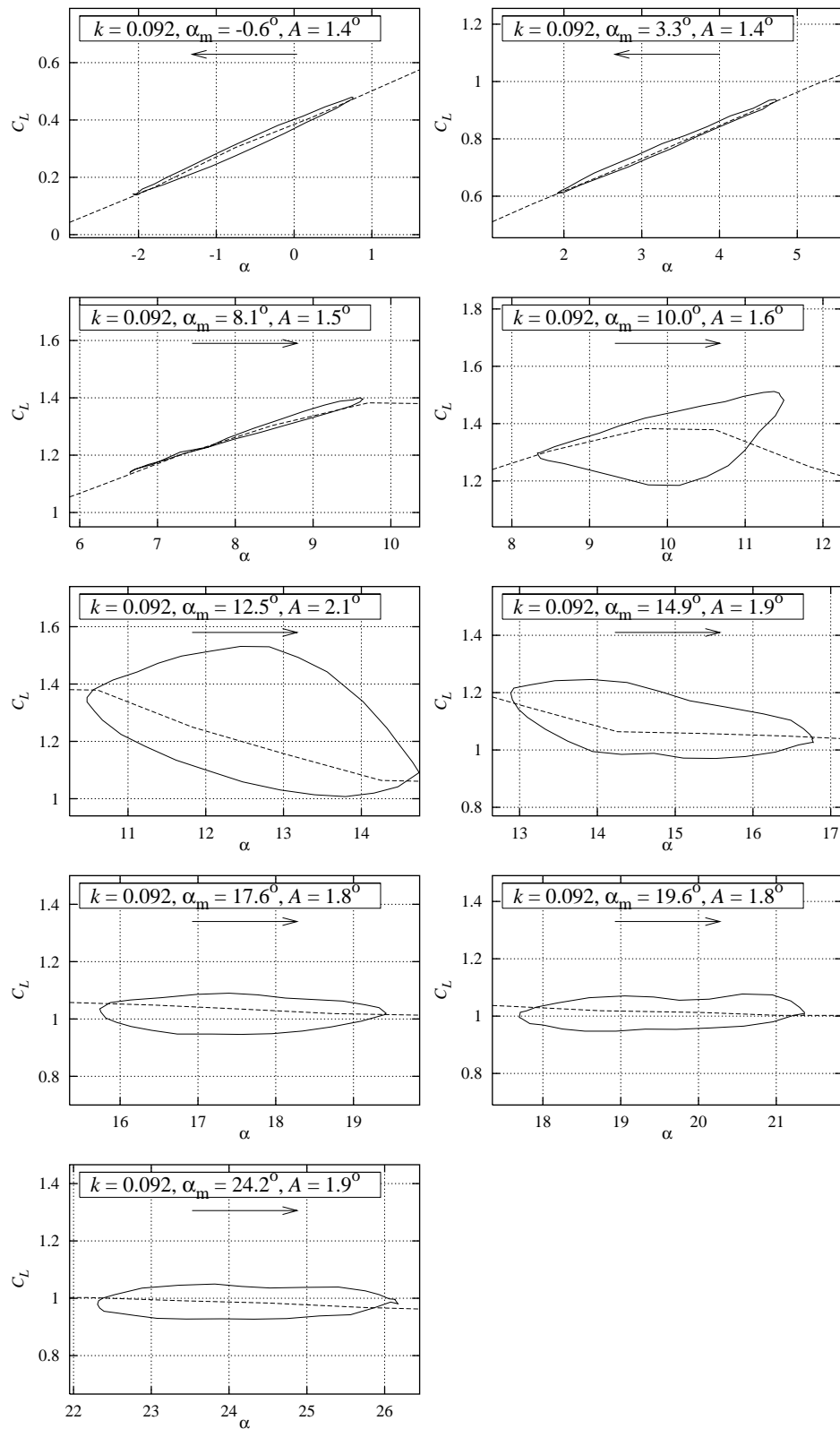
Figure 6-20 C_L hysteresis loops for Risø-A1-21 smooth measurement at k = 0.092, A between 1.4° and 2.0° (run022).
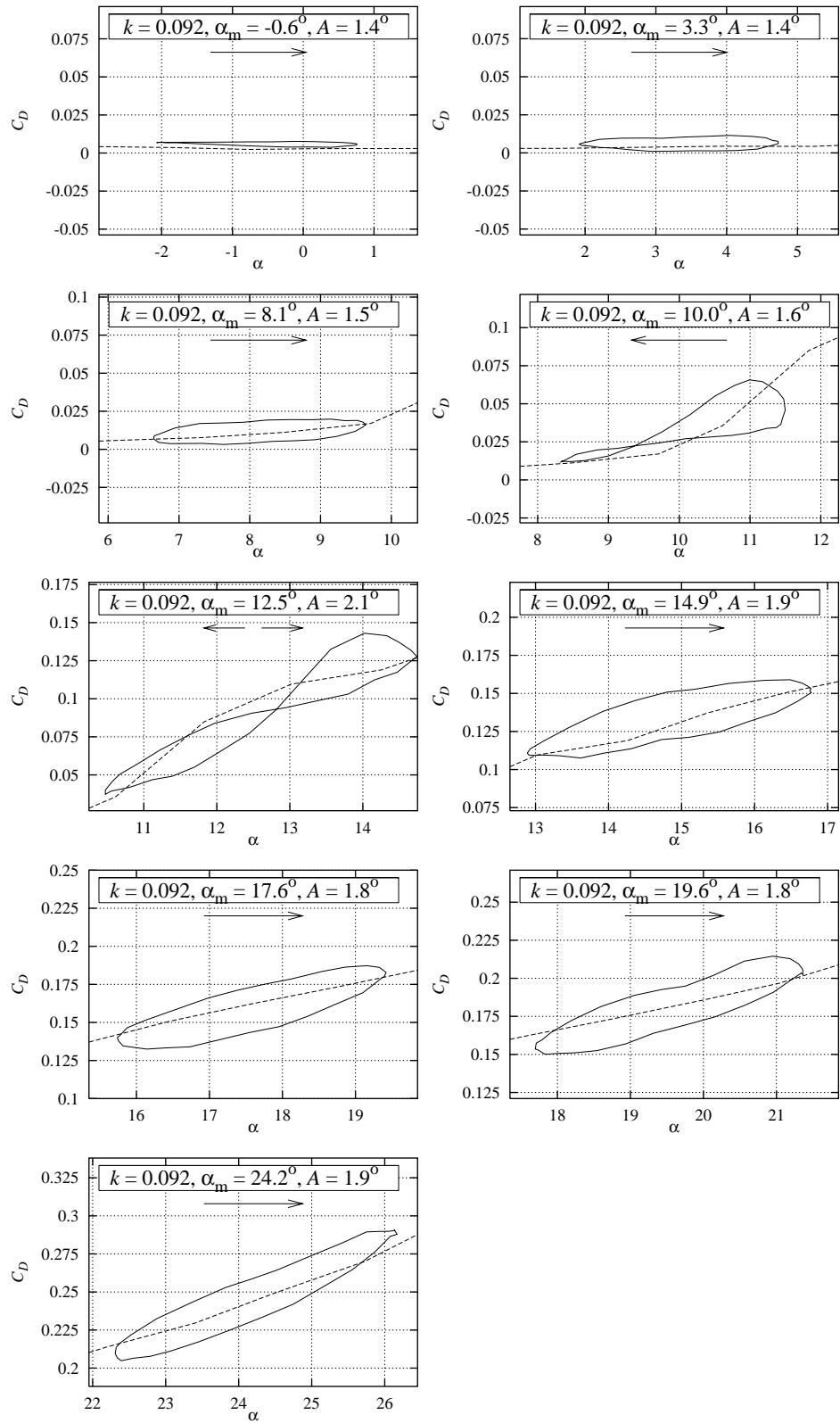
Figure 6-21 C_D hysteresis loops for Risø-A1-21 smooth measurement at $k = 0.092$, A between 1.4° and 2.0° (run022).
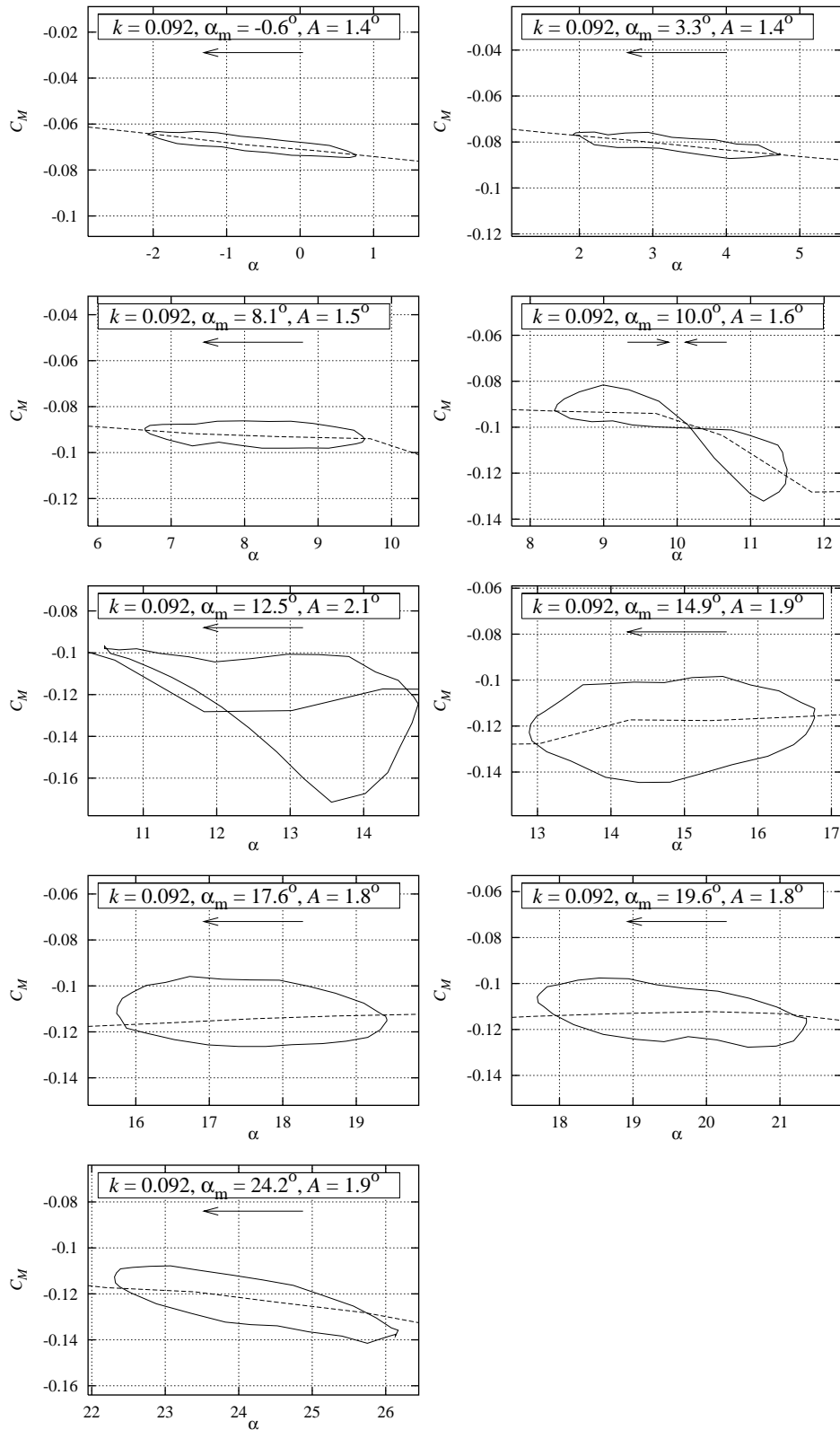
Figure 6-22 C_M hysteresis loops for Risø-A1-21 smooth measurement at k = 0.092, A between 1.4° and 2.0° (run022).

7 Results for Risø-A1-24

7.1 Risø-A1-24 Smooth flow (run032)
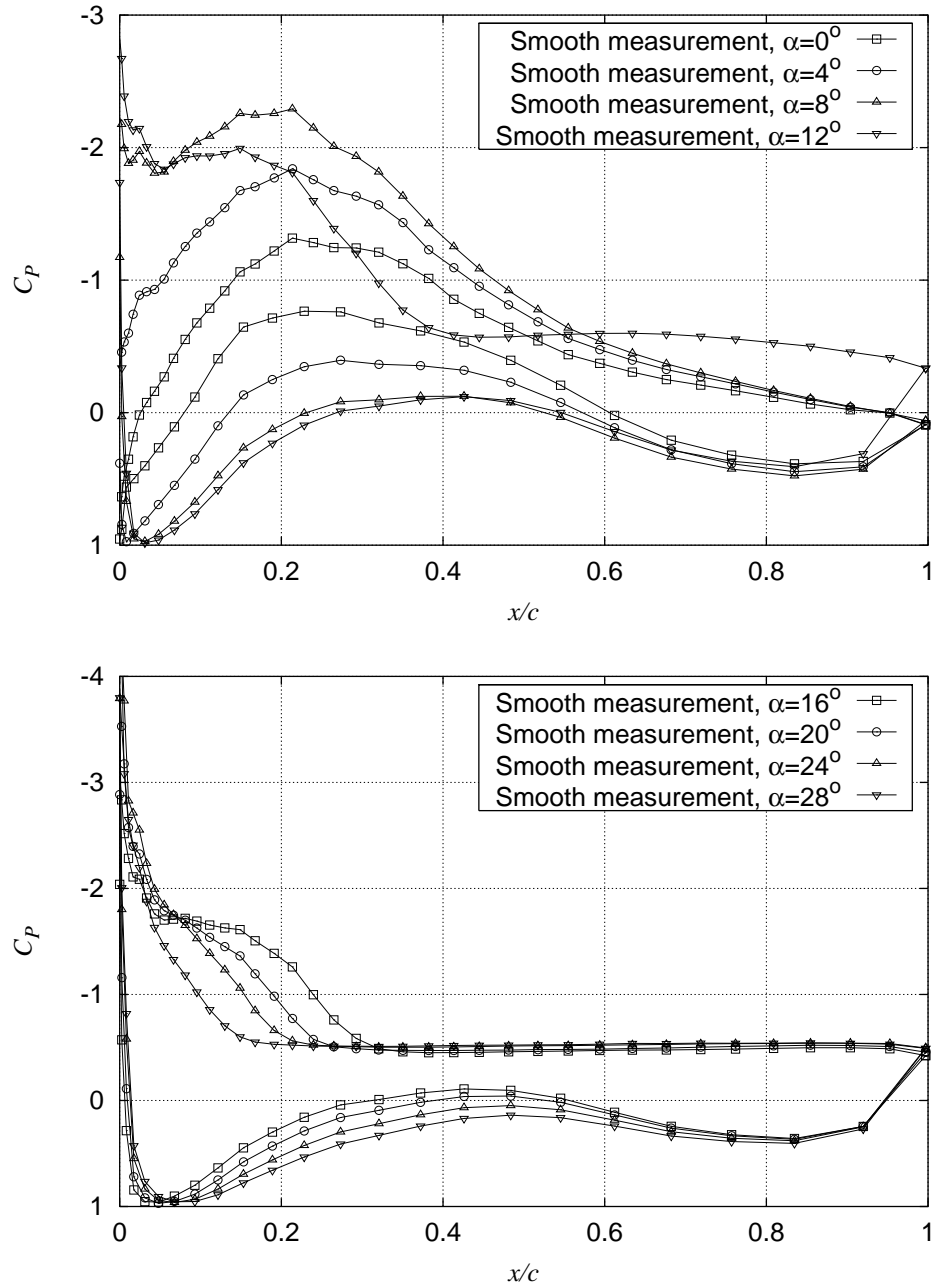
Figure 7-1 C_P at different angles of attack for Risø-A1-24 smooth measurement (run032).
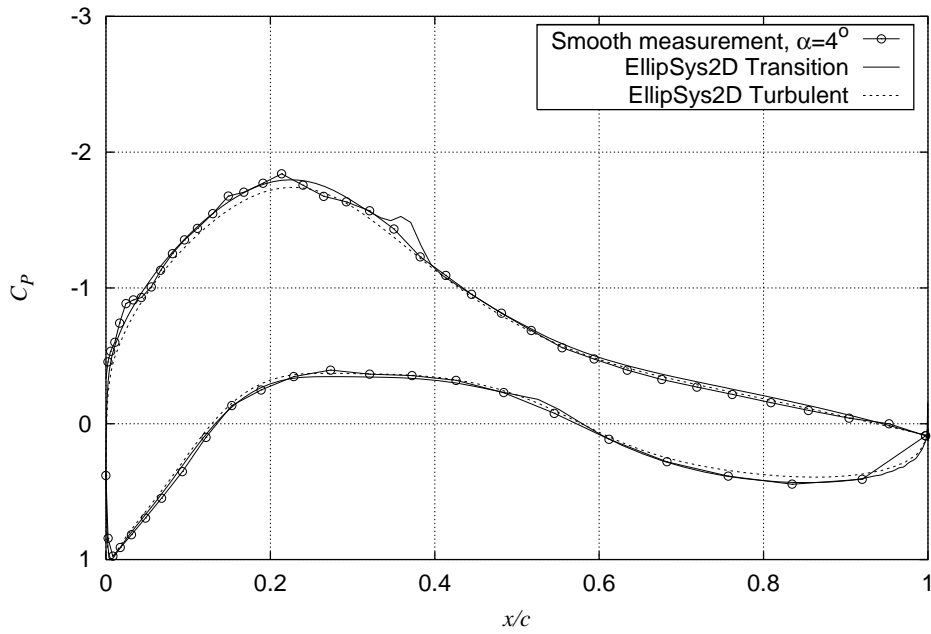
Figure 7-2 C_P at $\alpha = 4°$ for Risø-A1-24 smooth measurement compared with EllipSys2D calculations with transition modeling and turbulent flow respectively (run032).
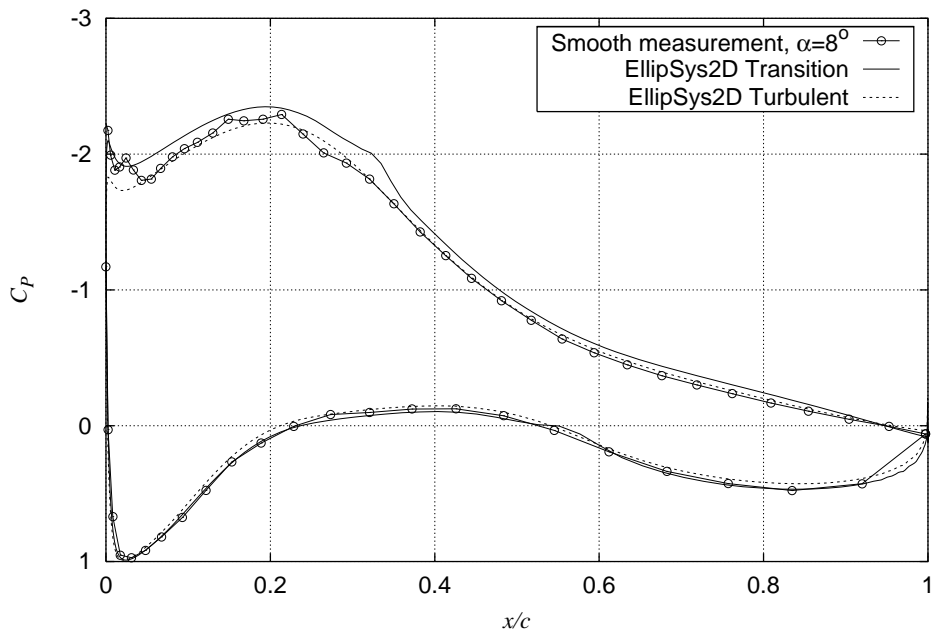
Figure 7-3 C_P at $\alpha = 8°$ for Risø-A1-24 smooth measurement compared with EllipSys2D calculations with transition modeling and turbulent flow respectively (run032).
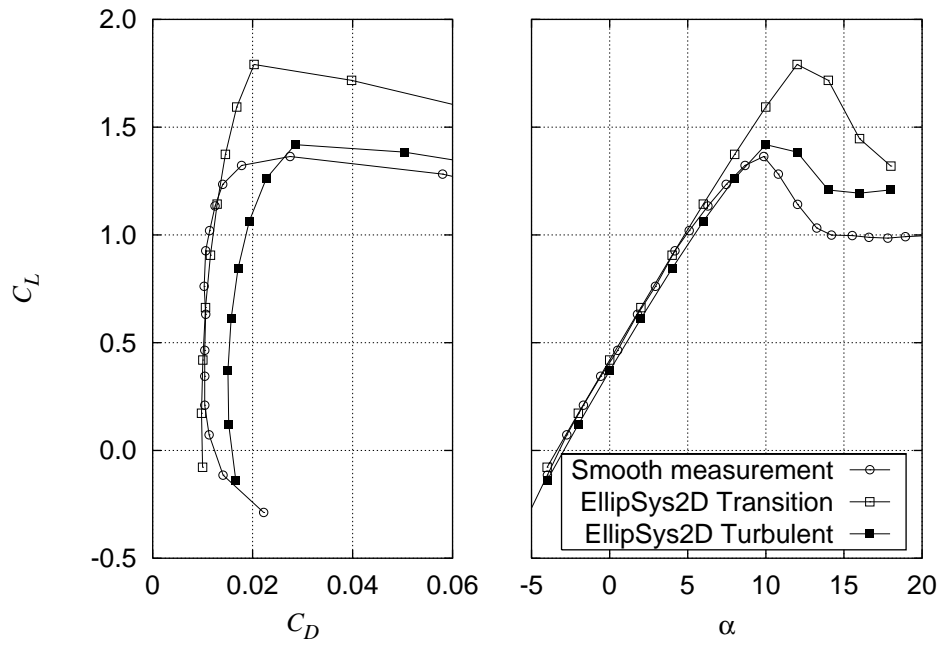
Figure 7-4 C_L-C_D for Risø-A1-24 smooth measurement compared with EllipSys2D calculations with transition modeling and turbulent flow respectively (run032).
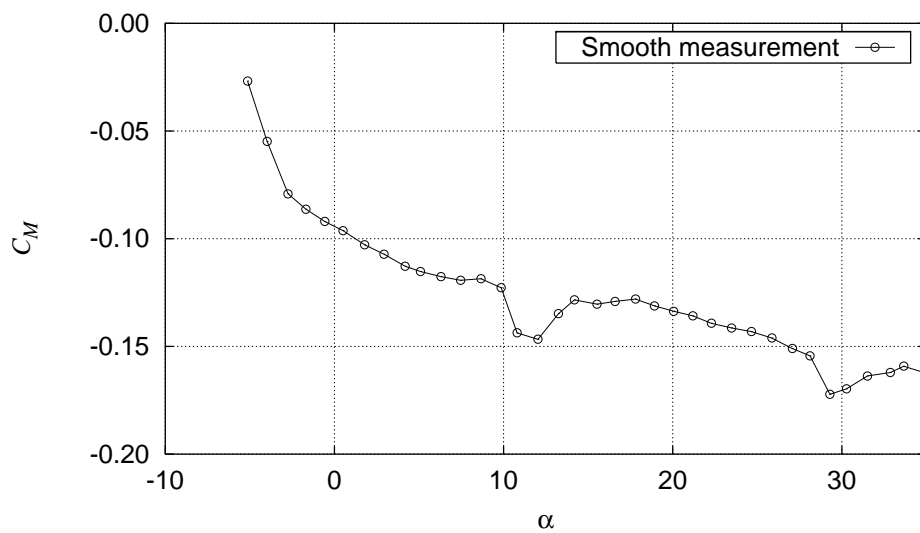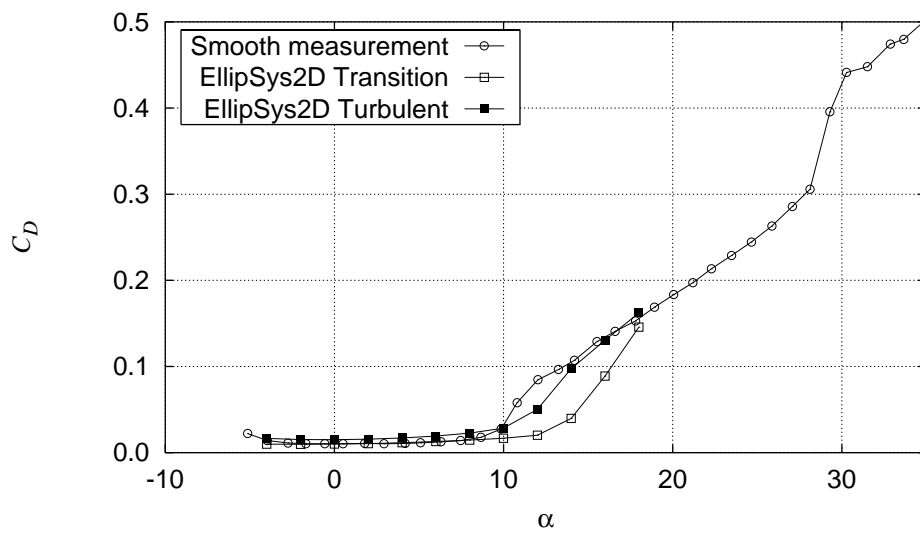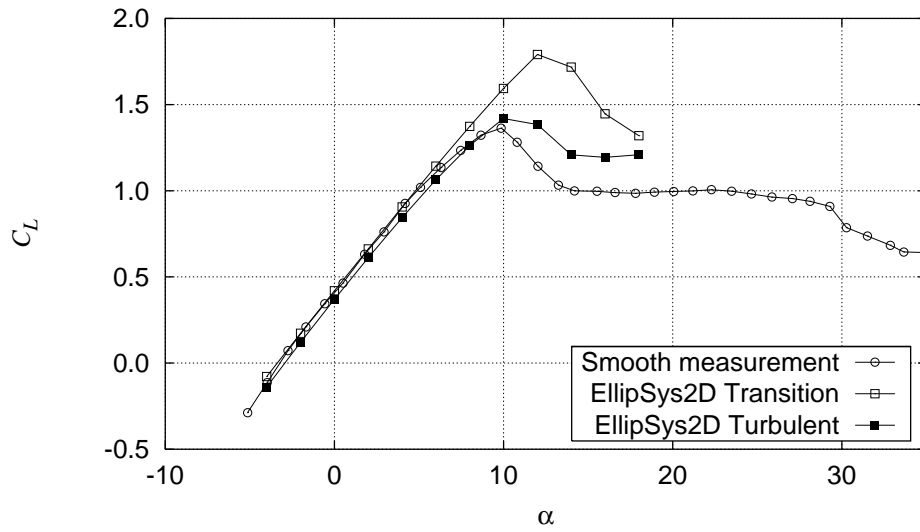
Figure 7-5 C_L, C_D and C_M for Risø-A1-24 smooth measurement compared with EllipSys2D calculations with transition modeling and turbulent flow respectively (run032).

7.2 Risø-A1-24 LER (run029)
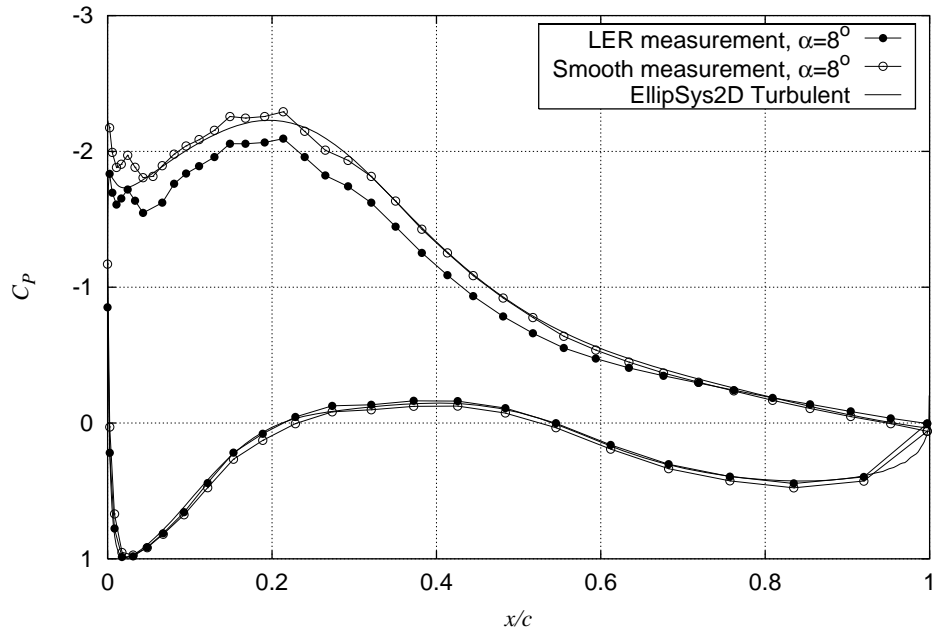
Figure 7-6 C_P at $\alpha = 8°$ for Risø-A1-24 LER measurement compared with smooth measurement and EllipSys2D calculations with turbulent flow (run029).
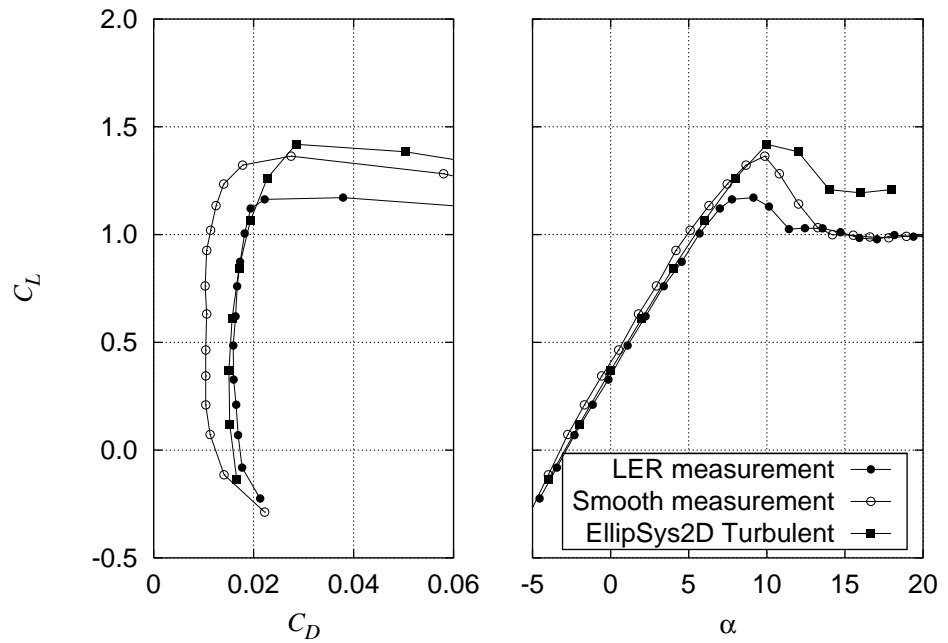
Figure 7-7 C_L-C_D for Risø-A1-24 LER measurement compared with smooth measurement and EllipSys2D calculations with turbulent flow (run029).
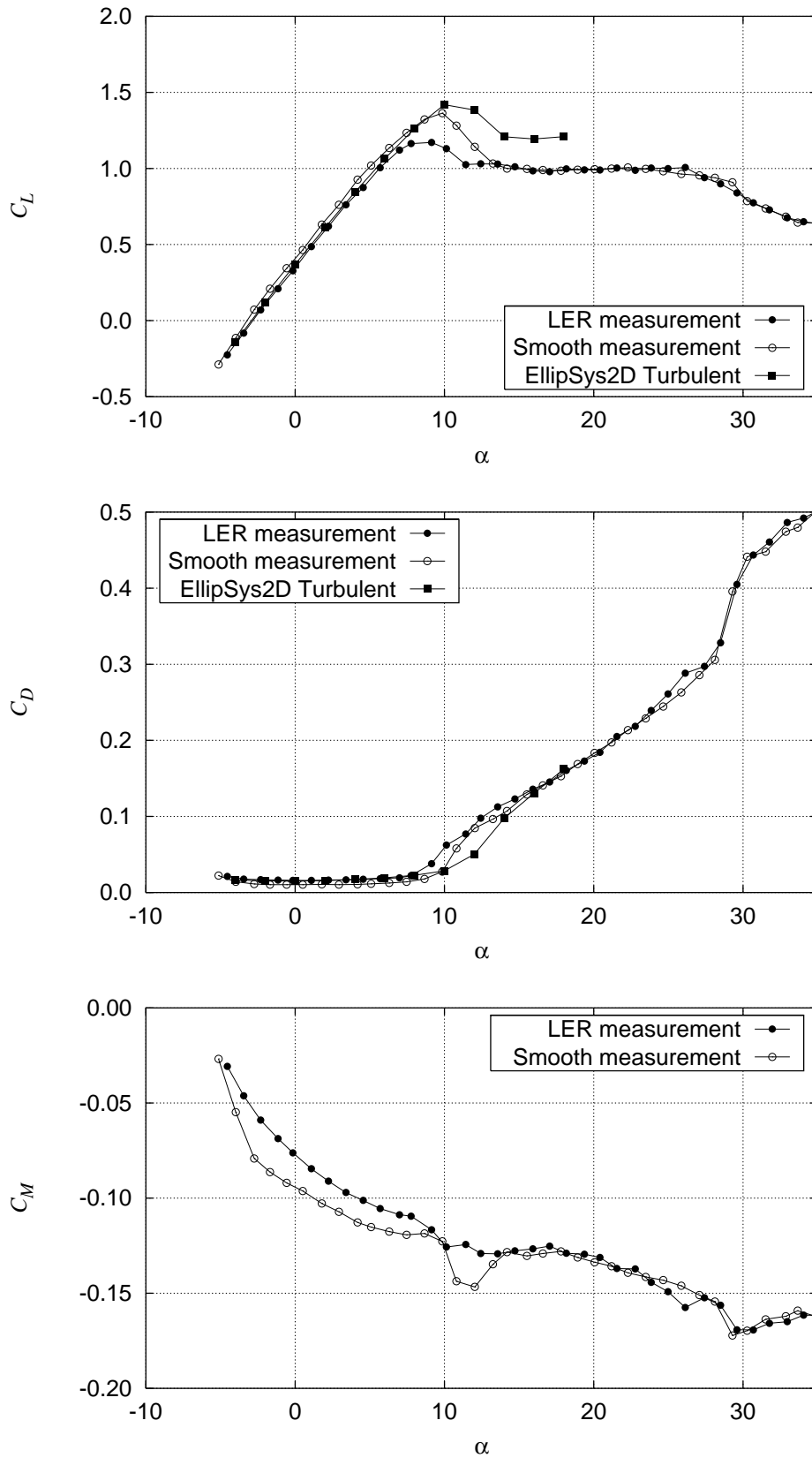
Figure 7-8 C_L, C_D and C_M for Risø-A1-24 LER measurement compared with smooth measurement and EllipSys2D calculations with turbulent flow (run029).

7.3 Risø-A1-24 VGs (run034, 027, 031, 081)
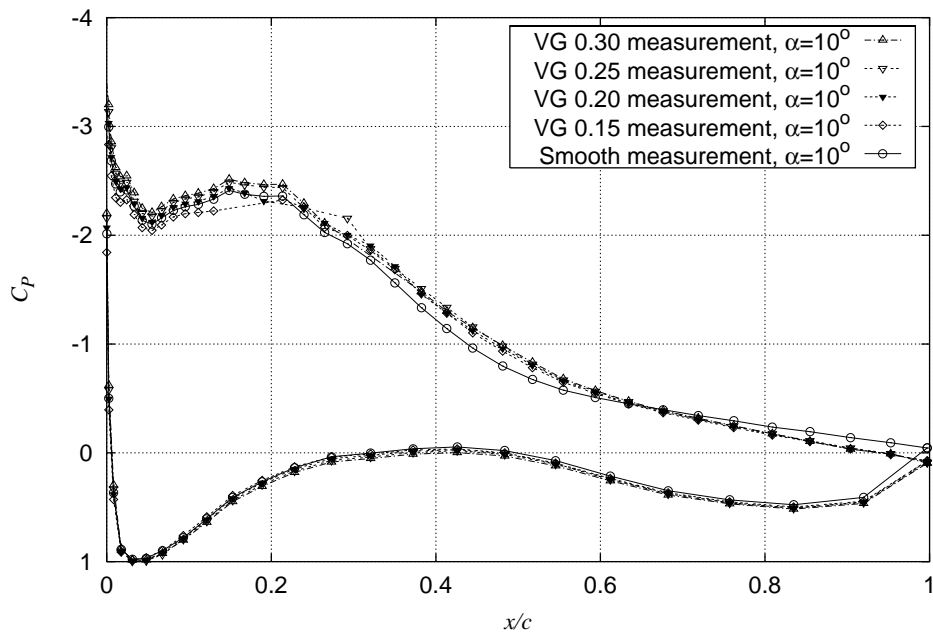
Figure 7-9 C_P at $\alpha = 10^o$ for Risø-A1-24 VG measurements compared with smooth measurement (run081,031,027,034).
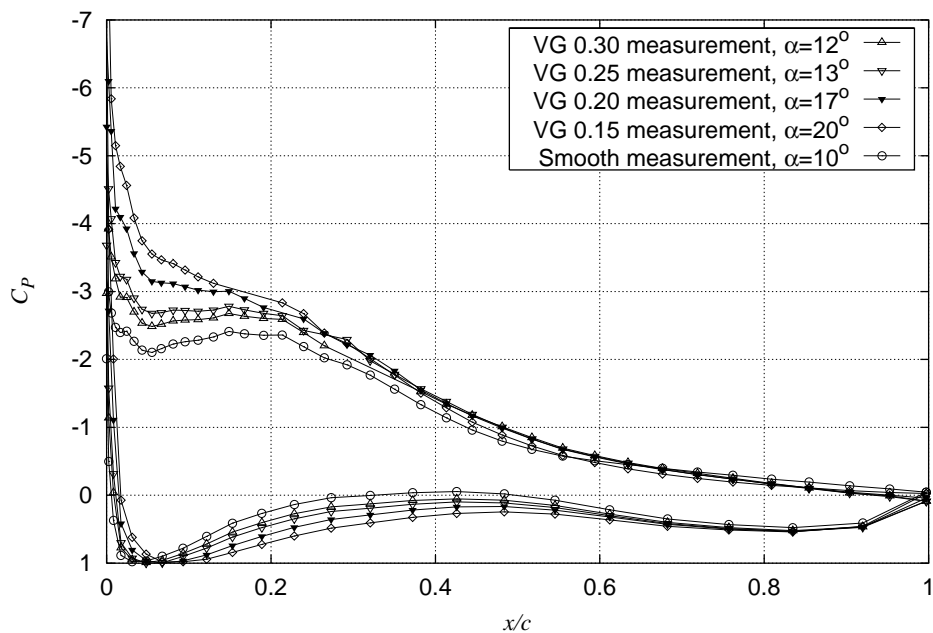
Figure 7-10 C_p at maximum C_L for Risø-A1-24 VG measurements compared with smooth measurement (run081,031,027,034).
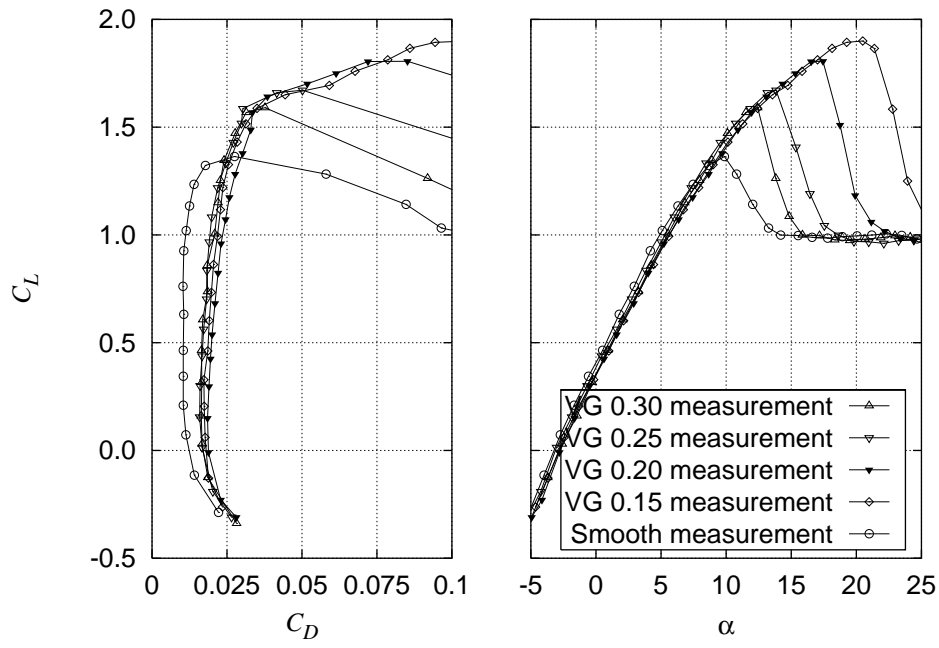
Figure 7-11 C_L-C_D for Risø-A1-24 VG measurements compared with smooth measurement (run081,031,027,034).
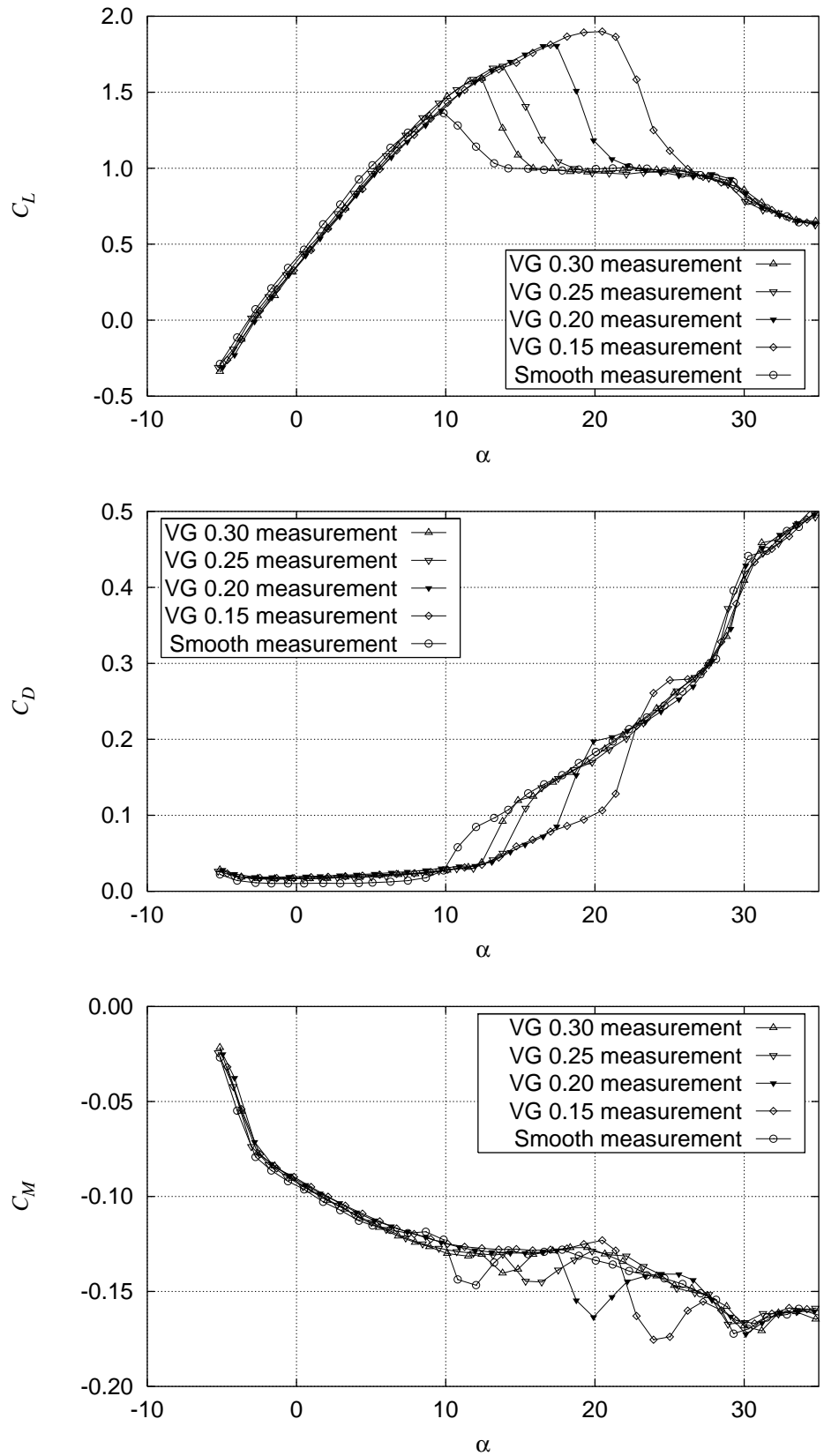
Figure 7-12 C_L, C_D and C_M for Risø-A1-24 VG measurements compared with smooth measurement (run081,031,027,034).

7.4 Risø-A1-24 GFs (run039,run040)
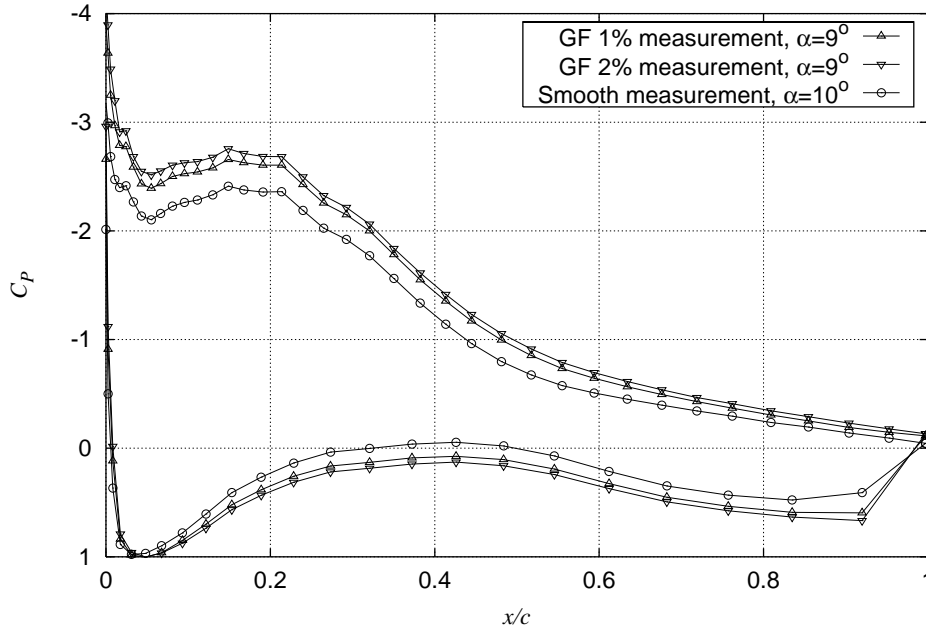
Figure 7-13 C_p at maximum C_L for Risø-A1-24 GF measurements compared with smooth measurement (run040,039).
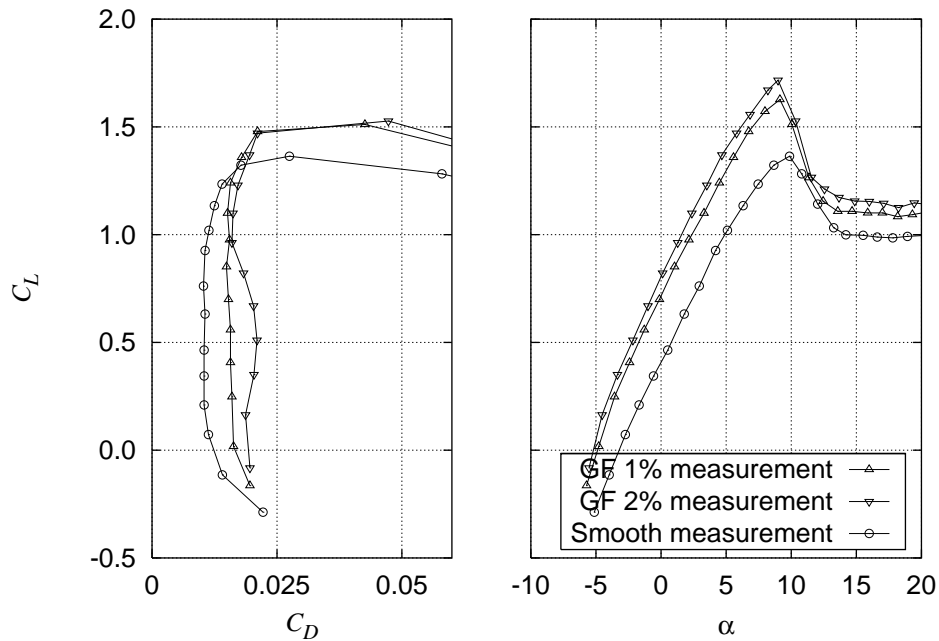
Figure 7-14 C_L-C_D for Risø-A1-24 GF measurements compared with smooth measurement (run040,039).
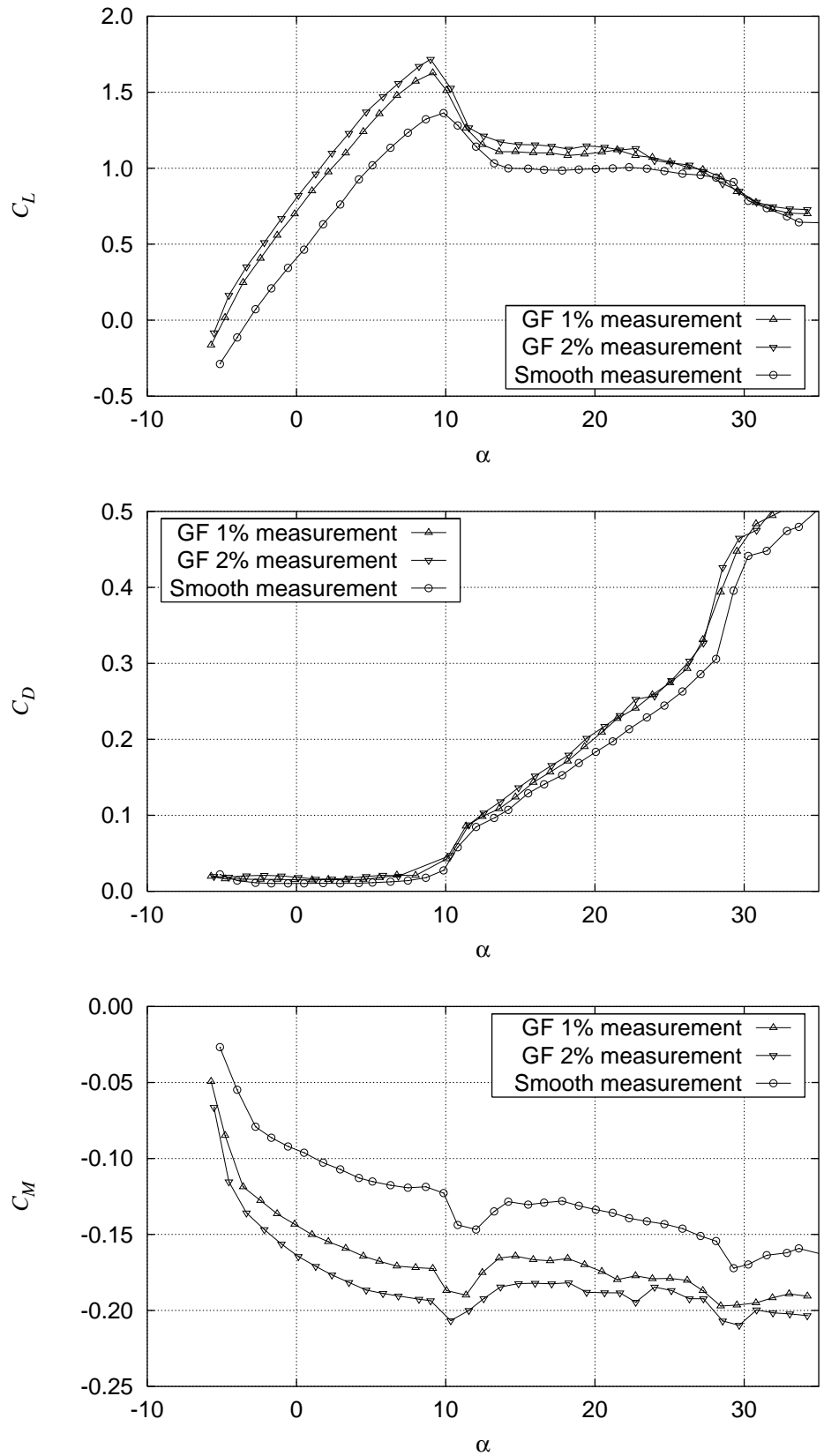
Figure 7-15 C_L, C_D and C_M for Risø-A1-24 GF measurements compared with smooth measurement (run040,039).

7.5 Risø-A1-24 VGs at 0.1 (run064, 065)
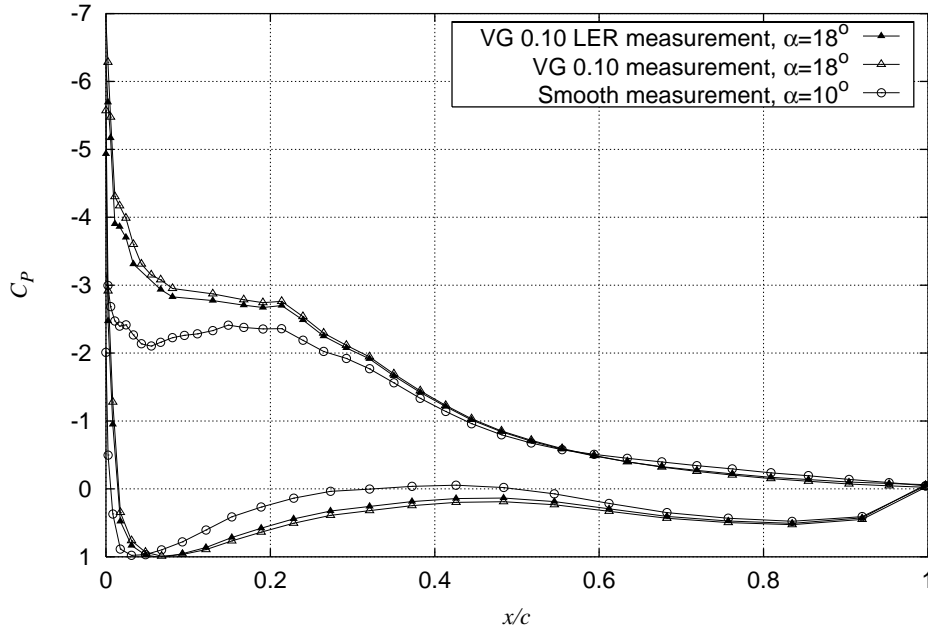
Figure 7-16 C_p at maximum C_L for Risø-A1-24 VG 10% Smooth and LER measurement compared with smooth measurements (run064,065).
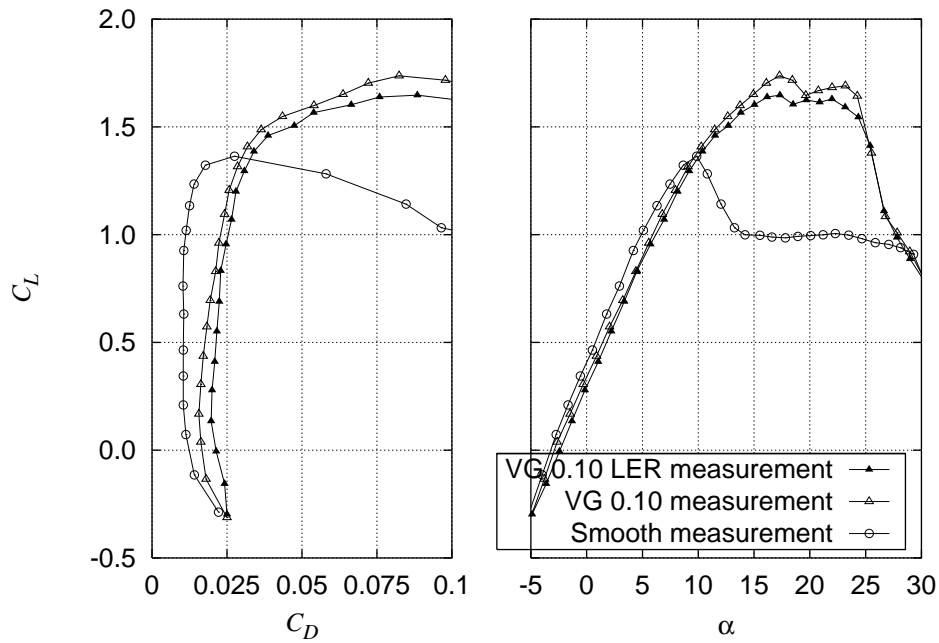
Figure 7-17 C_L-C_D for Risø-A1-24 VG 10% Smooth and LER measurement compared with smooth measurements (run064,065).
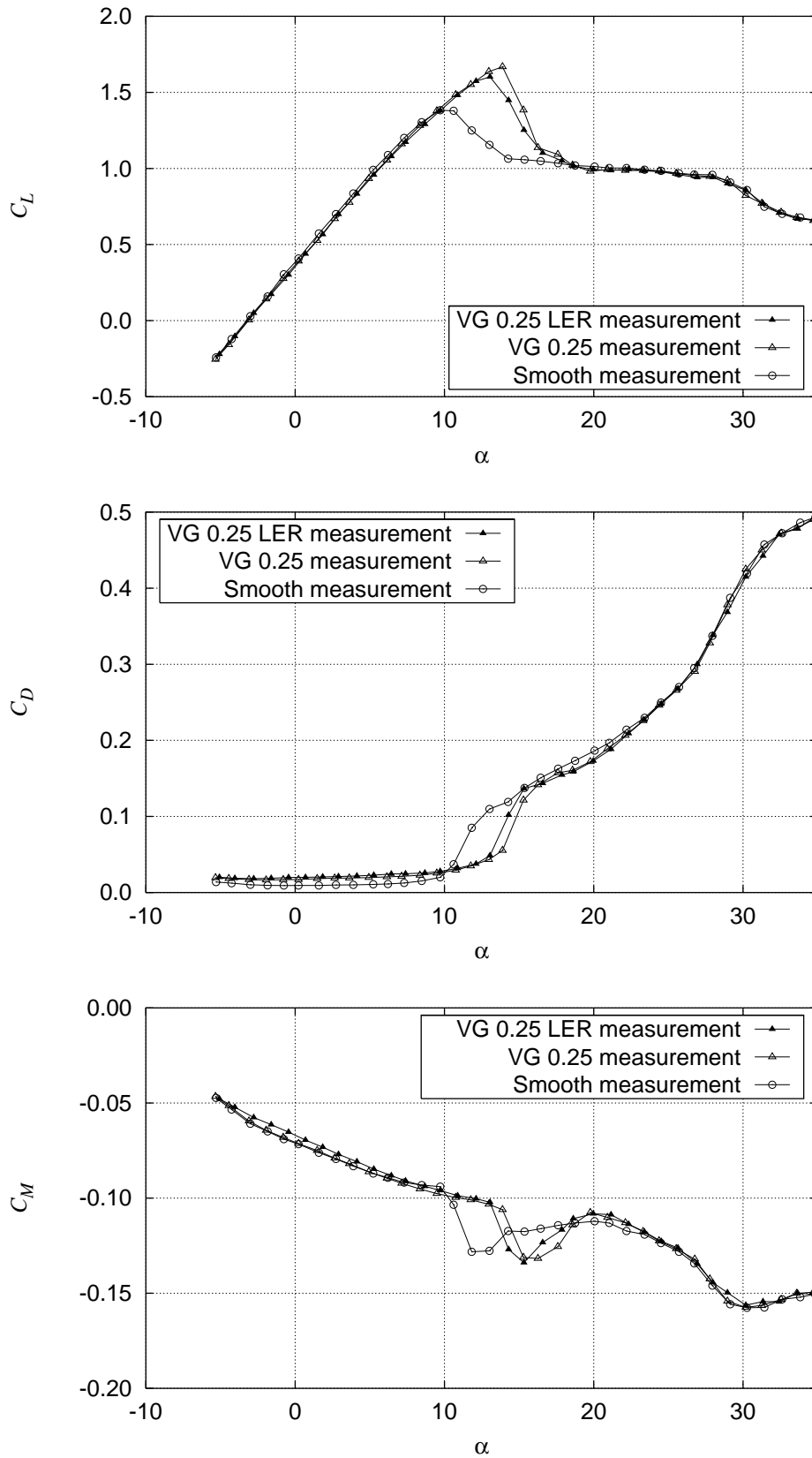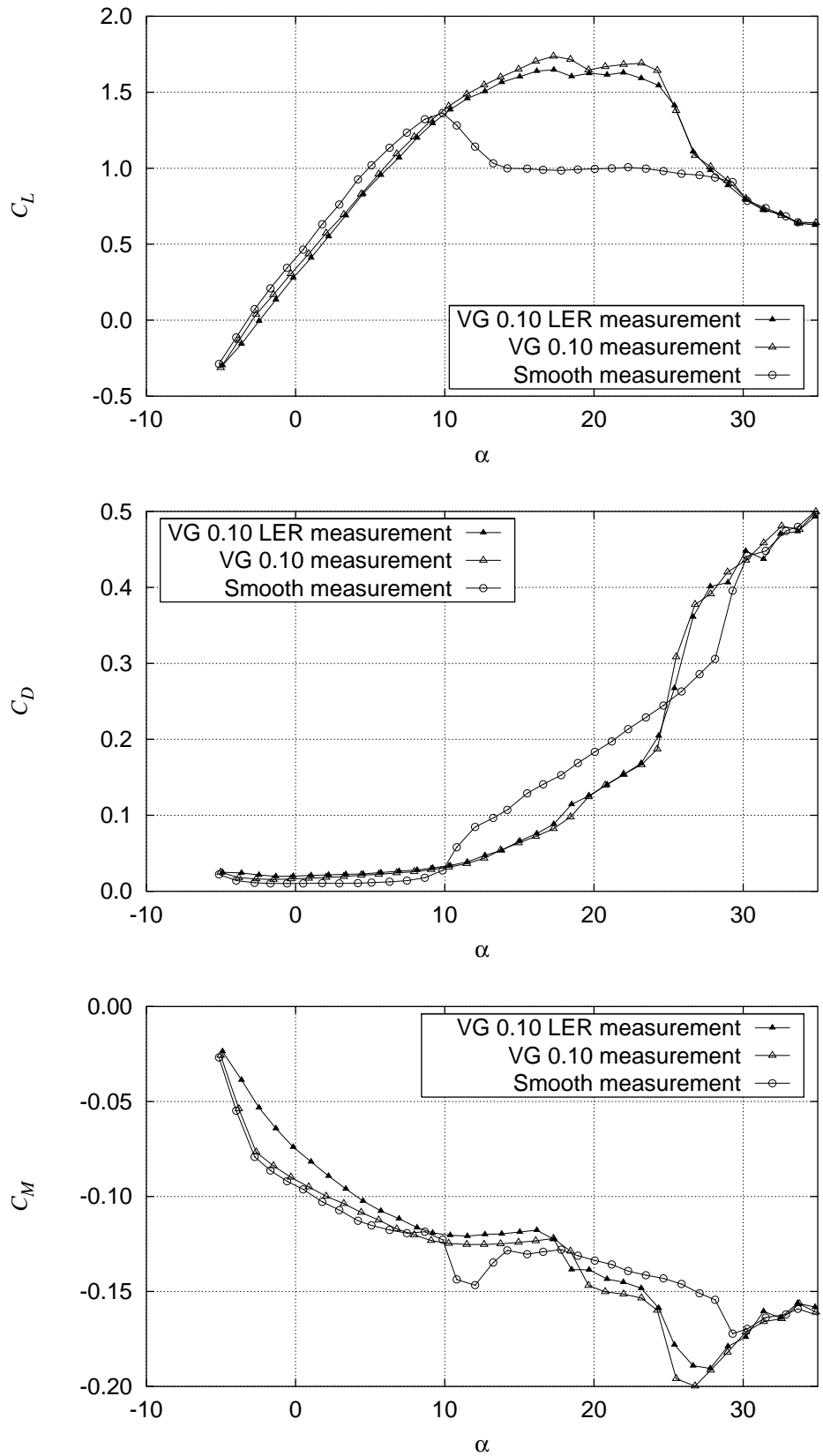
Figure 7-18 C_L, C_D and C_M for Risø-A1-24 VG 10% Smooth and LER measurement compared with smooth measurements (run064,065).

7.6 Risø-A1-24 VGs at 0.15 (run034,035)
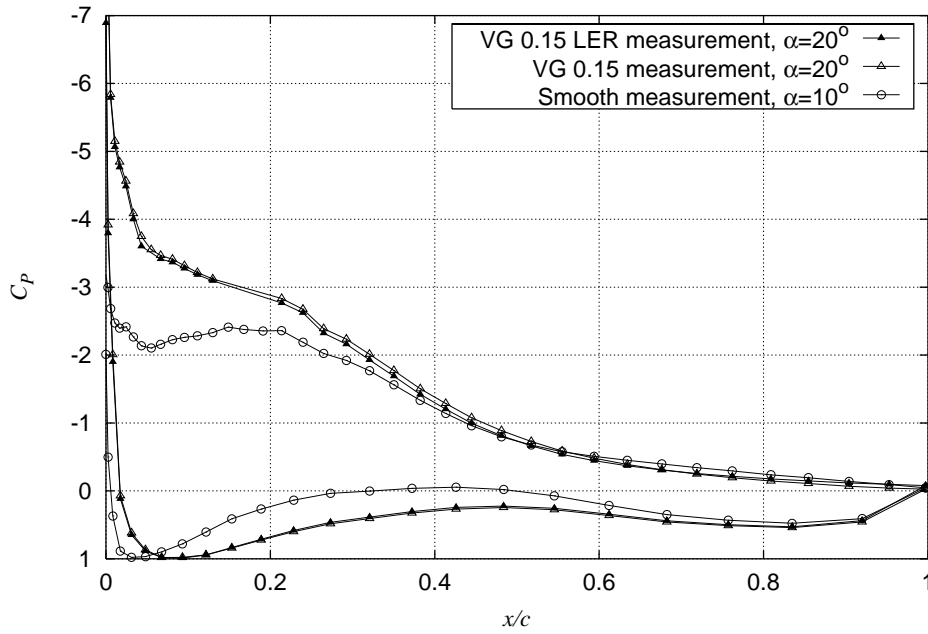
Figure 7-19 C_p at maximum C_L for Risø-A1-24 VG 15% Smooth and LER measurement compared with smooth measurements (run034,035).
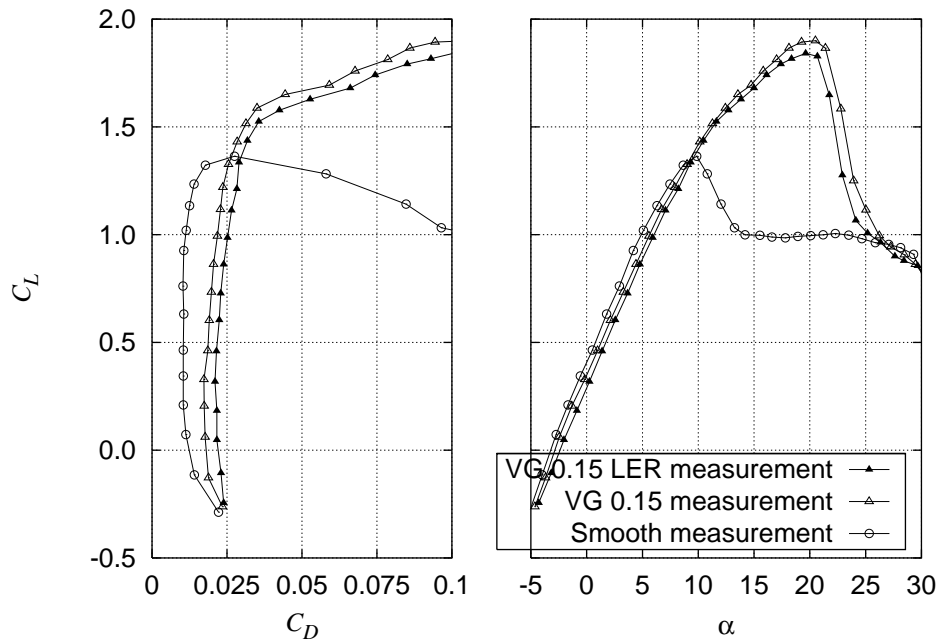
Figure 7-20 C_L-C_D for Risø-A1-24 VG 15% Smooth and LER measurement compared with smooth measurements (run034,035).
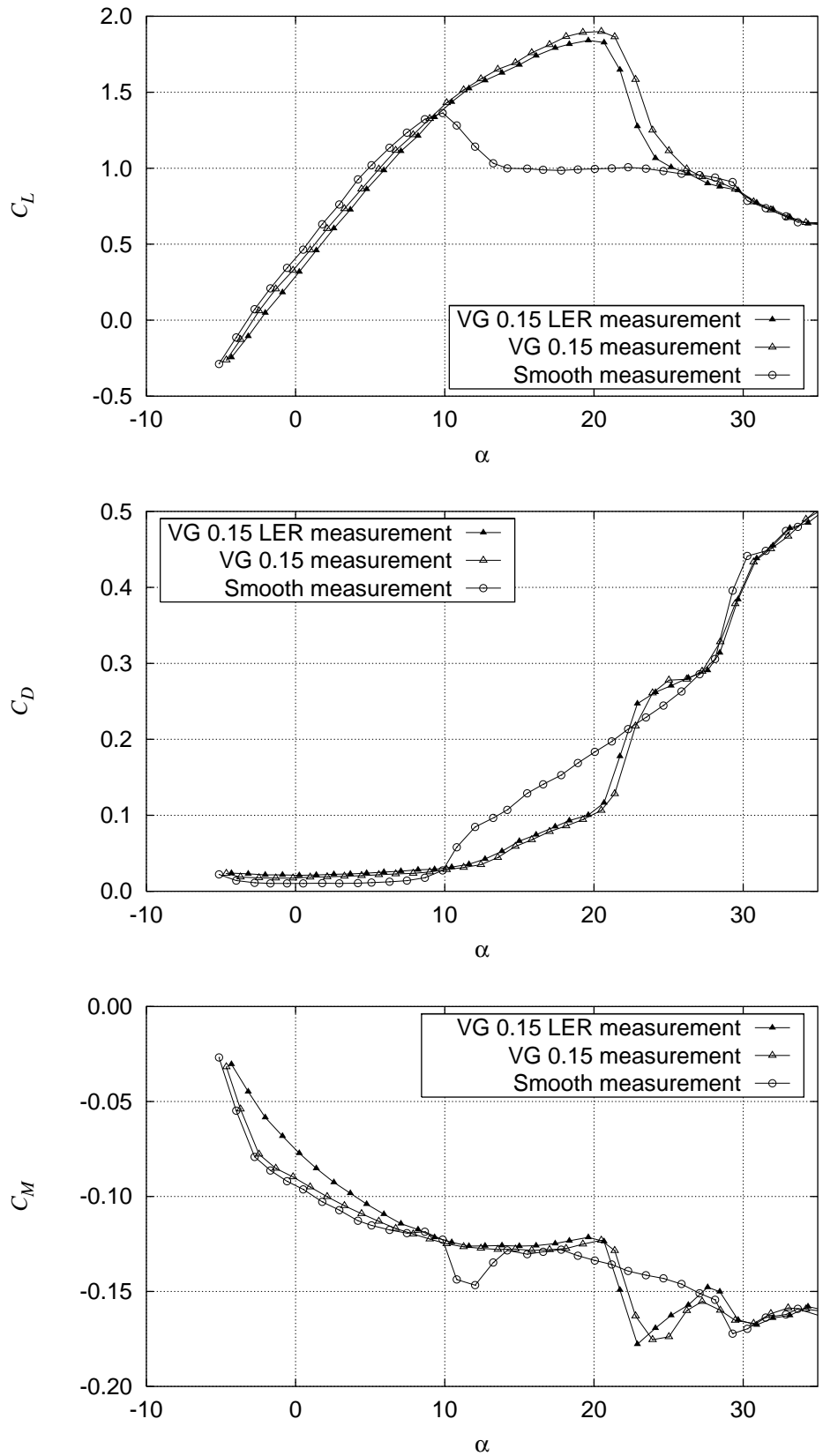
Figure 7-21 C_L, C_D and C_M for Risø-A1-24 VG 15% Smooth and LER measurement compared with smooth measurements (run034,035).

7.7 Risø-A1-24 VGs at 0.2 (run027,028)
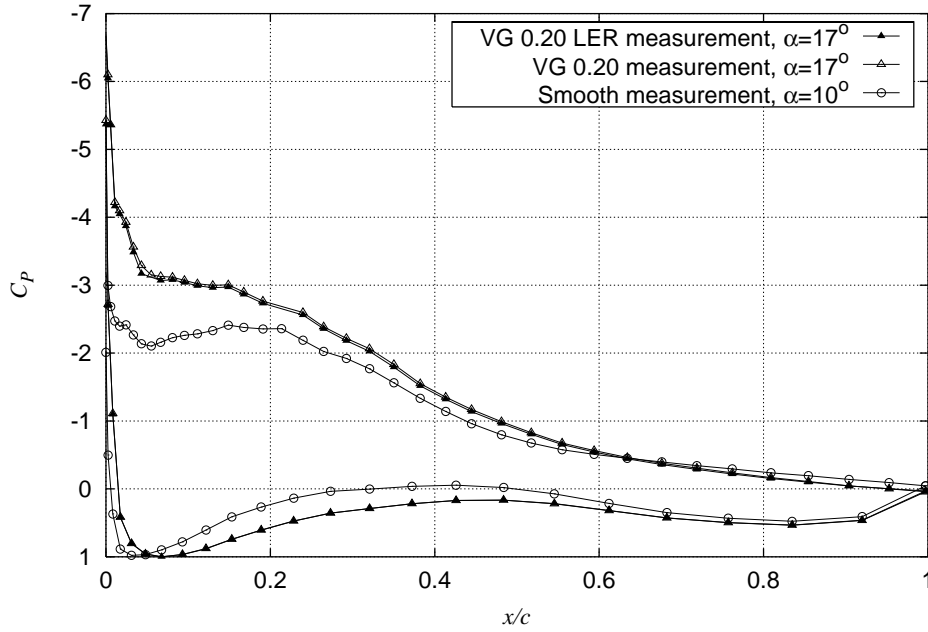
Figure 7-22 C_p at maximum C_L for Risø-A1-24 VG 20% Smooth and LER measurement compared with smooth measurements (run027,028).
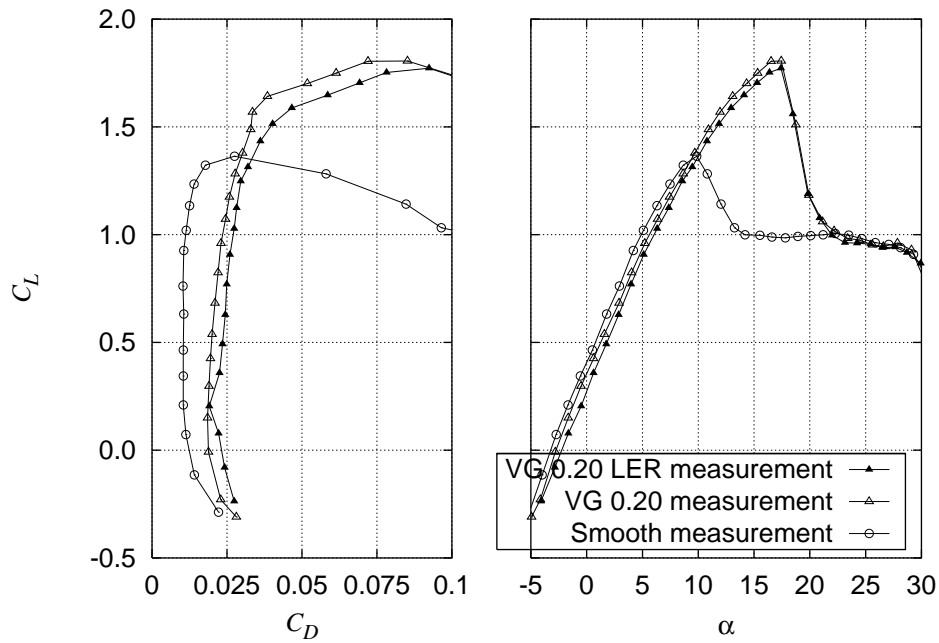
Figure 7-23 C_L-C_D for Risø-A1-24 VG 20% Smooth and LER measurement compared with smooth measurements (run027,028).
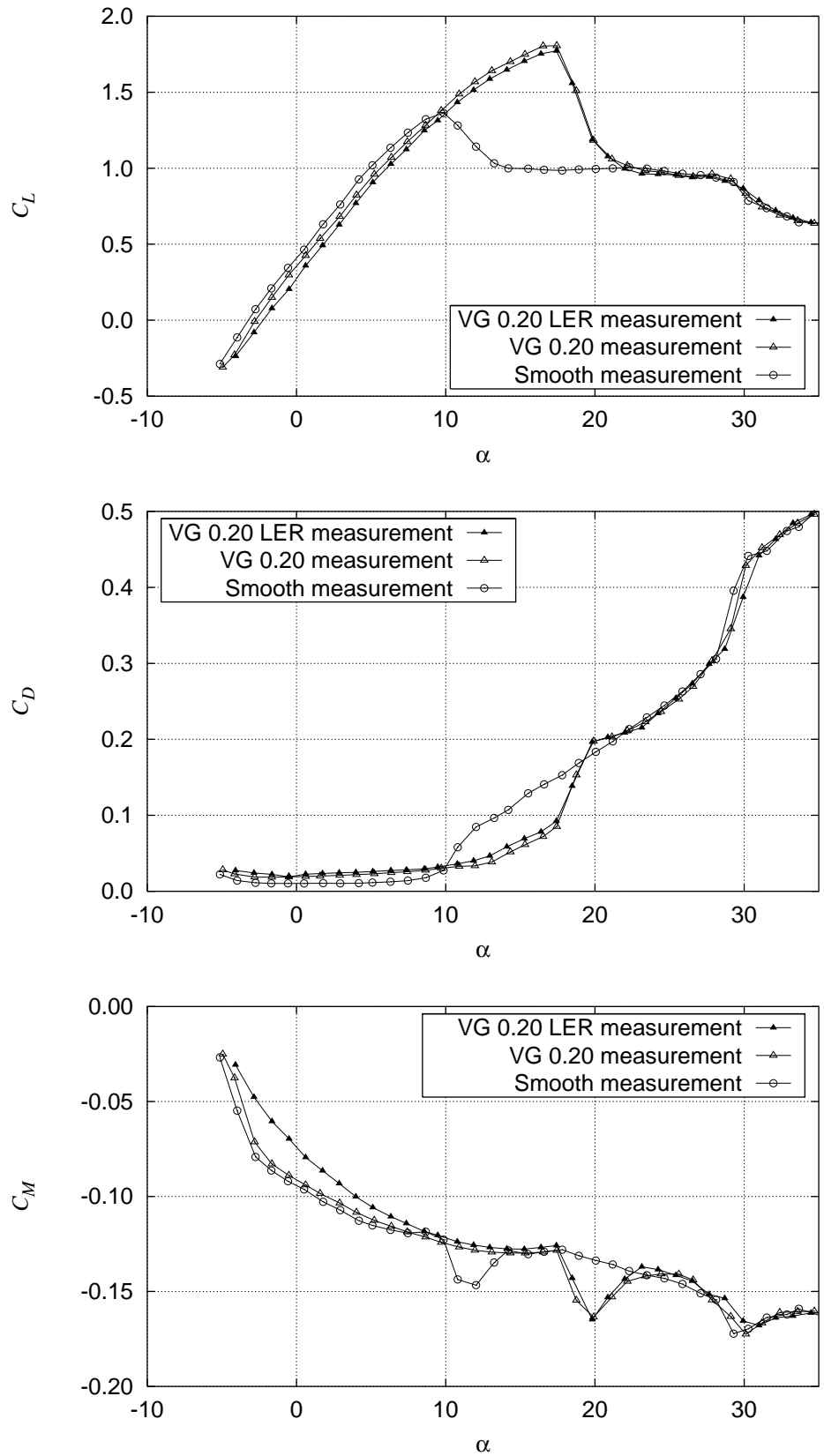
Figure 7-24 C_L, C_D and C_M for Risø-A1-24 VG 20% Smooth and LER measurement compared with smooth measurements (run027,028).

7.8 Risø-A1-24 VGs at 0.25 (run030,031)
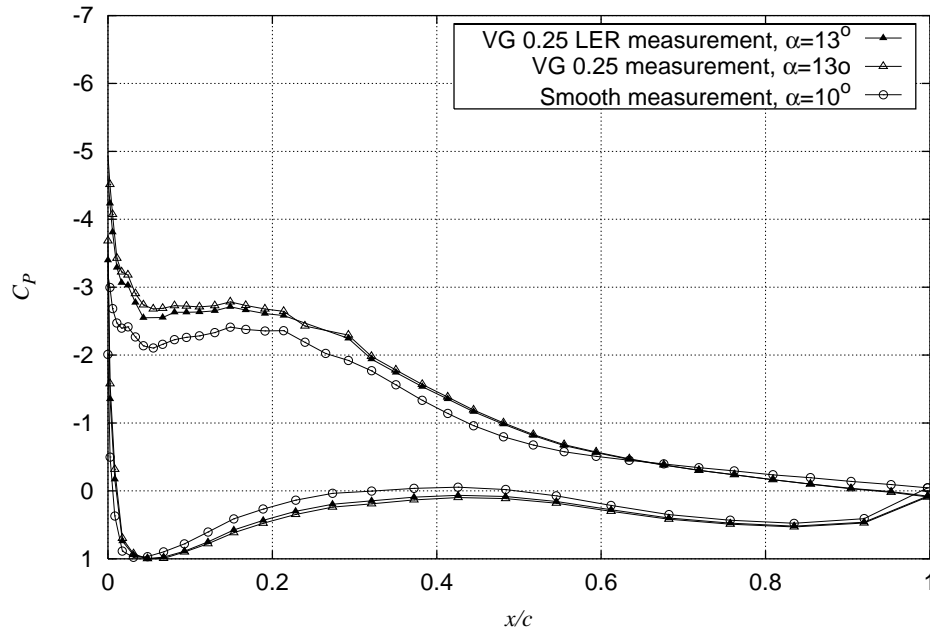
Figure 7-25 C_p at maximum C_L for Risø-A1-24 VG 25% Smooth and LER measurement compared with smooth measurements (run030,031).
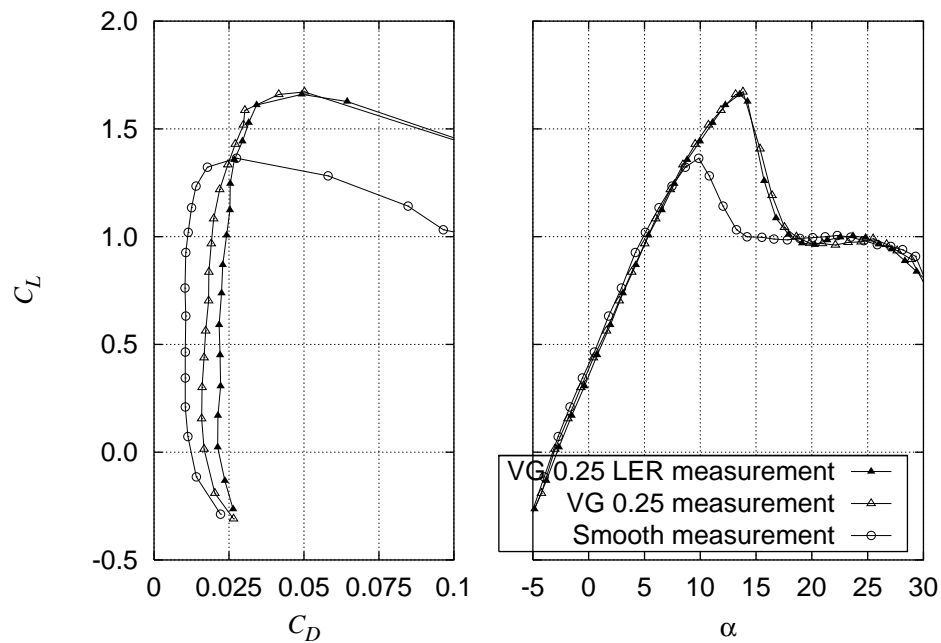
Figure 7-26 C_L-C_D for Risø-A1-24 VG 25% Smooth and LER measurement compared with smooth measurements (run030,031).
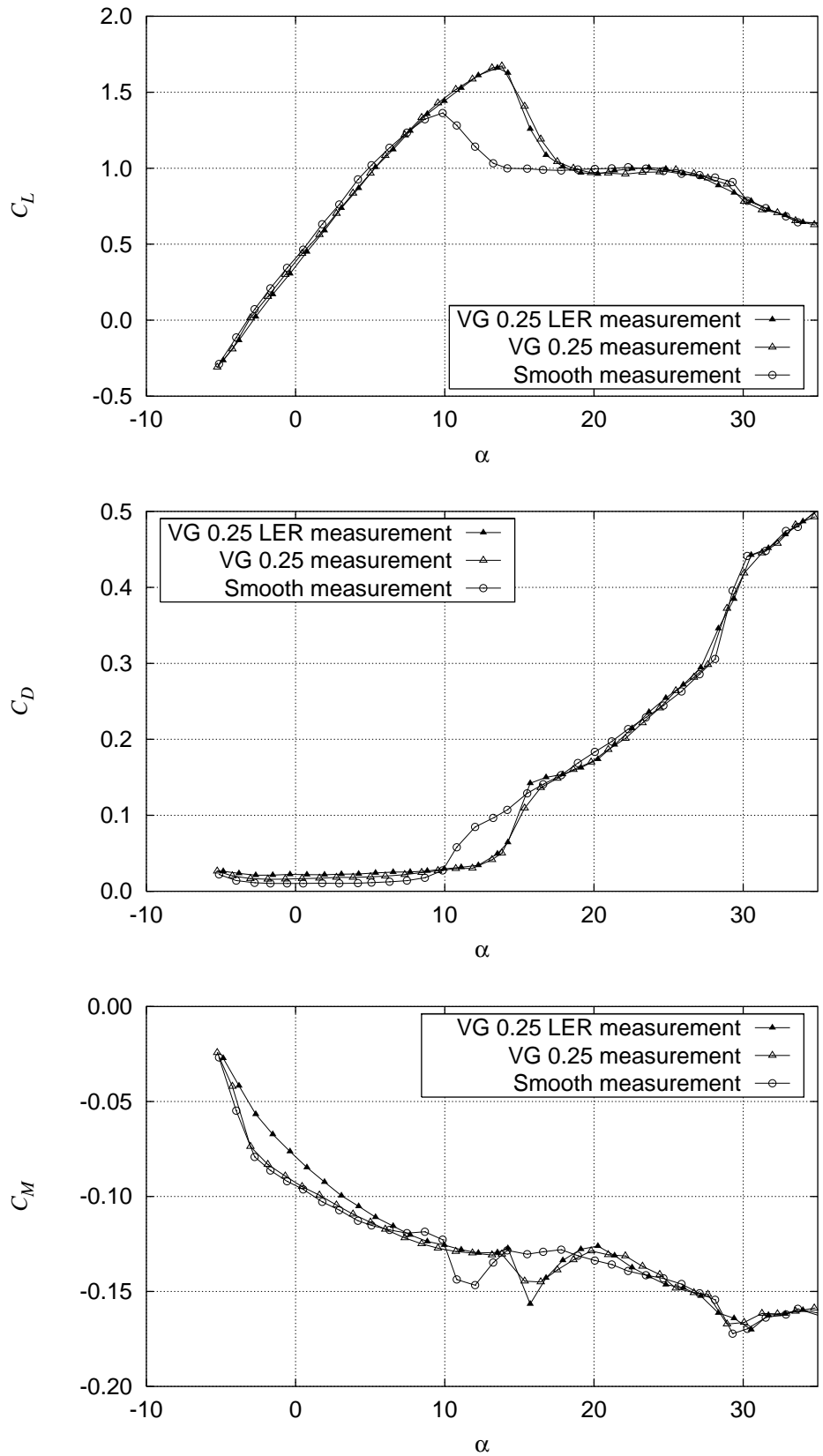
Figure 7-27 C_L, C_D and C_M for Risø-A1-24 VG 25% Smooth and LER measurement compared with smooth measurements (run030,031).

7.9 Risø-A1-24 VGs at 0.30 (run081)
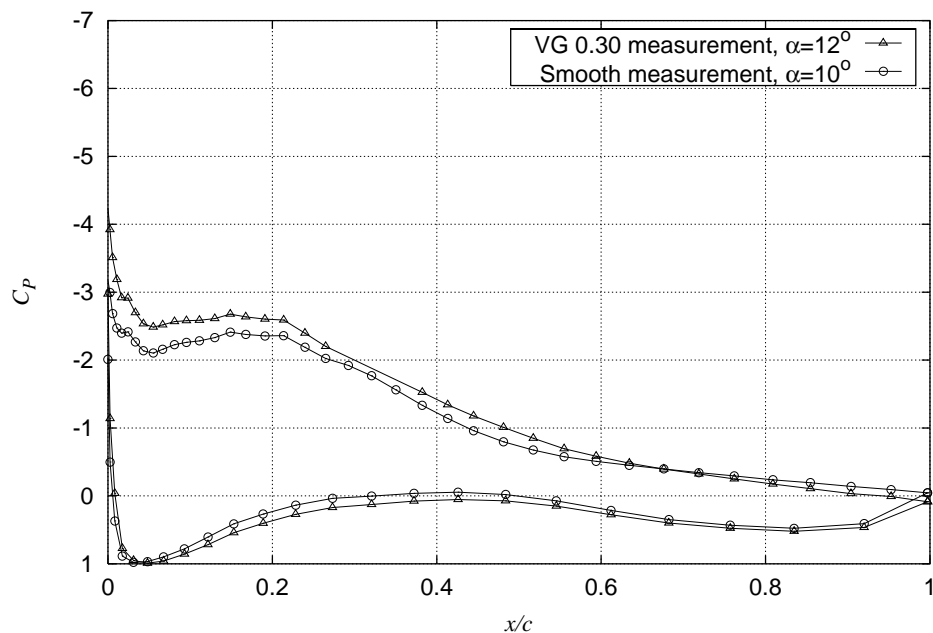
Figure 7-28 C_p at maximum C_L for Risø-A1-24 VG 30% measurement compared with smooth measurements (run081).
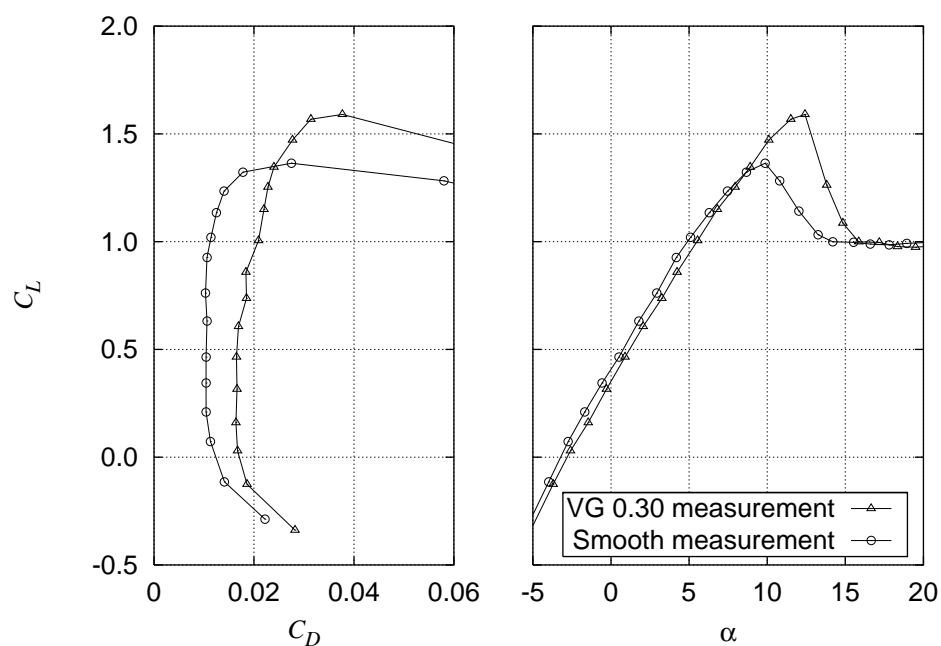
Figure 7-29 C_L-C_D for Risø-A1-24 VG 30% measurement compared with smooth measurements (run081).
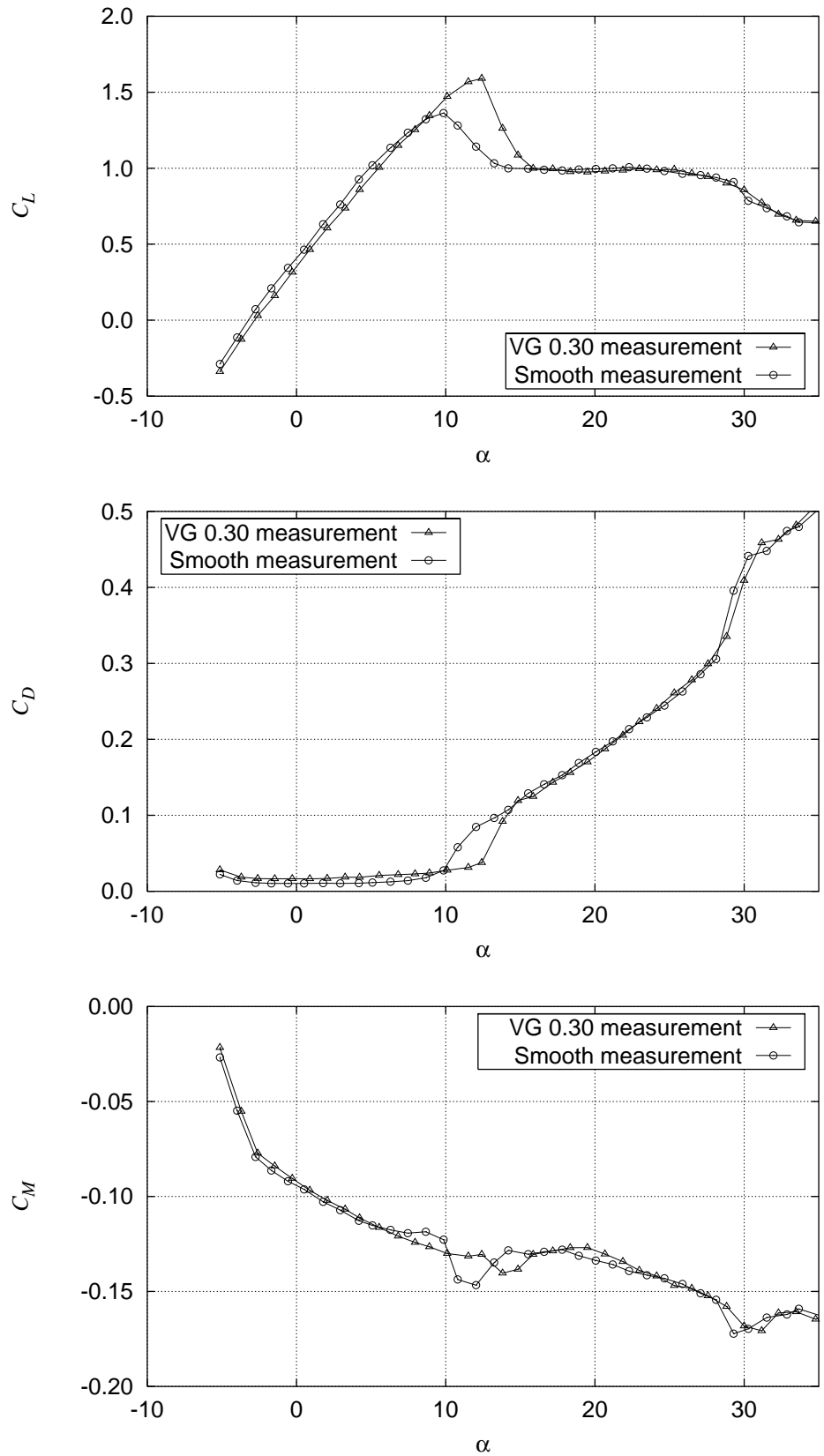
Figure 7-30 C_L, C_D and C_M for Risø-A1-24 VG 30% measurement compared with smooth measurements (run081).

Risø-R-1112(EN)

7.10 Risø-A1-24 GFs of 1% (run037,040)
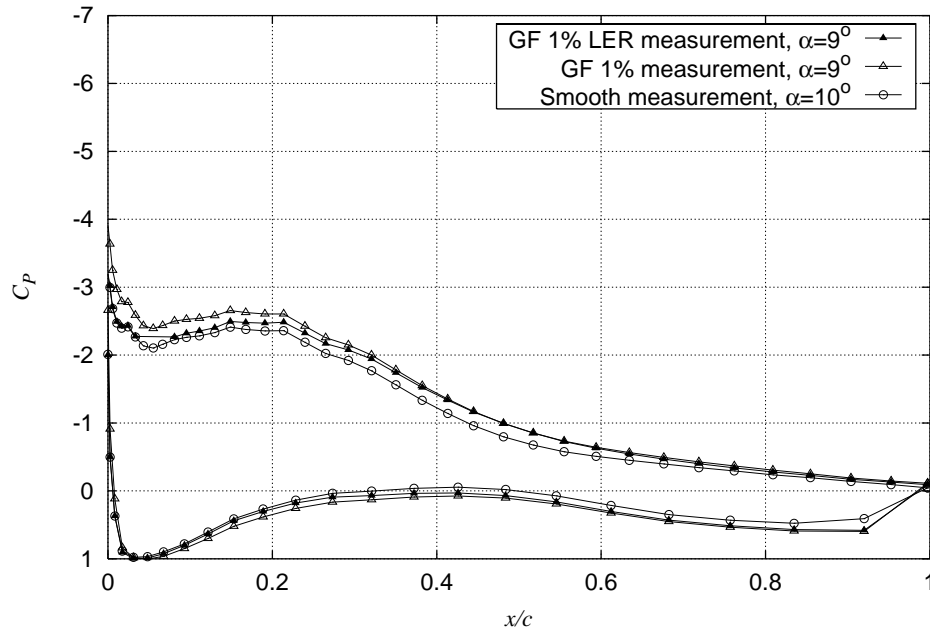
Figure 7-31 C_p at maximum C_L for Risø-A1-24 GF 1% Smooth and LER measurement compared with smooth measurements (run037,040).
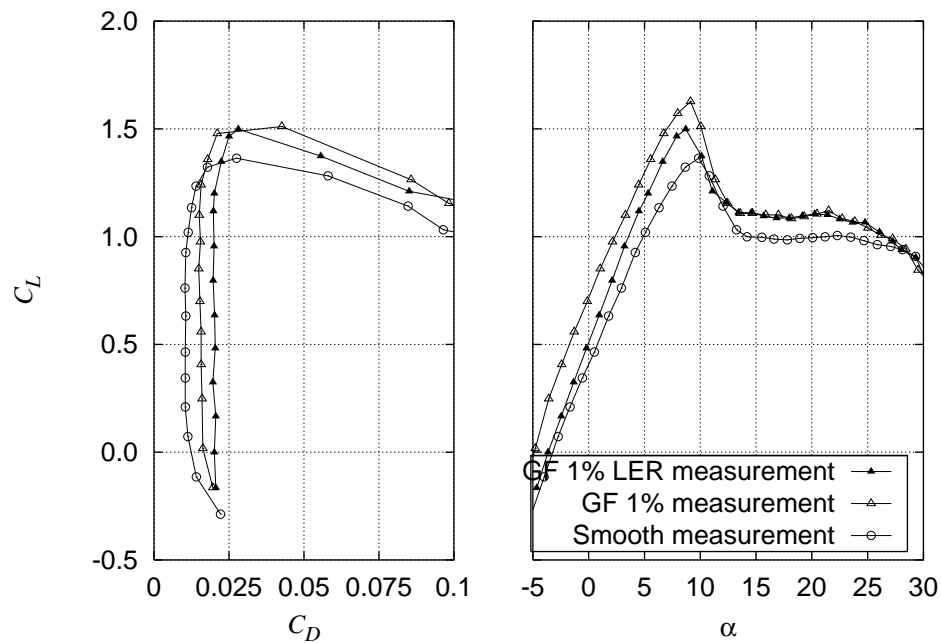
Figure 7-32 C_L-C_D for Risø-A1-24 GF 1% Smooth and LER measurement compared with smooth measurements (run037,040).
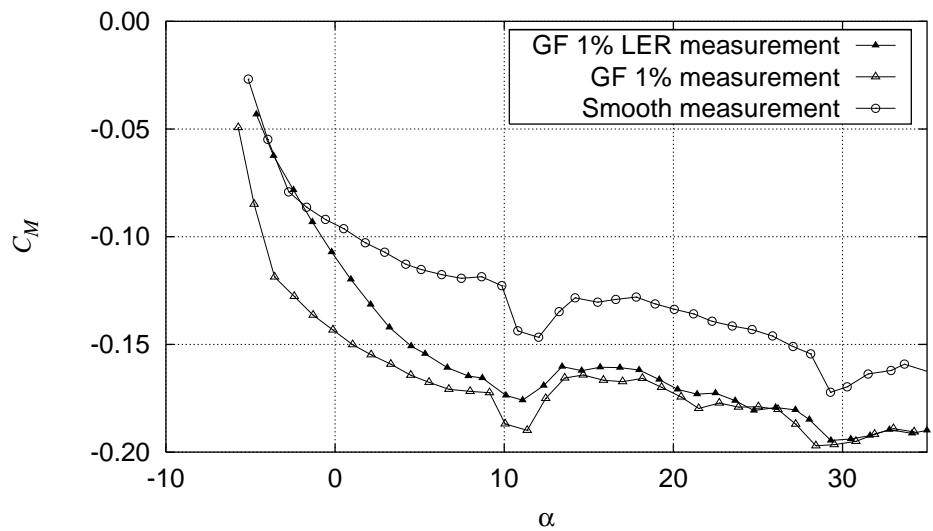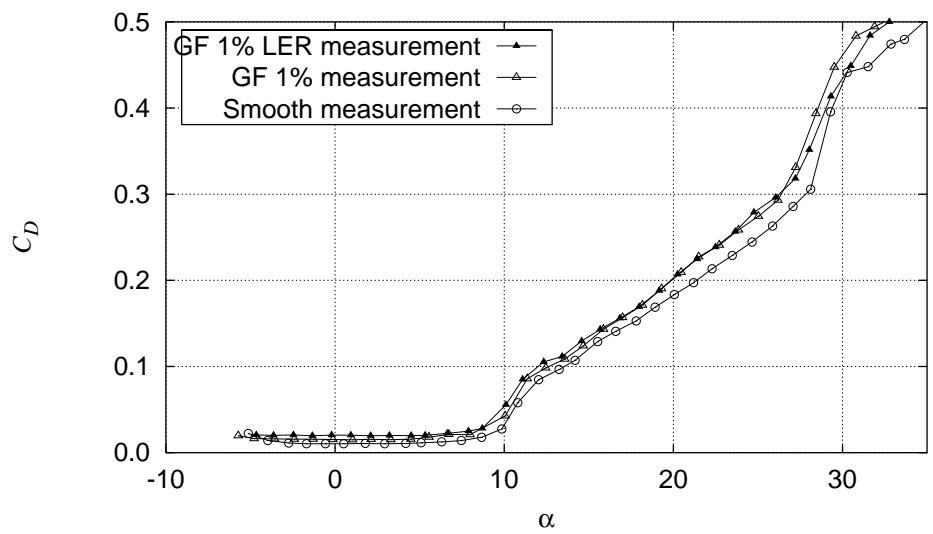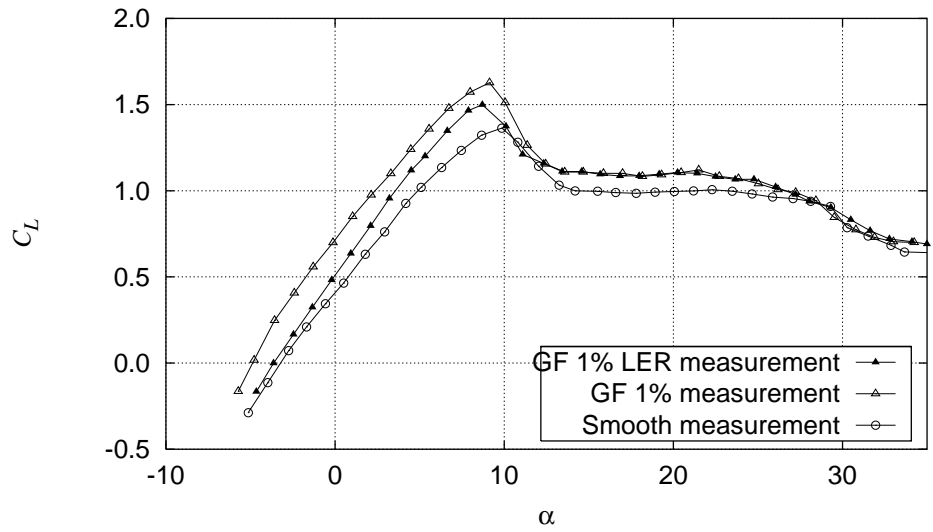
Figure 7-33 C_L, C_D and C_M for Risø-A1-24 GF 1% Smooth and LER measurement compared with smooth measurements (run037,040).

Risø-R-1112(EN)

7.11 Risø-A1-24 GFs of 2% (run038,039)
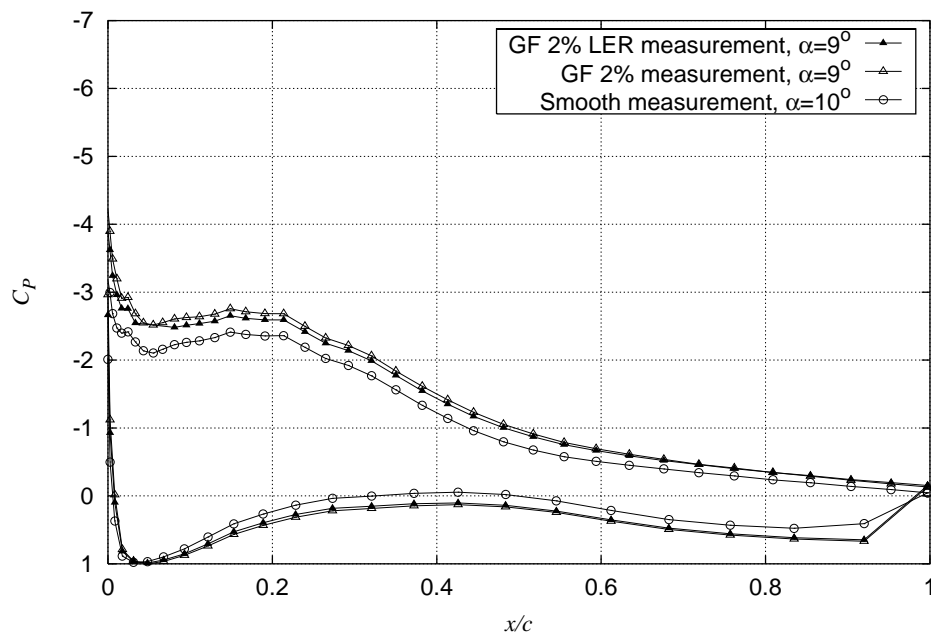
Figure 7-34 C_p at maximum C_L for Risø-A1-24 GF 2% Smooth and LER measurement compared with smooth measurements (run038,039).
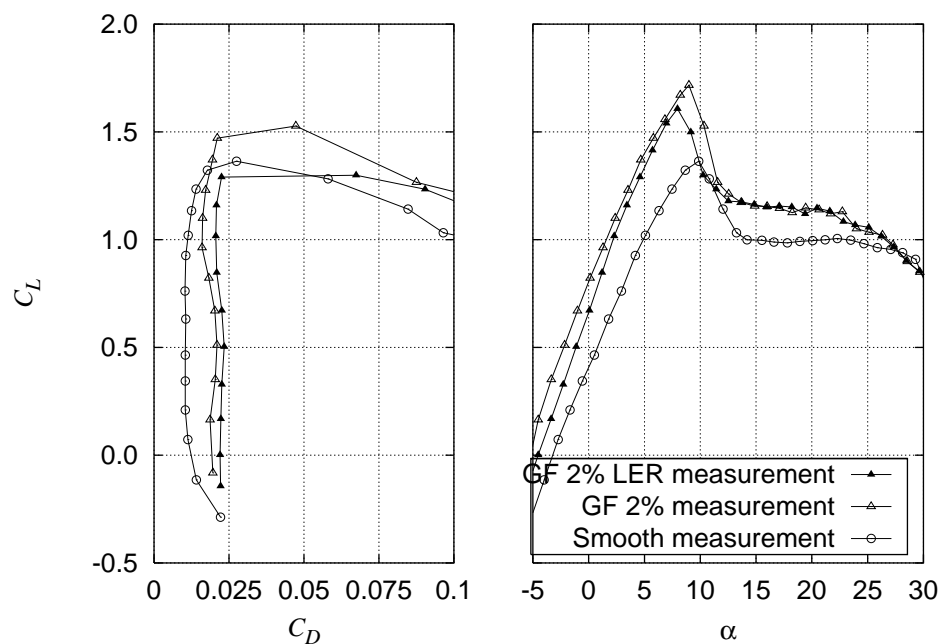
Figure 7-35 C_L-C_D for Risø-A1-24 GF 2% Smooth and LER measurement compared with smooth measurements (run038,039).
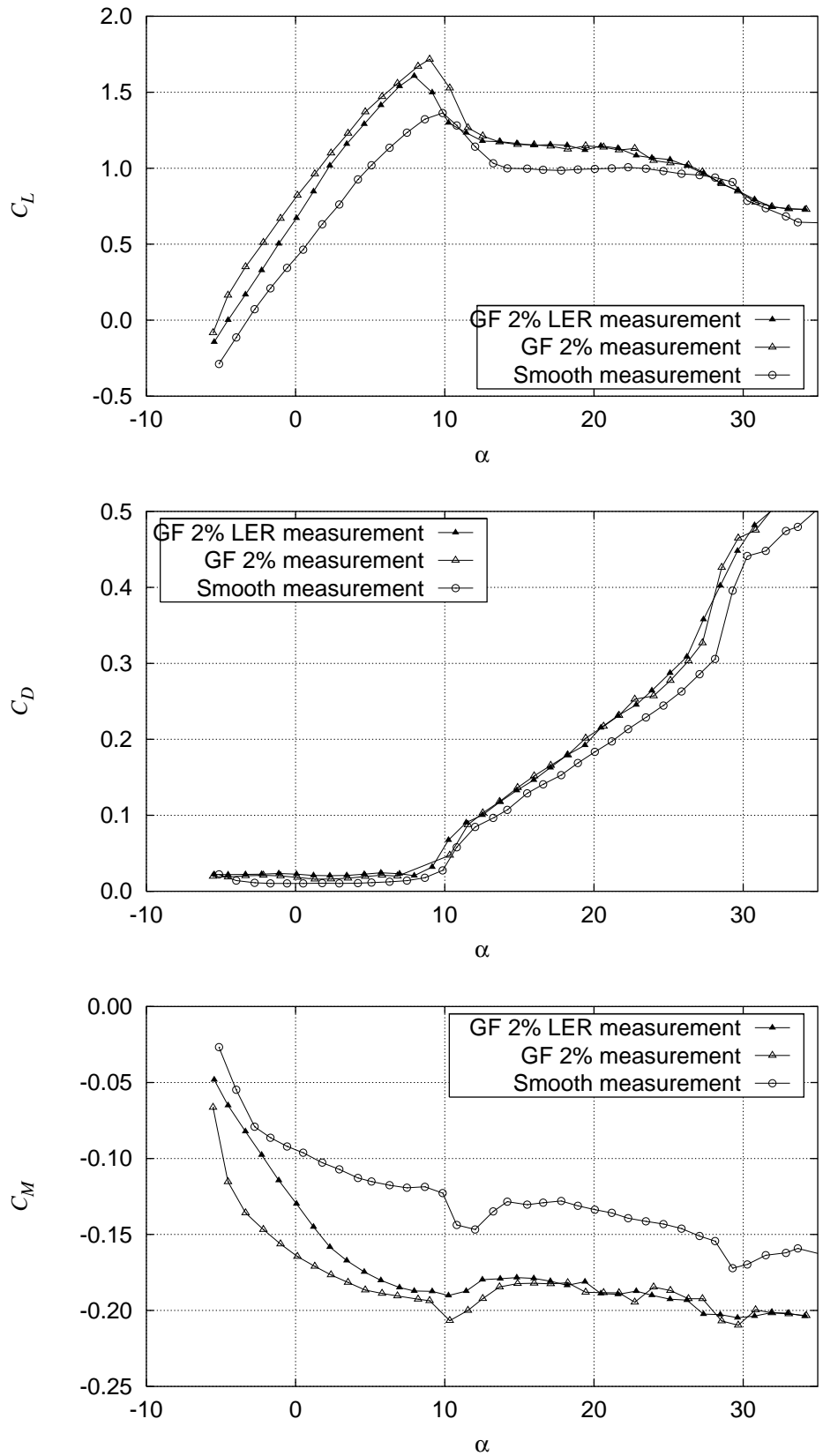
Figure 7-36 C_L, C_D and C_M for Risø-A1-24 GF 2% Smooth and LER measurement compared with smooth measurements (run038,039).

7.12 Risø-A1-24 VGs at 0.10 double spacing (run067,066)
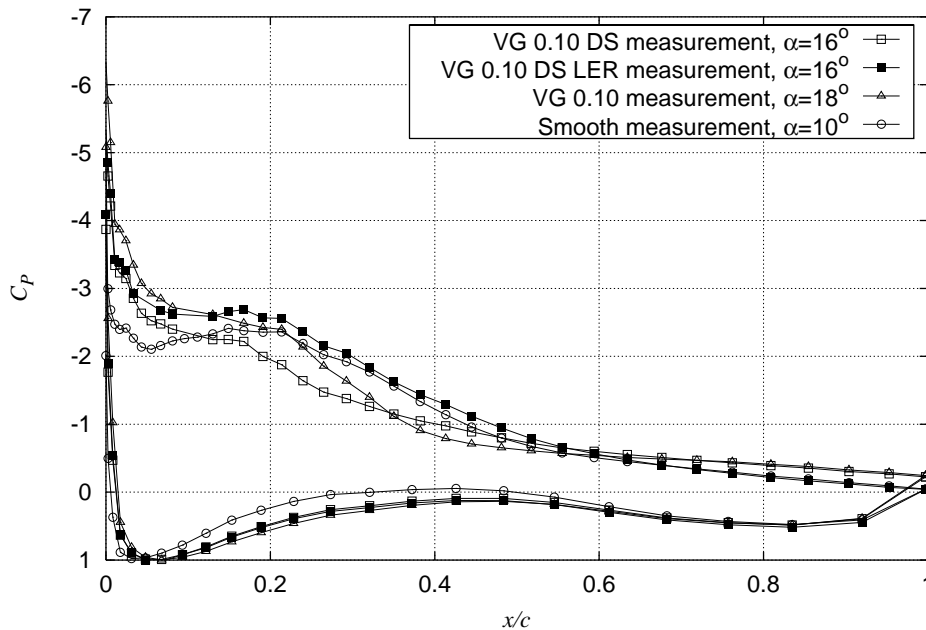
Figure 7-37 C_p at maximum C_L for Risø-A1-24 VG 10% Double spacing smooth and LER measurement compared with VG 10% and smooth measurements (run066,067).
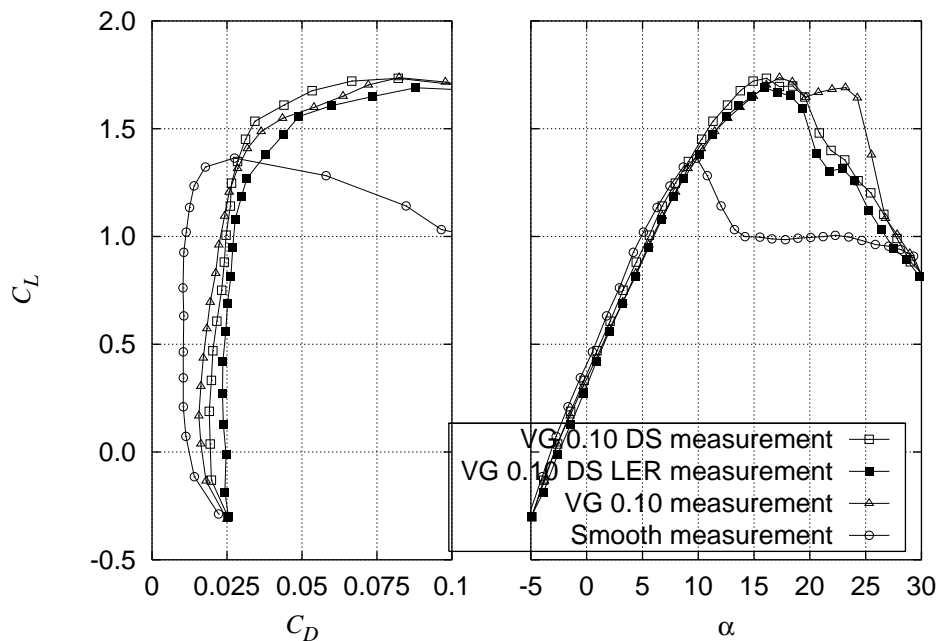
Figure 7-38 C_L-C_D for Risø-A1-24 VG 10% Double spacing smooth and LER measurement compared with VG 10% and smooth measurements (run066,067).
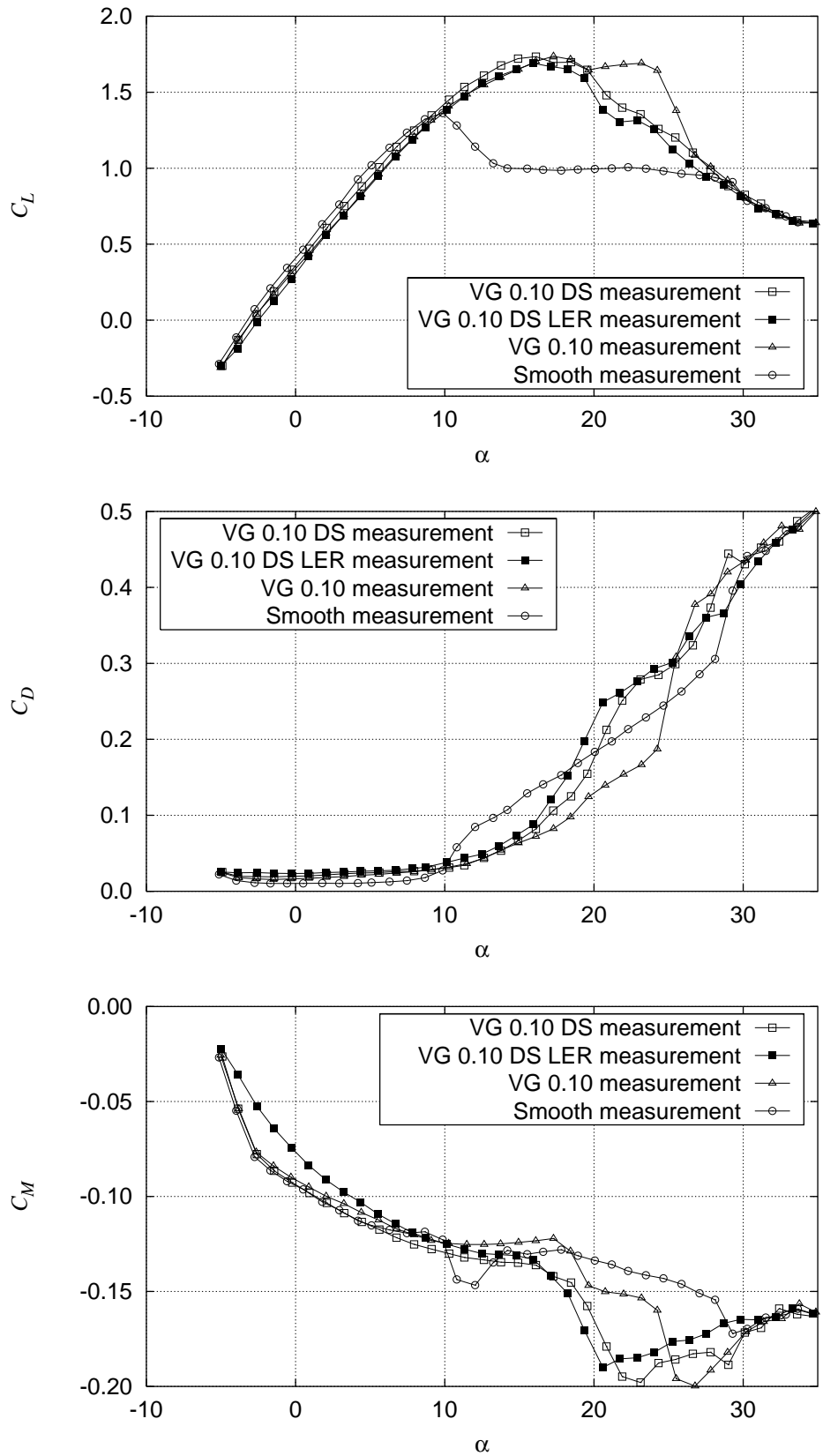
Figure 7-39 C_L, C_D and C_M for Risø-A1-24 VG 10% Double spacing smooth and LER measurement compared with VG 10% and smooth measurements (run066,067).

Risø-R-1112(EN)

7.13 Risø-A1-24 VGs at 0.15, GFs of 1%, LER (run036)
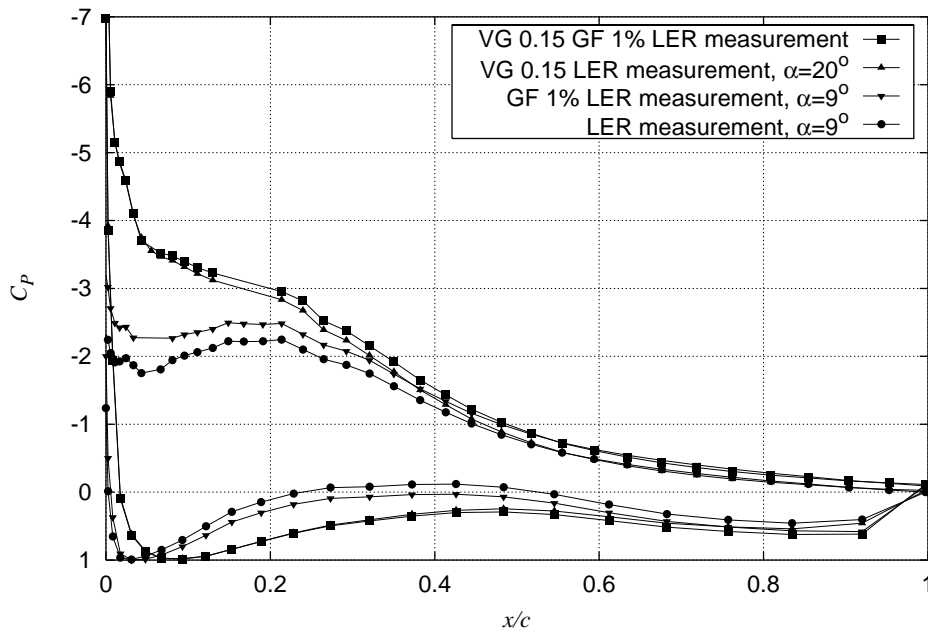
Figure 7-40 C_p at maximum C_L for Risø-A1-24 VG 15% GF 1% LER compared with GF 1% LER, VG 15% LER and LER measurements (run036).
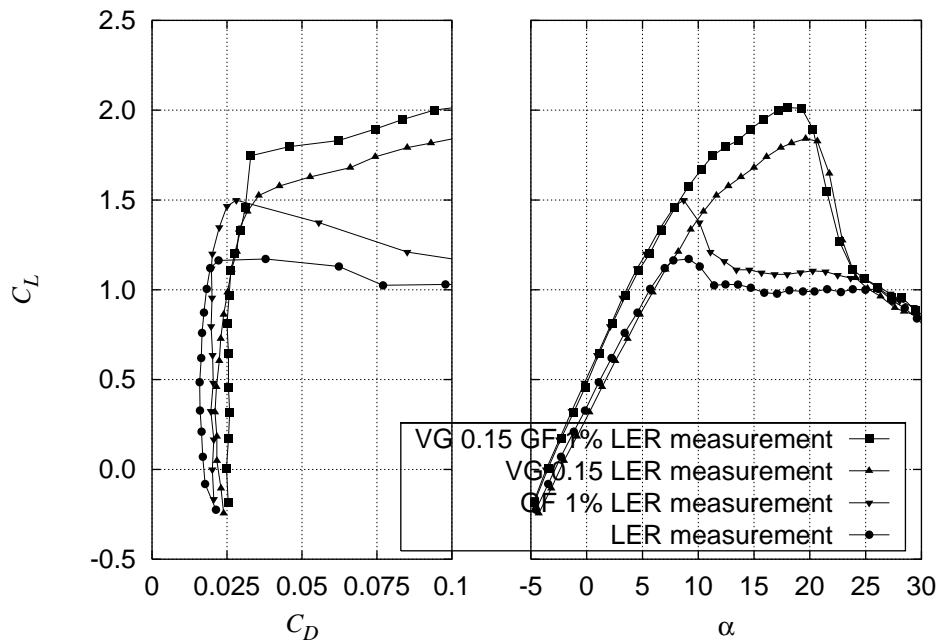
Figure 7-41 C_L-C_D for Risø-A1-24 VG 15% GF 1% LER compared with GF 1% LER, VG 15% LER and LER measurements (run036).
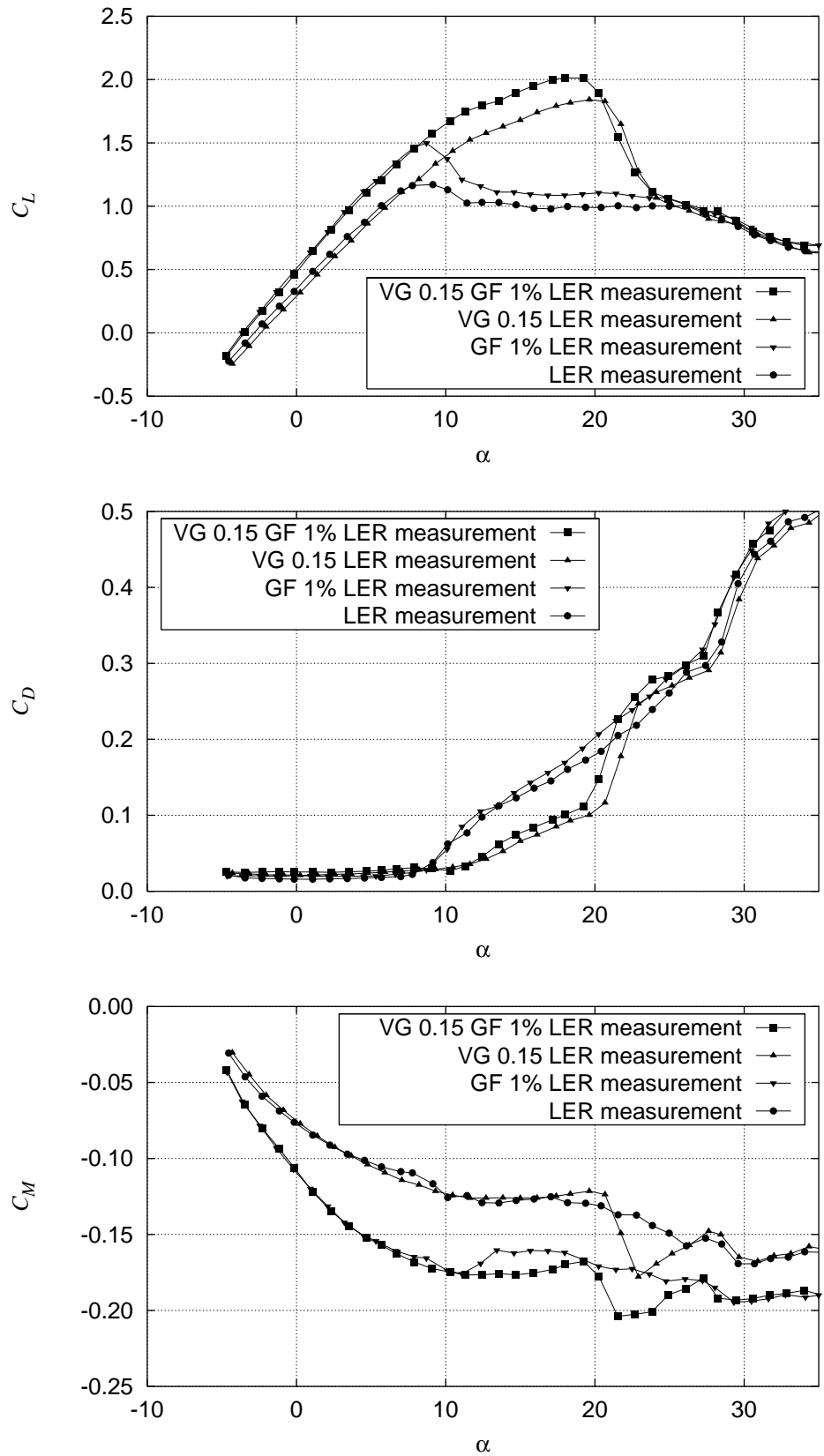
Figure 7-42 C_L, C_D and C_M for Risø-A1-24 VG 15% GF 1% LER compared with GF 1% LER, VG 15% LER and LER measurements (run036).

7.14 Risø-A1-24 Dynamic stall (run043)
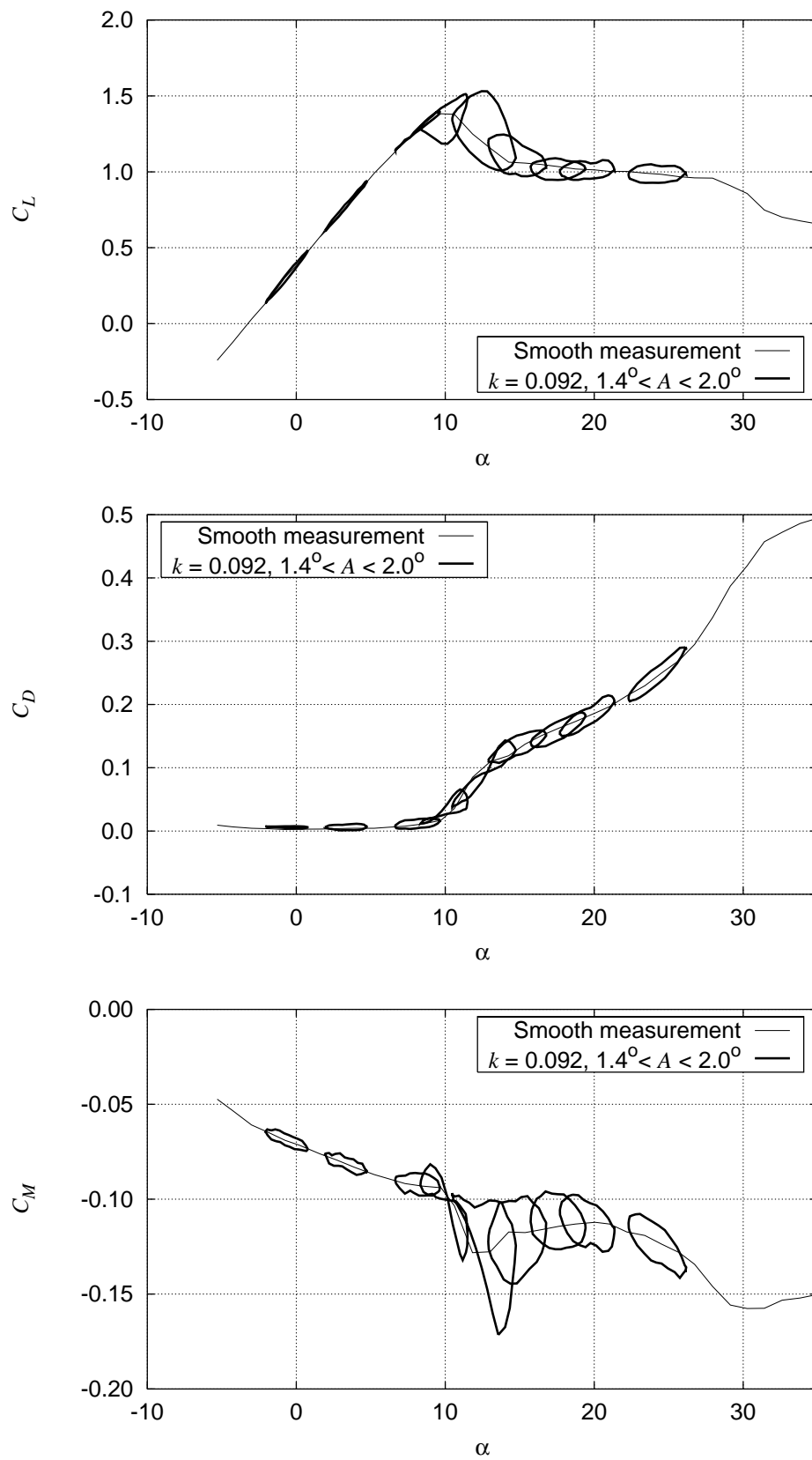
Figure 7-43 C_L, C_D and C_M hysteresis loops for Risø-A1-24 smooth measurement at k = 0.092, A between 1.4° and 2.0° (run043).
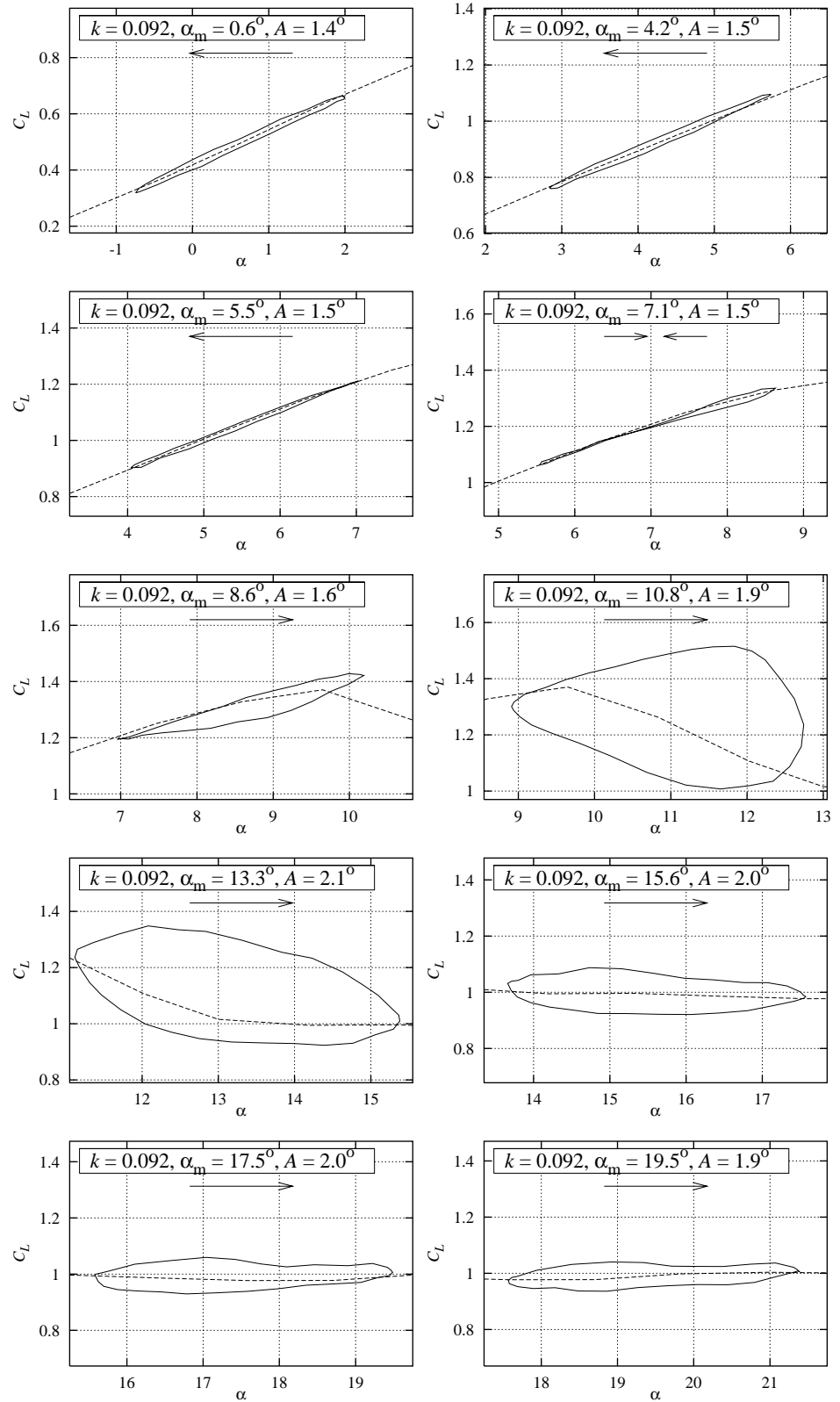
Figure 7-44 C_L hysteresis loops for Risø-A1-24 smooth measurement at k = 0.093, A between 1.4° and 2.0° (run043).
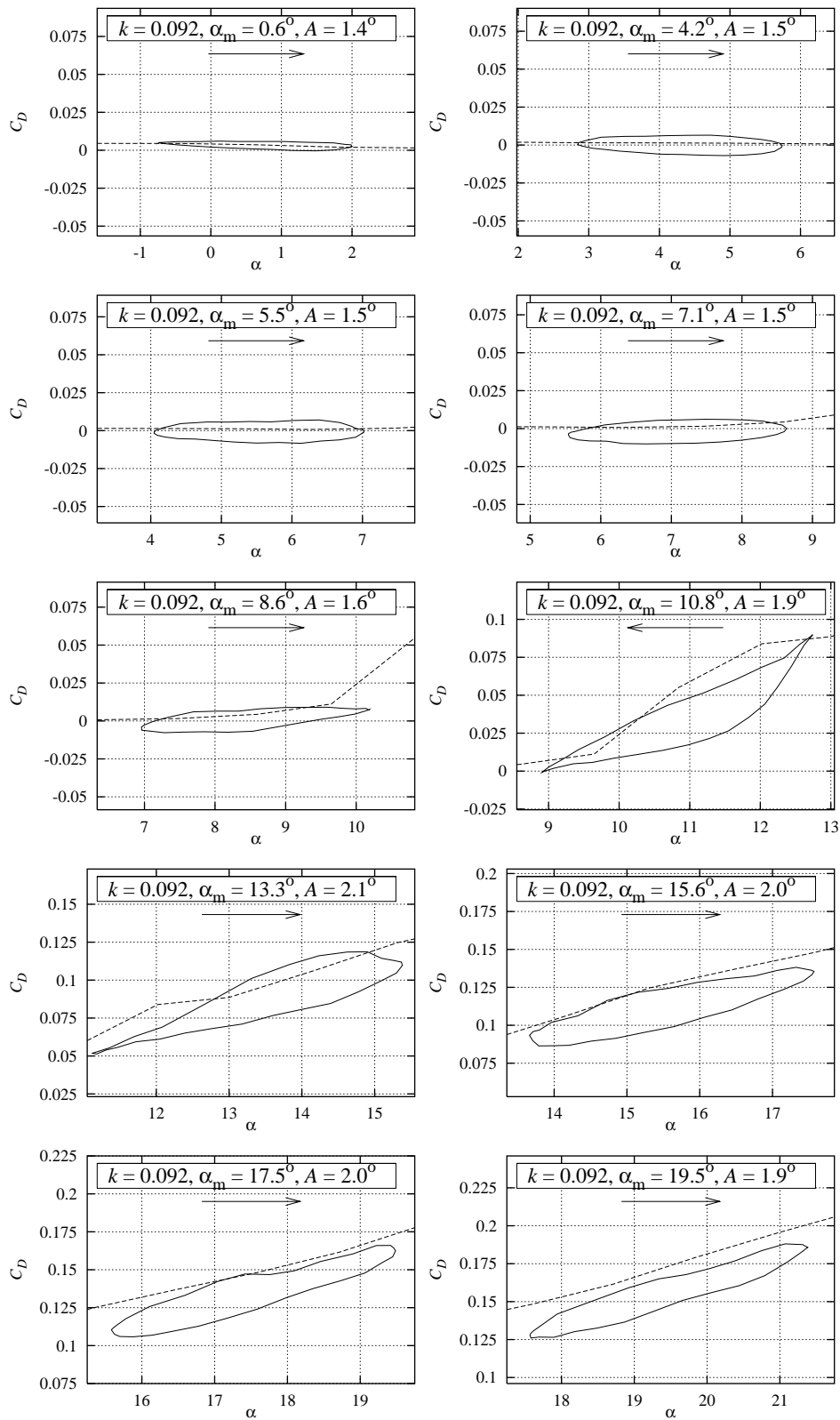
Figure 7-45 C_D hysteresis loops for Risø-A1-24 smooth measurement at k = 0.093, A between 1.4° and 2.0° (run043).
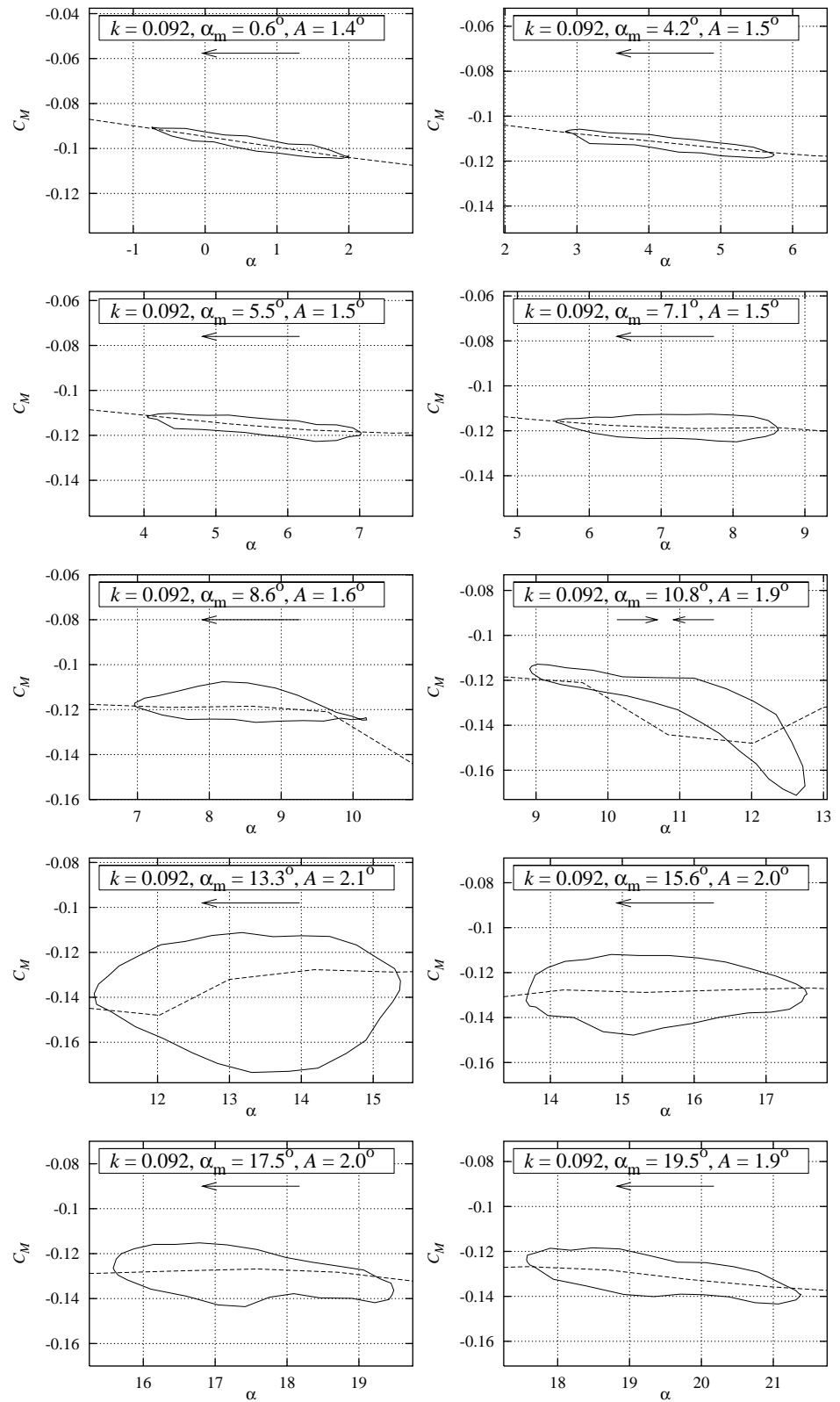
Figure 7-46 C_M hysteresis loops for Risø-A1-24 smooth measurement at k = 0.093, A between 1.4° and 2.0° (run043).

8 Discussion

8.1 Risø-A1-18

Measurements of Risø-A1-18 are shown in Chapter 5 and main results are shown in Table 8-1.

Results of the measurements with smooth surface conditions are shown in Section 5.1 . The slope of the C_L curve remains constant until a C_{Lmax} of about 1.43 is reached at $\alpha = 10°$ and when stall begins a well defined upper limit is set on C_L. In the post stall area C_L is smoothly reduced until deep stall. The measurement of C_D shows a C_{Dmin} of around 0.0097 which is higher than expected. The high background turbulence level of 1% will increase C_D. However, for this particular airfoil section, the high C_D is mainly due to the quality of the airfoil section, where the trailing edge was irregular and the finish around the pressure tabs was bad. Nevertheless it is positive that C_D remains nearly constant until stall occurs.

The constant steep slope of the C_L curve and the low C_D nearly until stall is in agreement with the design strategy where the operational point was designed to be close to C_{Lmax}.

The measurements compare well with computational results from the Navier-Stokes solver, EllipSys2D. Figure 5-2 and Figure 5-3 in Section 5.1 show the measured and computed C_P distributions for $\alpha = 2°$ and $\alpha = 8°$. The latter is just before C_{Lmax} is obtained. The fully turbulent computed C_P distribution is in very good agreement with the measured C_P distribution on the entire airfoil at the lower angles of attack. Differences between measurements and computations occur at higher angles of attack. In Figure 5-3 at the first 5% of the suction side, the free transition computation compares better with the measurement. Hence, the shape of the C_P curve is in good agreement at low angles of attack except for the location of the transition point, which is predicted too far down stream compared to the measurement. At high angles of attack the large acceleration of the suction side flow around the leading edge suppress the turbulence and this causes deviation between the measurements and the turbulent computations.

The measured and the predicted C_{Dmin}, Figure 5-4, and the shape of the C_D curve at low angles of attack are both in good agreement. However, C_{Lmax} could not be correctly predicted when the Michel transition model was used during the computation. Good agreement for C_{Lmax} was obtained for fully turbulent flow computations compared with the smooth flow measurements.

The agreement for C_{Lmax} between the measurement and the fully turbulent flow computation indicates that the measured flow is more or less fully turbulent close to stall. This is in agreement with the design strategy where transition should be located close to leading edge to ensure insensitivity of C_{Lmax} to leading edge roughness. As a result of the design strategy aiming for a roughness insensitive airfoil a small suction peak on the leading edge appears at

α = 8°. The suction peak increases with the angle of attack when getting closer to the stall angle. The peak eventually causes transition from laminar to turbulent flow close to the leading edge making C_{Lmax} insensitive to leading edge roughness. The measurements show that transition occurs at the leading edge also at angles of attack well below the stall angle indicating that the pressure peak that provokes transition either is too pronounced or occurs at too low angles of attack.

Measurements with zigzag tape to represent leading edge roughness are shown in Section 5.2 . Compared with smooth flow C_{Dmin} is increased to 0.012 and C_{Lmax} is reduced to 1.18. The slope of the C_L curve is nearly as steep for leading edge roughness flow as for smooth flow. This is in good agreement with the design strategy aiming for C_{Lmax} being insensitive to leading roughness. However, the drop in C_{Lmax} is somewhat higher than expected from the design calculations. The zigzag tape used to simulate leading edge roughness is also used on small aeroplane wings. It is therefore possible that it represents a massive roughness for the tested airfoil. Hence the deviations from the theoretically expected values can be attributed to he lack of correct roughness simulation.

Measurements with vortex generators (VGs) are shown in Section 5.3 - 5.5 . The C_P distributions for the different VG configurations were obtained directly from the pressure measurements, neglecting the 3d variation in the pressure. The C_P distribution at α = 10° for smooth flow shows that C_P is nearly identical for low angles of attack, Figure 5-9. Hence, the VG's have neglecting influence on C_P when the corresponding smooth flow without VGs is attached. The 3d influence on the pressure is negligible so that the measured C_P distribution is representative for the VG flow. At higher angles of attack, the VGs reduce the pressure on most of the suction side. Separation is delayed to a higher angle of attack and C_{Lmax} is increased. The slope of the linear part of the C_L curve and the angle of attack for zero C_L are not affected by the VGs. The resulting C_{Lmax} depends on the chordwise location of the VGs. For this airfoil $x/c = 0.20$ and $x/c = 0.25$ were measured. At $x/c = 0.20$ C_{Lmax} was increased to 1.82. However, the VGs also increased C_D in the pre-stall region. Compared to the smooth flow measurement in the post stall region C_D remains the same for both smooth and VG conditions. In the area where the flow remains attached due to VGs, C_D remains favourably lower compared to the smooth flow measurements, Figure 5-12.

Unfortunately the reported C_D curves with VGs are not accurate because the wake rake pressures were used for calculation of C_D. There will be a spanwise variation in the momentum downstream of the airfoil section because of the discrete location of the vortex generators. The wake rake represents a snap shot of the flow in one particular spanwise location. Since the wake rake was not traversed a representative average value of C_D could not be obtained.

Both VG configurations were measured with leading edge roughness. The presence of leading edge roughness only marginally reduced C_{Lmax} whereas C_{Dmin} was increased for angles of attack above 0°.

Measurements with smooth surface condition and dynamic inflow are shown in Section 5.6 . Time series were measured with the airfoil section being in a harmonic motion around $x/c = 0.40$ at different mean angles with a geometric maximum amplitude of $A = \pm2°$ and a reduced frequency of $k = 0.092$. The

derivation of the hysteresis loops from time series is explained in Fuglsang et al., [2]. When wind tunnel corrections are applied for the angle of attack, the amplitude of the harmonic motion is changed.

Table 8-1 C_{Lmax} and C_{Dmin} for Risø-A1-18.

	Smooth	LER	VG 0.20	VG 0.20 LER	VG 0.25	VG 0.25 LER
C_{Lmax}	1.43	1.18	1.82	1.75	1.76	1.66
C_{Dmin}	0.0097	0.012	0.016	0.017	0.015	0.016

8.2   Risø-A1-21

Measurements of Risø-A1-21 are shown in Chapter 6 and main results are shown in Table 8-2.

Results of measurements with smooth surface conditions are shown in Section 6.1 . The measured C_P distribution is slightly irregular on the rear part of the suction side. This is due to measurement errors but it will not affect the derivation of C_L. The overall measurements show similar trends as for the Risø-A1-18 airfoil with a C_{Lmax} of about 1.38 and C_{Dmin} of about 0.0092.

In the post stall area the C_L curve slope is negative and rather steep Figure 6-5. In combination with Figure 6-1 this shows, that the airfoil has a well-defined stall characteristic. Stall occurs at around 10° and moves rapidly to the leading edge within an angle of attack range of 4°. Due to the thickness of the airfoil this is not unexpected. However, at the design stage a smaller drop in C_L was intended.

The measurements compare well with the computational results from EllipSys2D with similar trends as for Risø-A1-18 with even better agreement of C_{Dmin}.

Measurements with leading edge roughness are shown in Section 6.2 . Compared with smooth flow C_{Dmin} is increased to 0.014 and C_{Lmax} is reduced to 1.20. Conclusions regarding roughness insensitivity are the same as for Risø-A1-18.

Measurements with VGs are shown in Section 6.3 - 6.5 . C_{Lmax} is increased to 1.89 for the $x/c = 0.20$ configuration and 1.67 for the $x/c = 0.25$ configuration. C_D is higher for the $x/c = 0.20$ configuration compared with the $x/c = 0.25$ configuration. The choice for the chordwise location of the VGs is crucial for the obtainable C_{Lmax} and C_D since large variations occur for small shifts of their position. This is in contrast to the Risø-A1-18 airfoil where C_{Lmax} was almost the same for the measured VG configurations

Both VG configurations were measured with leading edge roughness and this only marginally reduced C_{Lmax} whereas C_{Dmin} was increased.

Measurements with smooth surface conditions and dynamic inflow are shown in Section 6.6 . The geometric amplitude is $A = \pm 2°$ and the reduced frequency is $k = 0.092$.

Table 8-2 C_{Lmax} and C_{Dmin} for Risø-A1-21.

	Smooth	LER	VG 0.20	VG 0.20 LER	VG 0.25	VG 0.25 LER
C_{Lmax}	1.38	1.20	1.89	1.85	1.67	1.60
C_{Dmin}	0.0092	0.014	0.020	0.022	0.017	0.018

8.3   Risø-A1-24

Measurements of Risø-A1-24 are shown in Chapter 7 and main results are shown in Table 8-3 to Table 8-5.

Results of measurements with smooth surface conditions are shown in Section 7.1 . The overall measurements show similar trends as for the other tested airfoils. C_{Lmax} is about 1.36 and C_{Dmin} is about 0.010. As for the Risø-A1-21 airfoil there is a significant drop in C_L during post stall.

The measurements are in good agreement with the computational results from EllipSys2D with similar trends as for the other tested airfoils.

Measurements with leading edge roughness are shown in Section 7.2 . Compared with smooth flow C_{Dmin} is increased to 0.016 and C_{Lmax} is reduced to 1.17. Conclusions regarding roughness insensitivity are the same as for the other tested airfoils.

Measurements with VGs are shown in Section 7.3 , 7.5 -7.9 and 7.12 . The obtainable C_{Lmax} depends on the chordwise location of the VGs. When the VGs are moved closer to the leading edge C_{Lmax} is increased until x/c = 0.15 where a C_{Lmax} around 1.90 is obtained. Moving the VGs further upstream results in an entirely different flow pattern with a lower C_{Lmax} and a smoother post stall area. When the VGs are moved toward the leading edge C_{Dmin} is also increased.

When the VGs increase C_{Lmax} to very high values it is inevitable that there will be a large drop in C_L in the post stall area. However, the angles of attack where the drop occurs are so high that the flow on a rotor inboard part will have a complex 3d-flow pattern. This will to some extent counterbalance the 2D drop in C_L.

A measurement with larger spacing between the VGs at x/c = 0.10 is shown in Section 7.12 . The larger spacing does not seem to reduce C_{lmax}. However, C_L in the post stall area is reduced. This indicates that the spacing is equally important as the chordwise location when the VG configuration is optimised.

Measurements with Gurney flaps (GFs) are shown in Section 7.4 , 7.10 and 7.11 . The measured C_P distributions show that GFs increase the area inside of the C_P curve giving higher C_L. To the same angle of attack, C_L is increased. This moves the angle of attack for zero C_L towards negative. The angle of attack for C_{Lmax} is not influenced by the GFs. C_{Lmax} is measured to about 1.72 at a GF height of 2% with a C_{Dmin} about 0.016. A drawback from GFs is a large drop in C_L during post stall.

From the measurement of the significant increase in C_D compared with smooth flow it appears that measurements should have been carried out with lower height of the GFs compared to 1%. From this it could be expected that C_D would not increase so much but that there would still be an increase in C_{Lmax}.

The GF measurements show the importance of the shape of the trailing edge. A deviation in the trailing edge angle with the chord can cause a different angle of attack for zero C_L and a different C_{Lmax}

A measurement with VGs, GFs and leading edge roughness is shown in Section 7.13 . The combination of VGs and GFs increase C_{Lmax} to about 2.0. VGs and GFs supplement each other well and the measurement is an example of that very high C_{Lmax} can be achieved by simultaneous application of VGs and GFs.

Measurements with smooth surface condition and dynamic inflow are shown in Section 7.14 . The geometric amplitude is $A = \pm 2°$ and the reduced frequency is $k = 0.092$.

Table 8-3 C_{Lmax} and C_{Dmin} for Risø-A1-24 smooth, LER and GF.

	Smooth	LER	GF 1%	GF 1% LER	GF 2%	GF 2% LER	GF 1% VG 0.15 LER
C_{Lmax}	1.36	1.17	1.63	1.50	1.72	1.61	2.02
C_{Dmin}	0.010	0.016	0.015	0.020	0.016	0.021	0.025

Table 8-4 C_{Lmax} and C_{Dmin} for Risø-A1-24 VG.

	VG 0.10	VG 0.10 DS	VG 0.15	VG 0.20	VG 0.25	VG 0.30
C_{Lmax}	1.74	1.68	1.90	1.81	1.67	1.59
C_{Dmin}	0.016	0.024	0.017	0.019	0.016	0.017

Table 8-5 C_{Lmax} and C_{Dmin} for Risø-A1-24 VG LER.

	VG 0.10 LER	VG 0.10 DS LER	VG 0.15 LER	VG 0.20 LER	VG 0.25 LER
C_{Lmax}	1.65	1.69	1.84	1.77	1.66
C_{Dmin}	0.020	0.024	0.021	0.019	0.021

8.4   Summary

Measurements of C_L and C_D for Risø-A1-18, Risø-A1-21 and Risø-A1-24 airfoils for smooth surface conditions and leading edge roughness are shown in Figure 8-1 and Figure 8-2 respectively.

All airfoils have very similar characteristics at smooth surface conditions except for post stall where Risø-A1-21 and Risø-A1-24 have a larger drop in C_L compared with Risø-A1-18. With leading edge roughness the variation in C_D is larger with higher C_{Dmin} for thicker airfoils. However, all airfoils have approximately the same C_{Lmax}.
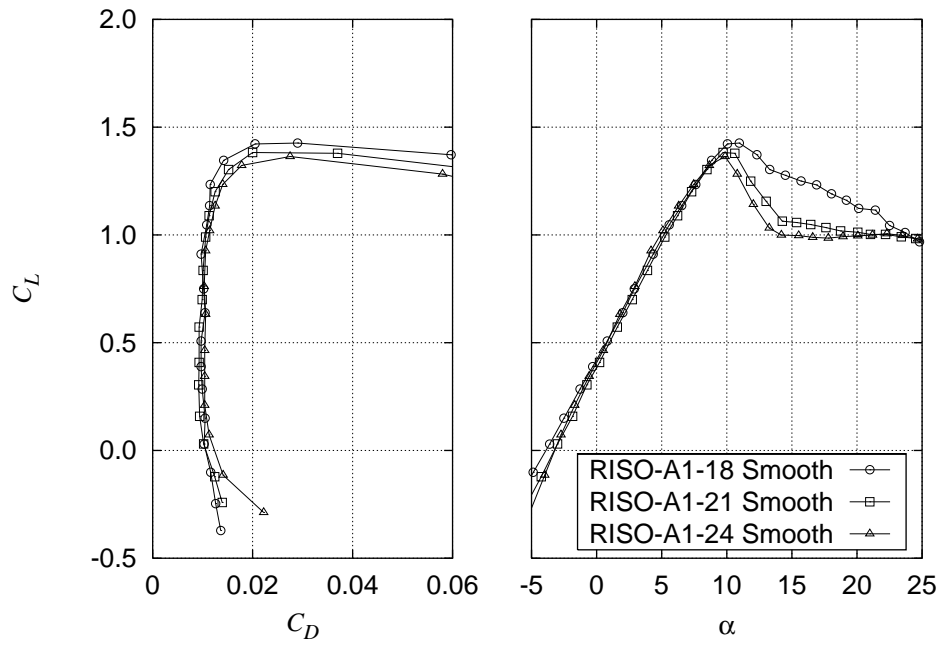
Figure 8-1 C_L-C_D for Risø-A1-18, Risø-A1-21 and Risø-A1-24 smooth measurements.
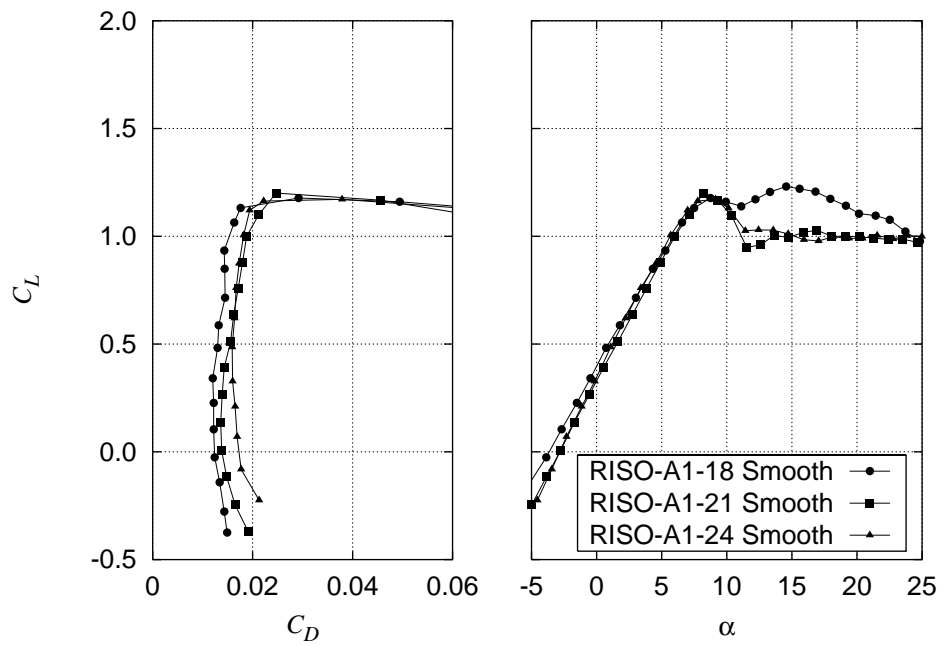
Figure 8-2 C_L-C_D for Risø-A1-18, Risø-A1-21 and Risø-A1-24 LER measurements.

9 Conclusions

The Risø-A1 airfoil family was designed with operational Reynolds numbers around 3.0 million for a 600 kW wind turbine rotor with the following characteristics:

- Maximum lift coefficient around 1.5 in natural conditions for all airfoils
- High lift-drag ratio also at high angles of attack just below maximum lift
- Insensitivity to leading edge roughness for the maximum lift coefficient
- Trailing edge stall, smooth post stall behaviour and no double stall

To address the agreement between the design characteristics and the actual airfoil performance three of the airfoils, Risø-A1-18, Risø-A1-21 and Risø-A1-24 were tested experimentally in a wind tunnel. The testing conditions corresponded to the maximum flow velocity of 42 m/s giving a Reynolds number of, $Re = 1.6 \times 10^6$ compared with the design Reynolds numbers around $Re = 3.0 \times 10^6$. According to Navier-Stokes calculations the difference in Reynolds number would reduce the maximum lift coefficient by approximately 0.1 reducing the design maximum lift coefficient from 1.5 to 1.4. The tunnel has a relatively high background turbulence level of 1% making the results more representative for natural conditions than it would be the case for a low turbulence wind tunnel.

For smooth surface conditions, all three airfoils had the desirable properties of constant lift curve slope and almost constant drag coefficient until maximum lift is reached. The maximum lift coefficient and the minimum drag coefficient for the airfoils were about 1.4 and 0.010 respectively.

Tests on all airfoil sections mounted with zigzag tape to simulate leading edge roughness showed that the airfoils were reasonably insensitive to this. An increase in the minimum drag coefficient to about 0.014 was inevitable. The maximum lift coefficient was reduced to about 1.2. The zigzag tape did not affect the slope of the lift coefficient versus angle of attack. The drop in maximum lift was somewhat higher than expected during the airfoil design. This indicated that the zigzag tape was not dimensioned properly, relative to the size of the airfoils.

The measurements in post stall showed that the Risø-A1-18 airfoil had a smooth post stall area with high lift coefficient retained until deep stall. Unfortunately measurements of Risø-A1-21 and Risø-A1-24 showed a larger drop in the lift coefficient than expected during post stall indicating massive separation on the suction side, which was not foreseen to this extent during the airfoil design.

Mounting of vortex generators and Gurney flaps showed that there was room for improvement of the aerodynamic properties of the airfoils by relatively simple means. The improvements can be applied with good results especially on the inner parts of wind turbine blades. All airfoils were well suited for application of vortex generators, e.g., vortex generators for Risø-A1-24 in 15% chord increased the maximum lift coefficient from 1.38 to 1.90. The combination of vortex generators and Gurney flaps increased the maximum lift

coefficient to about 2.0. The drag penalty has to be considered individually according to the application. Unfortunately the measurements of drag at the vortex generator and Gurney flap configurations was uncertain since the wake rake was not traversed to obtain an average value representative to 2-dimensional flow.

The experimental results for smooth surface conditions compare well with computational results from the general-purpose Navier-Stokes solver, EllipSys2D. The minimum drag coefficient and the shape of the drag curve at low angles of attack were in very good agreement. However, the maximum lift coefficient could not be predicted when transition was included in the computation. Good agreement for the maximum lift coefficient compared with the measurements was obtained for fully turbulent flow computations.

References

[1]   Fuglsang, P., Dahl, K.S., 1999, 'Design Of The New Risø-A1 Airfoil Family for Wind Turbines,' Proc. EWEC'99, Nice, France.

[2]   Fuglsang, P., Antoniou, I., Sørensen, N.N., Madsen, H. Aa., 1998, 'Validation of a Wind Tunnel Testing Facility for Blade Surface Pressure Measurements.' Risø-R-981(EN), Risø National Laboratory, Denmark.

[3]   Rae Jr., W.H., Pope, A., 1984, Low-Speed Wind Tunnel Testing, SE, John Wiley & Sons, ISBN 0-471-87402-7.

[4]   Brooks, T.F. and Marcolini, M.A., 1984, Airfoil Trailing Edge Flow Measurements and CompaRisøn with Theory Incorporating Open Wind Tunnel Corrections, AIAA-84-2266, AIAA/NASA 9th Aeroacoustic Conference.

[5]   Hoerner, S.F. and Borst, H.V., 1975, Fluid-Dynamic Lift, Hoerner Fluid Dynamics, P.O. Box 342, Brick Town, N.J. 08723, USA.

[6]   Timmer, W.A., 1992, The design and testing of airfoil DU 91-W2-250. Proc. IEA Joint Action. Aerodynamics of Wind Turbines. 6th Symposium.

[7]   Sørensen, N.N., 1995, General Purpose Flow Solver Applied to Flow over Hills, Risø-R-827(EN), Risø National Laboratory, Denmark.

[8]   Menter, F.R., 1993, Zonal Two Equation k-ω Turbulence Models for Aerodynamic Flows. AIAA Paper 93-2906.

[9]   Michel, R., 1952, Etude de la transition sur les profiles d'aile. ONERA Report 1/1578-A. See White F.M., Viscous fluid flow, p. 442.

[10]   Fuglsang, P., Antoniou, I., Dahl, K.S., Madsen, H.Aa., 1998, 'Wind Tunnel Tests of the FFA-W3-241, FFA-W3-301 and NACA 63-430 Airfoils.' Risø-R-1041(EN), Risø National laboratory, Denmark.

A Measurement survey

This appendix describes the performed measurements in detail to make the measurements stored on CD available for subsequent exploitation. The different measurement types are described and the naming convention for the data files is explained. The format of the data files is given and each performed measurement is listed and described.

A.1 List of symbols

h	[cm]	Wake rake vertical position, positive toward floor, origin at wake rake top
k		Reduced frequency
p	[Pa]	Static pressure
p_o	[Pa]	Total pressure head
p_{atm}	[Pa]	Atmospheric pressure
q	[Pa]	Dynamic pressure
x		Airfoil chordwise co-ordinate relative to chord, positive toward trailing edge, origin at leading edge
y		Airfoil vertical co-ordinate relative to chord, positive toward ceiling, origin at leading edge
A	[°]	Pitch motion amplitude
C_D		Drag coefficient
C_L		Lift coefficient
C_M		Moment coefficient
C_P		Airfoil pressure coefficient
Re		Reynolds number
t	[°C]	Air temperature
α	[°]	Angle of attack
ρ	[kg/m^3]	Air density
Subscripts		
c		Corrected value
p		Pressure measurement (opposite to wake rake measurement)
w		Wake rake measurement
∞		Reference for normalisation of airfoil forces

A.2 Measurement types

There are four different basic types of measurements of the airfoil flow as shown in Table A-1:

- STEP
- CONT
- STAT
- PITCH

Table A-1 Overview of the different types of measurements that have been performed.

STEP
The lift, drag and moment polar versus angle of attack.
• Discrete measurements at different angles of attack. • Angle of attack range: -6° to 30°. • Interval between different angles: 1° to 4°. • Time series length: 20 s. • Sampling frequency: 5 Hz.
CONT
The lift, drag and moment polar versus angle of attack. (shorter measurement time compared to 'STEP')
• Continuous measurements at different angles of attack. • Angle of attack range: -6° to 30°. • Rate of change of angle of attack: 0.1°/s to 0.5°/s (manually changed). • Time series length app: 250 s. • Sampling frequency: 50 Hz.
STAT
Time series of airfoil flow at different angles of attack, usually in stall.
• Stationary measurements at different angles of attack. • Time series length: 20s to 180s. • Sampling frequency: 100 Hz.
PITCH
Time series of unsteady airfoil flow from pitching motion for determination of hysteresis loops for lift, drag and moment at different pitching frequencies and amplitudes.
• Dynamic measurements at different mean angles of attack with the airfoil in pitching motion. • Pitching amplitude: 2° to 6° • Reduced frequency: to 0.15 • Time series length: 30s to 40s. • Sampling frequency: 100 Hz.

The following table contains a list of all the data files that are available for each type of measurement. A detailed description of the data files is given in Section A.4.

Table A-2 Overview of the available data files for each measurement type.

STEP	
rxx.pol	Average general results where the average of each sub measurement is written in rows, Table A-4. Well suited to obtain C_L and C_D versus α.
cp.pol	Average C_P distributions where the average of each sub measurement is written in columns. Well suited to obtain C_P distributions at different angles of attack (from rxx.pol).
v_w.pol	Average wake rake velocity distributions where the average of each sub measurement is written in columns.
rxx-5hz.nnn	Raw data as rows in general data file with frames of 5 Hz, Table A-4.
cp-5hz.nnn	C_P distribution in columns with frames of 5 Hz.
v_w-5hz.nnn	Wake velocity distribution in columns with frames of 5 Hz.
CONT	
rxx.bin	Average results where raw data are sorted in bins of the angle of attack, Table A-6. Well suited to obtain C_L, C_D and C_M versus α.
rxx.pol	Raw data as rows in general data file with frames of 50 Hz. First 15 columns of data file described in Table A-4. All sub measurements are merged together in one file
rxx-1hz.nnn	Raw data as rows in general data file reduced to frames of 1 Hz, Table A-4.
rxx-10hz.nnn	Raw data as rows in general data file reduced to frames of 10 Hz, Table A-4.
rxx-50hz.nnn	Raw data as rows in general data file with frames of 50 Hz, Table A-4.
cp-1hz.nnn	C_P distribution in columns reduced to frames of 1 Hz.
v_w-1hz.nnn	Wake velocity distribution in columns reduced to frames of 1 Hz.
STAT	
rxx.nnn	Raw data as rows in data file with frames of 50 Hz, Table A-5.
rxx-1hz.nnn	Raw data as rows in general data file reduced to frames of 1 Hz, Table A-4.
rxx-10hz.nnn	Raw data as rows in general data file reduced to frames of 10 Hz, Table A-4.
rxx-50hz.nnn	Raw data as rows in general data file with frames of 50 Hz, Table A-4.
cp-1hz.nnn	C_P distribution in columns reduced to frames of 1 Hz.
v_w-1hz.nnn	Wake velocity distribution in columns reduced to frames of 1 Hz.
PITCH	
rxx-loop.bin	Average results where raw data are sorted in bins of the phase angle of the hysteresis loop, Table A-7. Well suited to obtain hysteresis loops of C_L and C_D and C_M versus α.
rxx.nnn	Raw data as rows in data file with frames of 100 Hz, Table A-5.
rxx-100hz.nnn	Raw data as rows in general data file with frames of 100 Hz, Table A-4.

Where
xx is the measurement run number
yy is the frame resolution in Hz
nnn is the sub measurement number

A.3   Data file naming convention

The different data files are stored in the following directory structure:
- The name of the airfoil.
- The measurement run name.

The naming and the format of the data files is explained in Table A-3.

A.4   Data file formats

The different data files are shown in Table A-3.

Table A-3 Available data files.

rxx-yyhz.nnn	
xx	Measurement run number
yy	Frame average frequency: 100, 50, 10, 5 or 1
nnn	measurement sub number
General data file with each measurement frame/average formatted in rows. The first two rows contain the column number and the sensor name. The format of the data files is described in Table A-4	
STEP	Measurements are given with 5 Hz frame resolution
CONT	Measurements are given with 50 Hz, 10 Hz and 1 Hz frame resolutions respectively
STAT	Measurements are given with 50 Hz, 10 Hz and 1 Hz frame resolutions respectively
PITCH	Measurements are given with 100 Hz resolution

rxx.nnn	
xx	Measurement run number
nnn	measurement sub number
Raw data file with each measurement frame/average formatted in rows. The first two rows contain the column number and the sensor name. The format of the data files is described in Table A-5.	
PITCH	Measurements are given with 100 Hz frame resolution
STAT	Measurements are given with 50 Hz frame resolution

rxx.pol	
xx	Measurement run number
General data file with overall average values of each sub measurement formatted in rows, as above. All sub measurement for a given measurement run are assembled into one single file. The format of the data files is described in Table A-4.	
STEP	Measurements are given with a 20 s average value for each sub measurement
PITCH	Measurements are given with a 30 s average value for each sub measuremen
STAT	Measurements are given with a 180 s average value for each sub measurement

rxx.pol	
xx	Measurement run number
General data file with each measurement frame formatted in rows, as above. All sub measurement for a given measurement run are assembled into one single file. The format of the data files is described in Table A-4, but the files contain only the first 15 collumns.	
CONT	Measurements are given with 50 Hz resolution, only column 1 to 15.

rxx.bin	
xx	Measurement run number
Post processed data file where the frames from all sub measurements are sorted in bins of the angle of attack to obtain the polar curves. The format of the data files is described in Table A-6.	
CONT	Measurements where the 50 Hz frames from all sub measurements are sorted in bins of α_c. The angle of attack range is divided into 30 bins.

rxx-loop.bin	
xx	Measurement run number
Post processed data file where the frames from all sub measurements are sorted in bins of the phase of the hysteresis loop. The format of the data files is described in Table A-7.	
PITCH	Measurements where the 100 Hz frams from all sub measurements are sorted in bins of the phase of the hysteresis loop. The phase range is divided into 30 bins.

cp-yyhz.nnn	
yy	Frame average frequency: 5 or 1
nnn	measurement sub number
Data file with each frame/average formatted in columns. The first column contains the x-coordinates of the pressure tabs. The subsequent columns contain the C_P distributions for the different frames. The angle of attack for the frames can be found in the corresponding, rxx-yyhz.nnn file.	
STEP	Measurements are given with 5 Hz frame resolution
CONT	Measurements are given with 1 Hz frame resolution
STAT	Measurements are given with 1 Hz frame resolution

cp.pol	
Data file with each average formatted in columns. The first column contains the x-coordinates of the pressure tabs. The subsequent columns contain the average C_P distributions for each sub measurement. The angle of attack for the frames can be found in the corresponding, rxx.pol file.	
STEP	Measurements are given as 20 s average values

v_w-yyhz.nnn	
yy	Frame average frequency: 5 or 1
nnn	measurement sub number
Data file with each frame/average formatted in columns. The first column contains the coordinates of the wake rake total pressure tabs. The subsequent columns contain the wake rake velocity for the different frames. The angle of attack for the frames can be found in the corresponding, rxx-yyhz.nnn file.	
STEP	Measurements are given with 5 Hz frame resolution
CONT	Measurements are given with 1 Hz frame resolution
STAT	Measurements are given with 1 Hz frame resolution

v_w.pol	
Data file with each average formatted in columns. The first column contains the coordinates of the wake rake total pressure tabs. The subsequent columns contain the average wake rake velocity distributions for each sub measurement. The angle of attack for the frames can be found in the corresponding, rxx.pol file.	
STEP	Measurements are given as 20 s average values

Table A-4 The content of the columns in the general data file.

Col.	Symbol	Sensor	Unit	Description
1	α_c	αc	°	Corrected angle of attack
2	C_L	cl	-	Lift coefficient (pressure)
3	C_{Dc}	cdc	-	Corrected drag coefficient (wake rake + pressure)
4	C_{Mc}	cmc	-	Corrected moment coefficient (pressure)
5	C_{Dpc}	cdpc	-	Corrected drag coefficient (pressure)
6[*]	C_{Dw}	cdw		Drag coefficient (wake rake)
7	α	α	°	Raw angle of attack
8	C_D	cd	-	Raw drag coefficient (wake rake + pressure)
9	C_{Dp}	cdp		Raw drag coefficient (pressure)
10	C_M	cm	-	Raw moment coefficient (pressure)
11	Re	re		Free stream Reynolds Number
12	q_∞	qref	Pa	Free stream dynamic pressure
13	p_∞	ps,ref	Pa	Free stream static pressure
14	T	t	°	Tunnel temperature
15	p_{atm}	patm	Mbar	Atmospheric pressure
16-71[**]	C_P	cp(x)		Pressure coefficients corresponding to the coordinates in top row
72-74	p_{1-3}	ps,Pitot()	Pa	Pitot tube static pressures
75-77	p_{o1-3}	pt,Pitot()	Pa	Pitot tube total pressures
78-82[*]	p_w	ps,wake	Pa	Wake rake static pressures corresponding to the coordinates in top row
83-136[*]	p_{ow}	pt,wake	Pa	Wake rake total pressures corresponding to the coordinates in top row

*) At the 'PITCH' type measurements, the wake rake was not used. C_{DW} was set to C_{DP} and p_w and p_{ow} were not written in the data files

**) In some measurements one or more of the airfoil pressure sensors were excluded because of unstable calibration or because the pressure hole was blocked by vortex generators or roughness elements. The corresponding column in the file was then removed and the number of subsequent sensors changed.

Table A-5 The content of the columns in the raw data files.

Col.	Symbol	Sensor	Unit	Description
1	t	t	s	Running time
2	α	α	°	Raw angle of attack
3	C_L	cl	-	Lift coefficient (pressure)
4	C_{Dc}	cdc	-	Corrected drag coefficient (wake rake + pressure)
54	C_{Mc}	cmc	-	Corrected moment coefficient (pressure)
6	C_{Dpc}	cdpc	-	Corrected drag coefficient (pressure)
7[*]	r	ramp	rad	Hysteresis loop phase angle

*) At the 'STAT' type measurements, the hysteresis loop phase angle was not used.

Table A-6 The content of the columns in the post processed data files sorted in bins of the angle of attack.

Col.	Symbol	Sensor	Unit	Description
1	α_c	αc	°	Corrected angle of attack
2	C_L	cl	-	Lift coefficient (pressure)
3	C_{Dc}	cdc	-	Corrected drag coefficient (wake rake + pressure)
4	C_{Mc}	cmc	-	Corrected moment coefficient (pressure)
5	C_{Dpc}	cdpc	-	Corrected drag coefficient (pressure)

Table A-7 The content of the columns in the post processed data files sorted in bins of the phase angle of the hysteresis loop.

Col.	Symbol	Sensor	Unit	Description
1	α_c	αc	°	Corrected angle of attack
2	C_L	cl	-	Lift coefficient (pressure)
3	C_{Dpc}	cdpc	-	Corrected drag coefficient (pressure)
4	C_{Mc}	cmc	-	Corrected moment coefficient (pressure)

A.5 Performed measurements

Table A-8 to Table A-10 contain a list of the performed measurements for the different airfoil sections.

Table A-8 Performed measurements for Risø-A1-18

Run	Type	Surface conditions	Remarks
013	CONT	VGs at 0.20	
014	CONT	VGs at 0.20	
015	CONT	VGs at 0.20 LER	
016	CONT	LER	
017	CONT	Smooth flow	
018	STEP	Smooth flow	
019	STAT	Smooth flow	
020	CONT	VGs at 0.25	
021	CONT	VGs at 0.25 LER	
022	PITCH	Smooth flow	$k = 0.092, 1.4° < A < 2.0°$

Table A-9 Performed measurements for Risø-A1-21

Run	Type	Surface conditions	Remarks
001	CONT	Smooth flow	
002	STEP	Smooth flow	
003	CONT	VGs at 0.20	
004	CONT	VGs at 0.20 LER	
005	CONT	LER	
023	CONT	VGs at 0.25 LER	
024	CONT	VGs at 0.25	
025	CONT	Smooth flow	
026	PITCH	Smooth flow	$k = 0.092, 1.4° < A < 2.0°$

Table A-10 Performed measurements for Risø-A1-24

Run	Type	Surface conditions	Remarks
027	CONT	VGs at 0.20	
028	CONT	VGs at 0.20 LER	
029	CONT	LER	
030	CONT	VGs at 0.25 LER	
031	CONT	VGs at 0.25	
032	CONT	Smooth flow	
033	STEP	Smooth flow	
034	CONT	VGs at 0.15	
035	CONT	VGs at 0.15 LER	
036	CONT	VGs at 0.15 GF of 1% LER	
037	CONT	GF of 1% LER	
038	CONT	GF of 2% LER	
039	CONT	GF of 2%	
040	CONT	GF of 1%	
041	PITCH	GF of 1%	$k = 0.092,\ 1.4° < A < 2.0°$
042	CONT	Smooth flow	
043	PITCH	Smooth flow	$k = 0.092,\ 1.4° < A < 2.0°$
064	CONT	VGs at 0.10	
065	CONT	VGs at 0.10 LER	
066	CONT	VGs at 0.10 double spacing LER	
067	CONT	VGs at 0.10 double spacing	
081	CONT	VGs at 0.30	

Abstract (max. 2000 characters)

This report contains 2D measurements of the Risø-A1-18, Risø-A1-21 and Risø-A1-24 airfoils. The aerodynamic properties were derived from pressure measurements on the airfoil surface and in the wake. The VELUX open jet wind tunnel was used having a background turbulence intensity of 1%, a flow velocity of 42 m/s and a Reynolds number of 1.6×10^6. The airfoil sections had a chord of 0.60 m and a span of 1.9 m and end plates were used to minimise 3D flow effects. The measurements comprised both static and dynamic inflow where dynamic inflow was obtained by pitching the airfoil in a harmonic motion. We tested the influence of leading edge roughness, vortex generators and Gurney flaps both individually and in combination.

For smooth surface conditions, all three airfoils had the desirable properties of constant lift curve slope and low drag coefficient until the maximum lift of about 1.4 was reached. The Risø-A1-18 airfoil had a smooth post stall whereas the Risø-A1-21 and Risø-A1-24 airfoils had a significant drop in the lift coefficient after stall. Test on all airfoil sections mounted with zigzag tape showed that the airfoils were insensitive to leading edge roughness. However with a drop in the maximum lift coefficient to about 1.2. Mounting of delta wing shaped vortex generators and Gurney flaps showed that there was room for a significant increase in the maximum lift coefficient, which was increased to 1.90 for Risø-A1-24 with vortex generators located at 15% chord. The combination of vortex generators and Gurney flaps increased the maximum lift coefficient to about 2.0.